



HAL
open science

In-situ X-ray nano-tomography analysis of ceramic powder sintering

Aatreya Manjulagiri Venkatesh

► **To cite this version:**

Aatreya Manjulagiri Venkatesh. In-situ X-ray nano-tomography analysis of ceramic powder sintering. Chemical engineering. Université Grenoble Alpes [2020-..], 2023. English. NNT : 2023GRALI055 . tel-04234988

HAL Id: tel-04234988

<https://theses.hal.science/tel-04234988v1>

Submitted on 10 Oct 2023

HAL is a multi-disciplinary open access archive for the deposit and dissemination of scientific research documents, whether they are published or not. The documents may come from teaching and research institutions in France or abroad, or from public or private research centers.

L'archive ouverte pluridisciplinaire **HAL**, est destinée au dépôt et à la diffusion de documents scientifiques de niveau recherche, publiés ou non, émanant des établissements d'enseignement et de recherche français ou étrangers, des laboratoires publics ou privés.

THÈSE

Pour obtenir le grade de

DOCTEUR DE L'UNIVERSITÉ GRENOBLE ALPES

École doctorale : I-MEP2 - Ingénierie - Matériaux, Mécanique, Environnement, Energétique, Procédés, Production

Spécialité : 2MGE : Matériaux, Mécanique, Génie civil, Electrochimie

Unité de recherche : Science et Ingénierie des Matériaux et Procédés

Analyse du frittage de poudres céramiques par nano-tomographie aux rayons X in-situ

In-situ X-ray nano-tomography analysis of ceramic powder sintering

Présentée par :

Aatreya Manjulagiri VENKATESH

Direction de thèse :

Didier BOUVARD

PROFESSEUR EMERITE, Grenoble INP

Pierre LHUISSIER

CHARGE DE RECHERCHE, CNRS

Julie VILLANOVA

BEAMLINER RESPONSIBLE, ESRF

Directeur de thèse

Co-encadrant de thèse

Co-encadrante de thèse

Rapporteurs :

François Valdivieso

PROFESSEUR DES UNIVERSITES, Ecole des Mines de Saint-Etienne

Dominique Bernard

DIRECTEUR DE RECHERCHE EMERITE, CNRS

Thèse soutenue publiquement le 7 juillet 2023, devant le jury composé de :

Didier BOUVARD

PROFESSEUR EMERITE, Grenoble INP

Elisabeth Djurado

PROFESSEUR DES UNIVERSITES, Grenoble INP

Sabine Rolland du Roscaot

PROFESSEUR DES UNIVERSITES, Université Grenoble Alpes

Fumihiko Wakai

PROFESSEUR EMERITE, Tokyo Institute of Technology

François Valdivieso

PROFESSEUR DES UNIVERSITES, Ecole des Mines de Saint-Etienne

Dominique Bernard

DIRECTEUR DE RECHERCHE EMERITE, CNRS

Directeur de thèse

Présidente

Examinatrice

Examineur

Rapporteur

Rapporteur

Invités :

Pierre Lhuissier

CHARGE DE RECHERCHE, CNRS

Julie Villanova

BEAMLINER RESPONSIBLE, ESRF



ABSTRACT

Ultra-high-resolution capabilities flaunted by the nano-imaging beamlines of the synchrotron facilities have now made *investigation of ceramic powders at the individual particle length-scale* feasible. These features were taken advantage of to investigate and enhance the understanding of sintering in two ceramic powder systems. Several 3D images with *a voxel size as low as 25nm* were obtained at different times of the thermal cycles for each powder system.

The first material under consideration comprised two *micron-sized alumina powders*. The resolution attained allowed the depiction of particles and pores with enough details for subsequent quantitative analyses.

Post-mortem analyses were initially carried out on these alumina powders, sintered at 1500°C for various time periods. *The phase-contrast X-ray nano-holotomography* technique employed at the *ID16B nano-analysis beamline of the European Synchrotron Radiation Facility (ESRF)* allowed us to include large volumes of interest and examine various stages of sintering. Data resulting from quantitative image analyses were used to explore both densification and grain growth phenomena throughout the sintering cycle.

In a further breakthrough, to monitor the evolution of sintering in real-time, X-ray nanotomography experiments were accomplished *in-situ, directly inside the synchrotron hutch*. A *compact high-temperature furnace* was designed and developed for the same, providing us with images in the course of sintering at the nano-scale for the first time. Several phenomena contributing to the collective behavior of the particles were accurately observed at the local scale. Among these analyses are the variations in grain size and shape, pore size, particle coordination number, inter-particle neck size and notably, pore curvature analysis for tracking the stages of sintering.

The experimental results were also confronted with a *discrete element simulation* to further compare and validate key sintering parameters.

The second investigated material is a *sub-micronic zinc oxide powder mixed with 20 vol.% of larger alumina inclusions*. In this case of *constrained sintering*, the 3D images allowed following up of the evolution of imperfections induced by zinc oxide aggregates, the effect of

the added constraints, the consequent crack generation and their implication on the final densification of the material.

RESUMÉ

Les caractéristiques d'ultra-haute résolution offertes par les lignes de faisceaux de nano-imagerie des installations synchrotron permettent désormais d'étudier les poudres céramiques à l'échelle de la particule individuelle. Ces caractéristiques ont été mises à profit pour étudier et améliorer la compréhension du frittage dans deux systèmes de poudres céramiques. Plusieurs images 3D avec une taille de voxel de 25 nm ont été obtenues à différents instants des cycles thermiques pour chaque système de poudre.

Le premier système examiné comprenait deux poudres d'alumine de la taille d'un micron. La résolution atteinte a permis de représenter les particules et les pores avec suffisamment de détails pour des analyses quantitatives ultérieures.

Des analyses post-mortem ont d'abord été effectuées sur ces poudres d'alumine, frittées à 1500°C pendant différentes périodes. La technique de nano-holotomographie par rayons X à contraste de phase utilisée sur la ligne de faisceau de nano-analyse ID16B de l'Installation européenne de rayonnement synchrotron (ESRF) nous a permis d'analyser de grands volumes et d'examiner différents stades de frittage. Les données résultant des analyses quantitatives d'images ont été utilisées pour explorer les phénomènes de densification et de croissance des grains tout au long du cycle de frittage.

Pour suivre l'évolution du frittage en temps réel, des expériences de nanotomographie par rayons X ont été réalisées in situ, directement dans l'enceinte expérimentale de la ligne de lumière utilisée. Un four compact à haute température a été conçu et développé à cet effet, ce qui nous a permis d'obtenir pour la première fois des images de l'évolution du frittage à l'échelle nanométrique. Plusieurs phénomènes contribuant au comportement collectif des particules ont été observés avec précision à l'échelle locale. Parmi ces analyses, figurent les variations de la taille et de la forme des grains, la taille des pores, le nombre de coordination des particules, la taille du cou interparticulaire, ainsi que l'analyse de la courbure des pores pour suivre les étapes du frittage.

Les résultats expérimentaux ont également été confrontés à une simulation par éléments discrets afin de comparer et de valider les principaux paramètres de frittage utilisés dans le modèle.

Le deuxième matériau étudié est une poudre d'oxyde de zinc submicronique mélangée à 20 % d'inclusions d'alumine de plus grande taille. Dans ce cas de frittage contraint, les images 3D ont permis de suivre l'évolution des imperfections induites par les agrégats d'oxyde de zinc, l'effet des contraintes ajoutées, la génération de fissures qui en découle et leur implication sur la densification finale du matériau.

ACKNOWLEDGEMENTS

अणोरणीयान् महतो महीयान्।

Growing up in India, imbibing the eternal ideologies of *Sanatana Dharma*, which asserts that - *there is smaller than the smallest and larger than the largest*, and that - *Infinity is reflected in the tiniest of finite things, while the finite-ness is also a part of infinity...*, it felt fascinating, to be of service, however minute, during these last 3 years, in trying to unlock the secrets of matter - deep down at the nano-meter scale!

Simply put, this thesis of mine, 'In-situ X-ray nano-tomography analysis of ceramic powder sintering', is a humble attempt, leveraging the outstanding features of the ESRF synchrotron, in Grenoble, to find out more about the powder processing technique called sintering. The plan was to bombard some powerful X-rays onto some of the chosen ceramic powders, and to get to know what really happens deep inside them during their sintering - at the nano-meter scale, while being in-situ as well, i.e. throughout the entire process, in real time!

In this regard, it is my bounden duty to, primarily, acknowledge my gratefulness to :-

The European Union - for bestowing me with their generous grant of the Marie-Curie research fellowship,

My MATHEGRAM training network - for the stimulation from my fellow ESRs and for the collaboration between their respective institutions across Europe, all sharing the same passion for scientific excellence,

My host institution CNRS-SIMaP at Grenoble - for welcoming me into their research fold and offering me access to their state-of-the-art facilities and resources, and

The Université Grenoble Alpes - for permitting me to enroll under its aegis and for having accepted this thesis, via the jury at the PhD defense, for the award of the *degree of doctor of philosophy*.

More specifically, I must place on record, my deep felt gratitude to my core PhD supervisory team. My main supervisor, Prof. Didier Bouvard, a renowned expert in the field of sintering, has been the coolest boss ever. He has always been encouraging, understanding and helpful in every aspect of my work. I am honored to have had the opportunity to work under his tutelage. My co-supervisors, Dr. Pierre Lhuissier of CNRS, who always has a plethora of ideas at his disposal, and Dr. Julie Villanova of the ESRF, who introduced me to and familiarized me with the intriguing world of synchrotron radiation, have both steered me, throughout the thesis, with constructive feedback and invaluable support.

Furthermore, I acknowledge the contributions of the technical faculty, both at SIMaP and at the ESRF, in particular, Mr. Cyril Rajon of SIMaP, who engineered critical practical aspects that were instrumental in the completion of this project.

Special thanks are, of course, due to Prof. Chuan-Yu (Charley) Wu of the University of Surrey, the man behind MATHEGRAM, for he has best led and coordinated the network's agenda, facilitating multiple trainings, symposiums and a seamless interaction between all the partner institutions.

In line with the network's objectives, I also got benefitted by the secondments I could carry out, as a visiting researcher, in France and abroad - at Saint Gobain Recherche in Paris, at the ESRF in Grenoble and at CIMNE in Barcelona. I am very grateful to the team of research experts that hosted me and guided me during my time there.

Although I had to face the brunt of some challenging times posed by the covid pandemic, I was fortunate enough, to attend, both online and in-person, and disseminate at conferences in the US, in the UK and in Europe, while cobbling up some time to explore those places.

Equally important has been the cooperation and the camaraderie of my fellow colleagues at SIMaP. The PhDs, the Post-docs and the interns, spread across the *green*, the *blue* and the *white* rooms of the *ECOMARCH* building at SIMaP, have all played a significant role in this journey; be it the ones who graduated during my thesis, the ones who shared similar timelines like me or the ones currently on their way. I would rather not name them - you know who you are - I will always cherish those great memories I spent with you and your families!

I hereby also acknowledge with thanks my indebtedness to all those scholars and publishers whose work I have freely made use of in this research. As I dedicate this thesis to *my family and my loved ones*, while offering them my salutations and my profuse appreciation - I wish my work here - this thesis and the publications contained in it - finds a comparable contribution to the scientific community as well.

ॐ असतो मा सद्गमय
तमसो मा ज्योतिर्गमय
मृत्योर् मा अमृतं गमय

वाराणसी लक्ष्मणजीवश्रीने चरणरत्नद्वारे
जुलै २०२३
इन्द्रावती, वाराणसी

CONTENTS

ABSTRACT	2
RESUMÉ	4
CONTENTS	9
GENERAL INTRODUCTION	13
INTRODUCTION GÉNÉRALE	18
CHAPTER-1	
STATE OF THE ART AND OBJECTIVES	24
1.1 Sintering of Ceramics	24
1.1.1 Ceramics - Our constant companions	24
1.1.2 Sintering - Current understanding	25
1.1.3 Macroscopic driving force - Constituents of sintering process	26
1.1.4 Local driving force - Solid state diffusion	30
1.1.5 Classical classification of the stages of sintering	31
1.1.6 Modeling of sintering - Classical 2 sphere models to contemporary DEM	32
1.2 Experimental Investigation - 3D Imaging	38
1.2.1 Advances in 3D imaging - Metallic powder sintering	39
1.2.2 3D imaging complexities - Ceramic powder sintering	41
1.3 Premise and Objectives	43
CHAPTER-2	
EXPERIMENTAL METHODOLOGY	48
2.1 Process Outline	48
2.1.1 Powder system under consideration	48
2.1.2 From powders to green compacts	50
2.1.3 Thermo-mechanical analyses - From green compacts to sintered ones	52
2.1.4 Post-mortem experiment scheme	54
2.1.5 In-situ experiment scheme	55
2.2 Science of Synchrotrons	56
2.2.1 ESRF's nano-analysis beamline - ID16B	57
2.2.2 Imaging concepts - Tomography	58

2.2.3 Phase-contrast X-ray nano-holotomography	59
2.2.4 Design and development of the furnace	65
2.3 Image Processing and Segmentation	69
2.4 Quantitative Analyses and Derived Outcomes	72
CHAPTER-3	
POST-MORTEM NANO-TOMOGRAPHY INVESTIGATION	75
3.1 Introduction	76
3.2 Materials and Methods	78
3.2.1 Powder and sample preparation	78
3.2.2 Phase-contrast X-ray nano-holotomography	79
3.2.3 Image treatment and analyses	80
3.3 Results	82
3.3.1 Global assessment	82
3.3.2 Quantitative insights	83
3.3.3 Density – Grain volume fraction correlation	83
3.3.4 Grain size progression	84
3.3.5 Pore size measurements	86
3.3.6 Pore connectivity and closure	88
3.3.7 Pore throat characterization	89
3.3.8 Curvature maps	90
3.4 Conclusion	93
CHAPTER-4	
IN-SITU NANO-TOMOGRAPHY INVESTIGATION	96
4.1 Introduction	97
4.2 Materials and Methods	100
4.2.1 Sample preparation	100
4.2.2 Furnace - design and development	101
4.2.3 Synchrotron nano-tomography experiment	102
4.2.4 Image processing and segmentation	103
4.3 Results and discussion	106
4.4 Conclusion	123
CHAPTER-5	
TOWARDS A MORE COMPLEX CERAMIC POWDER SYSTEM	127

5.1 Introduction	128
5.2 Materials and Methods	130
5.3 Results	133
5.3.1 Post-mortem investigation	133
5.3.2 In-situ investigation	134
5.4 Conclusion	142
CHAPTER-6	
COMPARISON WITH DISCRETE ELEMENT SIMULATION	145
6.1 Introduction	145
6.2 Model description	147
6.3 Results	148
6.3.1 Consolidation - Alumina 1.3 μm	148
6.3.2 Grain growth - Alumina 0.7 μm	152
6.4 Conclusion	154
CHAPTER-7	
CONCLUSION AND PERSPECTIVES	156
REFERENCES	161

GENERAL INTRODUCTION

This PhD project by Aatreya Manjulagiri VENKATESH has been carried out in the framework of MATHEGRAM – a Marie Skłodowska-Curie actions Innovative Training Network, funded by the European Union. MATHEGRAM is a multi-disciplinary and inter-sectoral consortium composed of 10 prominent academic and non-academic beneficiaries across Europe, in addition to 5 partner organizations. It strives to address the key challenges related to the thermo-mechanical behavior of granular materials, across different scales and applications. In this context, a cohort of 15 early stage researchers (ESRs) have been dealing with 15 individual projects. The present work, 'In-situ X-ray nano-tomography analysis of ceramic powder sintering' is by ESR14 and has been carried out at the SIMaP laboratory of Université Grenoble Alpes and CNRS. This project is associated with the PhD thesis of ESR15 (Brayan Marcelo PAREDES GOYES), dealing with the discrete element method (DEM) simulation of ceramic powder systems, at SIMaP, as well.

X-ray tomography is a technique that can reveal the internal details of objects in three-dimensions (3D) non-destructively - the penetrating power of X-rays is exploited to obtain a series of two-dimension (2D) radiographs of the object viewed from many different directions, and then a 3D image is computationally reconstructed from these projections. This technique can provide unrivalled information about the structure, morphology, defects, damage and dynamic evolution of objects across various length-scales and under different loading conditions. It has its own set of advantages over conventional characterization methods that are either invasive and/or are generally restricted to 2D information.

X-ray tomography has been widely used in various fields of science and engineering, such as medicine, geology, paleontology, metrology, manufacturing etc. Here, emphasizing its role in *materials science* - it can help understand and optimize the properties and performance of materials for various applications. To this end, X-ray micro-tomography (micro-CT or μ CT), introduced in the 1980s, capable of working at the level of microns, has been a standard tool in materials science research.

One of the fields that can benefit from this technique is *powder sintering*, i.e., the consolidation and transformation of powder particles into a dense solid with tailored microstructure and properties, by thermal energy. It is a key powder processing route for metallic and ceramic

materials. The ISO definition of the term reads: 'The thermal treatment of a powder or compact at a temperature below the melting point of the main constituent, for the purpose of increasing its strength by bonding together of the particles'.

However, μ CT has only been able to provide limited insights into the *sintering of ceramics* so far. μ CT cannot detect the individual ceramic particles, which are often less than 1 μm in size and are, not to mention, relatively complex and irregular in shape as well. The collective phenomena occurring during sintering further complicate the observation process. Sintering of ceramics has therefore not been fully mastered nor modelled, especially for powder systems with multiple phases and compositions.

Some of the open questions on ceramic sintering that need to be addressed or investigated further are: What are the factors that influence the rate and shape of inter-particle neck formation? How can densification be enhanced without compromising the grain size and porosity of sintered ceramics? What are the roles of driving forces, diffusion mechanisms, and external fields in densification? How is grain growth coupled with densification? How can grain growth be controlled to achieve optimal grain size distribution and orientation? What are the effects of sintering additives, impurities, and defects on the sintering behavior and performance of ceramics? How can they be used to tailor the sintering process and the final properties of ceramics?

Over the years, several researchers have demonstrated the success of μ CT with regard to sintering of materials like metal powders, and have foreseen the potential applications of X-ray tomography for sintering research in ceramics. The need for more advancement, such as improvement in the resolution capabilities to obtain comprehensive data on the microstructural evolution during sintering, is stressed by many, as well. A few chosen review works are mentioned below for reference:

- *Current understanding and future research directions at the onset of the next century of sintering science and technology* by Bordia *et al.* [1] - provides a comprehensive overview of the present status and future prospects of sintering science and technology. The authors also point out the importance of 3D imaging by tomography as a means to gain fundamental insights into the complex phenomena involved in sintering.

- *Quantitative analysis of microstructure and modeling of sintering* by Jean-Marc Chaix [2] - presents a comprehensive approach to characterize and simulate the microstructural evolution during sintering using X-ray tomography techniques. It shows that the 3D images can provide

accurate measurements of particle size, shape and coordination number, as well as local densification and shrinkage rates.

- *Multi-Scale Study of Sintering: A Review* by Olevsky *et al.* [3] - reviews the multi-scale aspects of sintering, from atomic to macroscopic levels, and discusses how X-ray tomography can help bridge the gap between different scales and provide experimental validation for theoretical models.

- *Constrained sintering: A delicate balance of scales* by Green *et al.* [4] - examines the role of external or internal constraints on sintering behavior and highlights the importance of in-situ X-ray tomography to reveal the complex interactions in the microstructure during *constrained sintering*.

Fortunately, we have seen steady progress in the field of X-ray tomography in the last decade. Some major developments over the past few years in imaging in general that can be applied to sintering are:

- The use of synchrotron radiation sources that offer high flux, coherence and spatial resolution, enabling high-quality tomographic acquisition;

- The development of versatile mechanical testing devices that permit continuous and controlled loading during tomography scanning, enabling the study of damage and fracture in sintered materials;

- The exploitation of different contrast modes that can differentiate between phases, grains, pores and cracks in the microstructure based on their absorption, refraction or scattering properties;

- The application of advanced image processing and analysis methods that can segment, visualize and quantify the 3D microstructural features and their evolution during sintering.

Taking into account all these challenges, developments, and prospects, at this critical juncture, this project was made possible by a combination of factors:

- the recent upgrade of the European Synchrotron Radiation Facility (*ESRF*), which enabled *fast in-situ X-ray nano-tomography* at one of their nano-probes ID16B (Villanova *et al.* [5]);
- the acceptance of our scientific proposals and the provision of the *ESRF* facilities for our experiments;

- the coming across of a simplistic ceramic powder produced by an advanced hydrolysis technique;
- the development of a custom-made compact high-temperature furnace; and
- the timely funding grants from MATHEGRAM.

The above factors were successfully applied to perform high-resolution visualizations and real-time assessments of ceramic powders at their particle length-scale; the process and the quantitative results of which constitute this PhD dissertation. It is written as an *integration of journal articles* (with principal authorship) that have been published in or are submitted to reputed peer-reviewed journals. The articles are connected by suitable transitions that ensure a consistent and coherent reading experience.

Chapter 1 provides an overview of the sintering process and its applications in ceramics, as well as a critical review of the existing literature on the topic. It also introduces the main research questions, setting up the premise and objectives of this thesis.

Chapter 2 describes the experimental methods employed in this work, including the selection of suitable powders, the design and development of the furnace for in-situ experiments, and the X-ray nano-tomographic set-up to obtain high-resolution 3D images of the sintering samples.

Chapter 3 reports the results of the first article produced from this project, which investigates the sintering behavior of a model micron-sized alumina powder using *post-mortem synchrotron experiments*. It reveals for the first time the 3D microstructure of ceramic samples at the particle length-scale with a resolution of 25 nm.

Chapter 4 presents the results of the second article produced from this project, involving a *novel in-situ experiment* at the synchrotron to capture real-time transient and local phenomena during sintering of the same alumina powder at the particle length-scale.

Chapter 5 discusses the results of a collaborative work with ESR15, which compares the obtained tomography data with a *discrete element model* (DEM) developed for sintering simulations. The results are promising enough to be published as an article in the near future.

Chapter 6 outlines the results of the third article to-be-published from this project, which extends the tomography analyses to a more *complex industrial ceramic powder* composed of zinc oxide nanoparticles, mixed with alumina inclusions. It explores the effects of constrained sintering on the microstructure evolution and reveals the formation and propagation of anomalies.

Chapter 7 summarizes the main findings and contributions of this thesis and suggests some directions for future research in the ceramic sintering domain.

INTRODUCTION GÉNÉRALE

Cette thèse de doctorat d'Aatreya Manjulagiri VENKATESH a été réalisée dans le cadre de MATHEGRAM – un réseau de formation innovante (ITN), financé par l'Union européenne dans le cadre des actions Marie Skłodowska Curie. MATHEGRAM est un réseau multidisciplinaire et intersectoriel composé de 10 organismes académiques et non académiques à travers l'Europe, ainsi que de 5 organisations partenaires. Il s'efforce de relever les principaux défis liés au comportement thermomécanique des matériaux granulaires, à différentes échelles et pour différentes applications. Dans ce contexte, un groupe de 15 chercheurs en début de carrière (ESR) ont été chargés de 15 projets individuels. Le présent travail, intitulé "In-situ X-ray nano-tomography analysis of ceramic powder sintering", est réalisé par l'ESR14 au laboratoire SIMaP de l'Université Grenoble Alpes et du CNRS. Ce projet est associé à la thèse de doctorat de l'ESR15 (Brayan Marcelo PAREDES GOYES), portant sur la simulation par la méthode des éléments discrets (DEM) de systèmes de poudres céramiques, au SIMaP également.

La tomographie par rayons X est une technique qui permet de révéler les détails internes des objets en trois dimensions (3D) de manière non-destructive. Le pouvoir de pénétration des rayons X est exploité pour obtenir une série de radiographies en deux dimensions (2D) de l'objet vu dans de nombreuses directions différentes, puis une image 3D est reconstruite par calcul à partir de ces projections. Cette technique peut fournir des informations inégalées sur la structure, la morphologie, les défauts, les dommages et l'évolution dynamique des objets sur différentes échelles de longueur et dans différentes conditions de chargement. Elle présente ses propres avantages par rapport aux méthodes de caractérisation conventionnelles qui sont soit invasives, soit limitées à des informations en 2D.

La tomographie par rayons X a été largement utilisée dans divers domaines de la science et de l'ingénierie, tels que la médecine, la géologie, la paléontologie, la métrologie, la fabrication, etc. En mettant l'accent sur son rôle dans la science des matériaux, elle peut aider à comprendre et à optimiser les propriétés et les performances des matériaux pour diverses applications. À cette fin, la micro-tomographie à rayons X (micro-CT ou μ CT), introduite dans les années 1980, capable de travailler à l'échelle du micron, est devenu un outil standard dans la recherche en science des matériaux.

L'un des domaines pouvant bénéficier de cette technique est *le frittage des poudres*, c'est-à-dire la consolidation et la transformation des particules de poudre en un solide dense à la microstructure et aux propriétés adaptées grâce à l'énergie thermique. Il s'agit d'une méthode essentielle de traitement des poudres pour les métaux et céramiques. La définition ISO du terme Frittage est la suivante: 'le traitement thermique d'une poudre ou d'un compact à une température inférieure au point de fusion du principal constituant, dans le but d'augmenter sa résistance en liant les particules entre elles'.

Cependant, jusqu'à présent, la μ CT n'a pu fournir que des informations limitées sur *le frittage des céramiques*. La μ CT ne peut pas détecter les particules de céramique individuelles, dont la taille est souvent inférieure à 1 μ m et dont la forme est, en outre, relativement complexe et irrégulière. Les phénomènes collectifs qui se produisent pendant le frittage compliquent encore le processus d'observation. Le frittage des céramiques n'a donc pas été entièrement maîtrisé ni modélisé, en particulier pour les systèmes de poudres à phases et compositions multiples.

Certaines des questions ouvertes sur le frittage des céramiques qui doivent être abordées ou étudiées de manière plus approfondie sont les suivantes: Quels sont les facteurs qui influencent la vitesse de formation des cols interparticulaires? Comment la densification peut-elle être améliorée sans compromettre la taille des grains et la porosité des céramiques frittées? Quels sont les rôles des forces motrices, des mécanismes de diffusion et des champs externes dans la densification? Comment la croissance des grains est-elle couplée à la densification? Comment la croissance des grains peut-elle être contrôlée pour obtenir une distribution et une orientation optimales de la taille des grains? Quels sont les effets des additifs de frittage, des impuretés et des défauts sur le comportement de frittage et les performances des céramiques? Comment peuvent-ils être utilisés pour adapter le processus de frittage et les propriétés finales des céramiques?

Au fil des années, plusieurs chercheurs ont démontré le succès de la μ CT en ce qui concerne le frittage des poudres métalliques et ont prévu les applications potentielles de la tomographie par rayons X pour la recherche sur le frittage des céramiques. Nombreux sont ceux qui soulignent la nécessité d'aller plus loin, notamment en améliorant les capacités de résolution afin d'obtenir des données complètes sur l'évolution de la microstructure au cours du frittage. Quelques documents de synthèse sont mentionnés ci-dessous à titre de référence:

- *Current understanding and future research directions at the onset of the next century of sintering science and technology* par Bordia *et al.* [1] - donne un aperçu complet de l'état actuel

et des perspectives d'avenir de la science et de la technologie du frittage. Les auteurs soulignent également l'importance de l'imagerie 3D par tomographie comme moyen d'obtenir des informations fondamentales sur les phénomènes complexes impliqués dans le frittage.

- *Quantitative analysis of microstructure and modeling of sintering* par Jean-Marc Chaix [2] - présente une approche complète pour caractériser et simuler l'évolution de la microstructure pendant le frittage à l'aide de techniques de tomographie à rayons X. Il montre que les images 3D peuvent fournir des mesures précises de la taille, de la forme et du nombre de coordination des particules, ainsi que des taux de densification et de retrait locaux.

- *Multi-Scale Study of Sintering: A Review* par Olevsky *et al.* [3] - examine les aspects multi-échelles du frittage, du niveau atomique au niveau macroscopique, et explique comment la tomographie par rayons X peut aider à combler le fossé entre les différentes échelles et fournir une validation expérimentale des modèles théoriques.

- *Constrained sintering: A delicate balance of scales* par Green *et al.* [4] - examine le rôle des contraintes externes ou internes sur le comportement de frittage et souligne l'importance de la tomographie par rayons X *in situ* pour révéler les interactions complexes dans la microstructure pendant le frittage.

Heureusement, des progrès constants ont été réalisés dans le domaine de la tomographie par rayons X au cours de la dernière décennie. Quelques développements majeurs de ces dernières années dans le domaine de l'imagerie en général qui peuvent être appliqués au frittage sont les suivants:

- L'utilisation de sources de rayonnement synchrotron qui offrent un flux, une cohérence et une résolution spatiale élevés, permettant l'acquisition d'images de haute qualité, y compris à des températures et des pressions élevées pendant des expériences *in situ*;

- Le développement de dispositifs d'essais mécaniques polyvalents qui permettent un chargement continu et contrôlé pendant l'acquisition tomographique, ce qui permet d'étudier les dommages et les fractures dans les matériaux frittés;

- L'exploitation de différents modes de contraste permettant de différencier les phases, les grains, les pores et les fissures dans la microstructure sur la base de leurs propriétés d'absorption, de réfraction ou de diffusion;

- L'application de méthodes avancées de traitement et d'analyse d'images qui peuvent visualiser et quantifier les caractéristiques de la microstructure en 3D et leur évolution au cours du frittage.

Compte tenu de tous ces défis, développements et perspectives, à ce moment critique, ce projet a été rendu possible par une combinaison de facteurs:

- la récente mise à niveau de l'installation européenne de rayonnement synchrotron (ESRF), qui a permis le développement de *la nano-tomographie par rayons X rapide et in situ* à l'une de ses lignes de lumière possédant un nano-faisceau ID16B (Villanova *et al.* [5]);
- l'acceptation de nos propositions scientifiques et la mise à disposition des installations de l'ESRF pour nos expériences;
- la découverte d'une poudre céramique simple produite par une technique d'hydrolyse avancée;
- le développement d'un four compact à haute température sur mesure; et
- le financement opportun de MATHEGRAM.

Les facteurs ci-dessus ont été mis à profit avec succès pour effectuer des visualisations à haute résolution et en temps réel de poudres céramiques à l'échelle des particules ; le processus et les résultats obtenus constituent cette thèse de doctorat. Cette thèse est rédigée sous *la forme d'articles* (avec le doctorant comme auteur principal) publié dans une revue à comité de lecture ou soumis à de telles revues. Les articles sont reliés entre eux par des transitions appropriées qui assurent une lecture cohérente et homogène.

Le chapitre 1 présente une vue d'ensemble du processus de frittage et de ses applications dans le domaine des céramiques, ainsi qu'un examen critique de la littérature existante sur le sujet. Il présente également les principales questions de recherche, en établissant les prémisses et les objectifs de cette thèse.

Le chapitre 2 décrit les méthodes expérimentales employées dans ce travail, y compris la sélection des poudres appropriées, la conception et le développement du four pour les expériences *in situ*, et la mise en place de l'équipement de nanotomographie par rayons X pour obtenir des images 3D haute résolution des échantillons de frittage.

Le chapitre 3 présente les résultats du premier article issu de ce projet, qui étudie le comportement de frittage d'une poudre d'alumine modèle de taille micrométrique à l'aide

d'expériences synchrotron post-mortem. Il révèle pour la première fois la microstructure 3D des échantillons céramiques à l'échelle des particules avec une taille de pixel de 25 nm.

Le chapitre 4 présente les résultats du deuxième article produit dans le cadre de ce projet, qui implique *une nouvelle expérience in-situ* au synchrotron pour capturer en temps réel les phénomènes transitoires et locaux pendant le frittage de la même poudre d'alumine à l'échelle de la longueur des particules.

Le chapitre 5 présente les résultats d'un travail en collaboration avec l'ESR15, qui compare les données de tomographie obtenues avec les résultats d'un *modèle aux éléments discrets* (DEM) développé pour les simulations de frittage. Les résultats sont suffisamment prometteurs pour faire l'objet d'un article dans un avenir proche.

Le chapitre 6 présente les résultats du troisième article à paraître dans le cadre de ce projet, qui étend les analyses tomographiques à un matériau *plus complexe composé d'une poudre industrielle* composée de nanoparticules d'oxyde de zinc et mélangée à des inclusions d'alumine. Il explore les effets du frittage contraint sur l'évolution de la microstructure et révèle la formation et la propagation des défauts.

Le chapitre 7 résume les principaux résultats de cette thèse et suggère quelques orientations pour les recherches futures dans le domaine du frittage des céramiques.

CHAPTER-1

STATE OF THE ART AND OBJECTIVES

1.1 Sintering of Ceramics

1.1.1 Ceramics - Our constant companions

“Ceramics are amazing materials! Some are delicate and fragile; others are so strong and durable that they are used to reinforce metals and plastics. Some ceramics are transparent. Others are magnetic. Many ceramics withstand temperatures many times the temperature of your oven and are untouched by erosion and corrosion that destroy metals in days. Ceramics have so many different characteristics and make so many things possible in our modern society that they seem magical.” [6]

W. D Kingery, in his classic text ‘Introduction to Ceramics’, defines ceramics as “the art and science of making and using solid articles which have as their essential component, and are composed in large part of inorganic, non-metallic materials.” [7]

Going by this definition, simply put, most solid materials that are not metal, plastic, or derived from plants or animals are ceramics .

Ceramics, therefore, are truly everywhere - at our homes, at our workplaces, in the outdoors and elsewhere - ceramics have permeated every aspect of our lives and are an integral part of our existence.

The diverse set of properties of ceramics have made them gain a substantial application spectrum and form a basis for the successful operation of numerous other industries. In comparison to other engineering materials like metals, ceramic materials generally have a lower density, which makes them suitable for light-weight applications. In addition, they possess outstanding physical and mechanical properties, such as high strength and hardness, strong anti-corrosion and temperature resistance.

These properties were exploited to guide the evolution of traditional ceramics used for centuries for pottery and stoneware to the new-age advanced ceramics. In fact, in the 1800s, the advent of a technique to produce, at low cost, thousands of tons of pure alumina powders led to a

further explosion of new ceramics and ceramic uses. These techniques were emulated and utilized to engineer all of the subsequent ceramic compositions. Wide varieties of ceramics were invented, and are still in an active state of development: high-strength, high-temperature ceramics; magnetic ceramics; glass ceramics; piezoelectric ceramics; special optical ceramics; bio-ceramics etc. [8].

To transform the powders into a useful product, while the majority of the metals and their alloys can be melted or cast and, when required, forged or machined to attain the final shape, for ceramic materials, such fabrication techniques are unsuitable. Ceramic materials have a higher melting point, which makes it difficult to cast them or give them a desired shape by molding processes. At the same time, they are brittle in nature, which places processes like forging beyond consideration. Nevertheless, ceramic materials can also be melted and cast under certain special circumstances to develop certain properties, but they are obviously cost intensive and are normally avoided.

Fortunately, for the ceramic community, *sintering* provides an alternative route for the shaping and consolidation of the ceramic powders.

1.1.2 Sintering - Current understanding

For ceramic fabrication via the sintering route, the starting raw materials are in powdery form. It is relatively easy to obtain them - by grinding the naturally occurring lumpy minerals or by chemical synthesis in the case of advanced ceramics. Powdery raw materials, at the same time, provide a number of benefits. They exhibit free flowing characteristics and can be directly fed into a mold and pressed to a shape under high pressure.

Given an opportunity, meaning, if and when sufficient activation energy is made available, powders tend to lose the excess energy associated with their surfaces. This phenomenon is made use of in sintering, wherein a certain activation energy is provided to a powder system by heating it to higher temperatures. This results in the excess free energy being removed and a strong bond being formed between the particles [9].

In essence, in the sintering process, a powder or a powder compact, when subjected to just thermal energy below the melting point of its main constituent, is transformed into a bulk material of regulated density. As a result of this, a coherent and mechanically strong non-porous bulk body is produced from the loosely bonded initial powder or powder compact with a lower mechanical strength [10].

Sintering, therefore, is a unique phenomenon and one of the most important steps in the manufacturing of ceramic products.

1.1.3 Macroscopic driving force - Constituents of sintering process

The macroscopic driving force for sintering, as mentioned above, is the lowering of the excess free energy associated with the free surfaces of the initial powders. This decrease in free energy may occur in different ways, either by the reduction of total surface area through increase of the average size of the particles, or by replacement of high energy solid-vapor interface by low energy solid-solid interface. In the first case, some particles get coalesced with each other with not necessarily a strong bond getting developed. In the latter case, the solid particles come in contact with each other with a strong chemical bond, i.e., there is an inter-particulate transfer between the solid particles resulting in the formation of a grain boundary interface. Both of these cases may occur simultaneously or one may lead the other, depending on local situations.

(In this work, as in the case of the science of granular materials, the definitions of *particles* and *grains* are used interchangeably, although they are different from each other from a crystallographic point of view).

A pictorial representation of the driving force of sintering is depicted below, showing different constituents of the overall sintering process (**Figure 1**):

Particle coarsening - wherein some of the particles grow at the expense of others, the contact area between the particles do not change much and there is no formation of a bond taking place. The overall surface area (ΔA) reduces due to coarser particles, causing a reduction in surface energy while the mechanical strength of the material remains the same;

Densification - through which loosely bonded powder particles change their configurations, come in contact with each other (*consolidation*), forming strong bonds in terms of *grain boundaries* and becoming dense while clearing out inter-particulate pores. In this case, therefore, the quality of the surface changes, with a change in surface energy term ($\Delta\gamma$). Densification in turn results in overall contraction of the powder compact (*shrinkage*);

Grain Growth - in which both coarsening and densification occur simultaneously ($\Delta A + \Delta\gamma$): the final product is not only densified with the formation of surface contacts but is also accompanied by an increase in the size of the individual grains.

Under certain circumstances, another probability is for the material to undergo a step-by-step transformation by first going through densification ($\Delta\gamma$) without increase in average grain size,

then if provided with sufficient activation energy, the smaller particles would evolve into a bigger size (ΔA).

In principle, however, for optimal properties, the idea of sintering is to have a densified body with minimal pores and as less grain growth as possible [11].

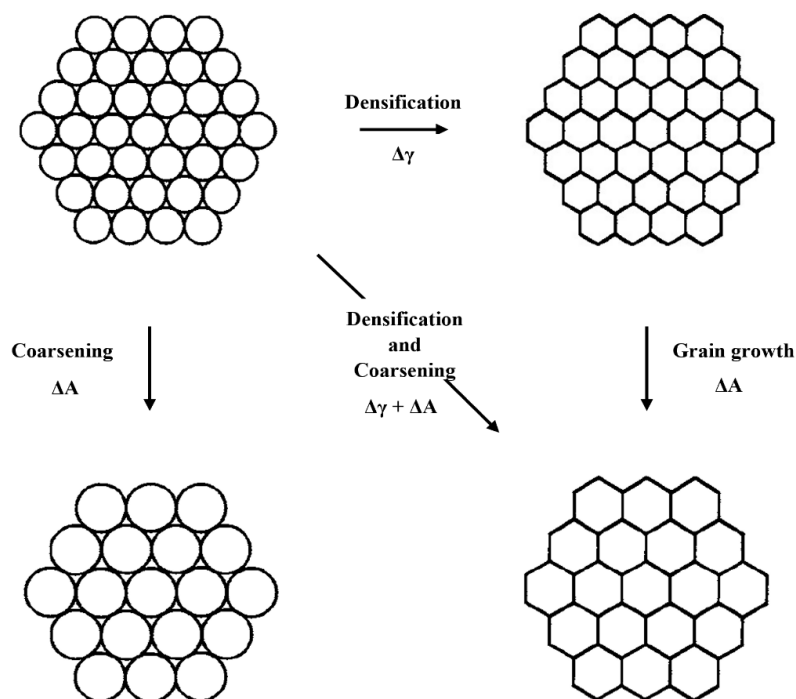


Figure 1. Schematic of the constituents of sintering: densification and grain growth [10].

In addition to this pressure-less solid-state sintering discussed above, there are many other variations to the process. For example, pressure sintering - wherein sintering is aided by a pressure; reactive sintering - which is a combination of sintering and associated chemical reactions between the constituents; microwave sintering - where the material is heated by coupling with microwaves; spark plasma sintering - a relatively newer technique, where a certain pressure as well as a very high DC voltage is applied to assist the sintering mechanisms.

On the whole, be it any of the variations mentioned above, the sintering process mainly leads to a significant enhancement of mechanical strength of the material. This is led by the inter-particle contact growth and densification of the particle assembly and the associated global volumetric shrinkage of the powder compact. In addition, consequently, there is reduction in overall pore size and volume. Moreover, if not controlled, intense grain growth could take place at higher temperatures, which in most cases acts as a hindrance to the mechanical properties desired.

Generally, the typical shrinkage behavior of a ceramic material would proceed with time and temperature as shown in **Figure 2**. The shrinkage here is represented in terms of the axial shrinkage $\Delta L/L$, and the volumetric shrinkage is then usually computed from the axial shrinkage data. As in the case of a thermally activated phenomenon, initially at temperature T_1 , shrinkage increases for a certain period, but then tapers off with increasing time and becomes almost constant. At a higher temperature T_2 , initial shrinkage rate is faster than the previous case. It then stabilizes and turns constant after a certain time, however much faster than at T_1 .

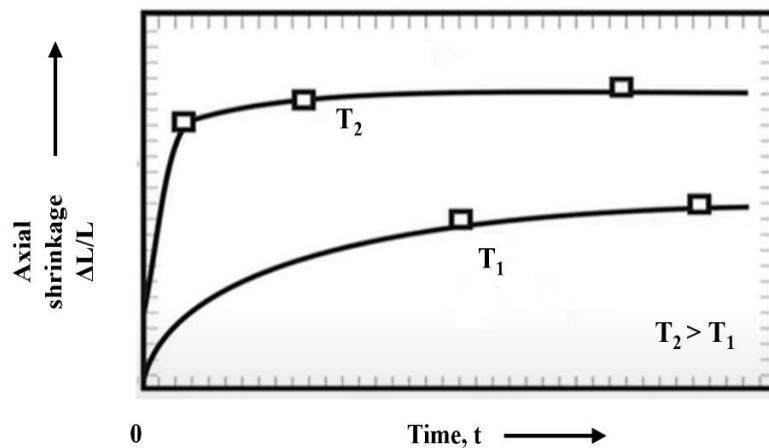


Figure 2. Typical axial shrinkage behavior as a function of time and temperature [9].

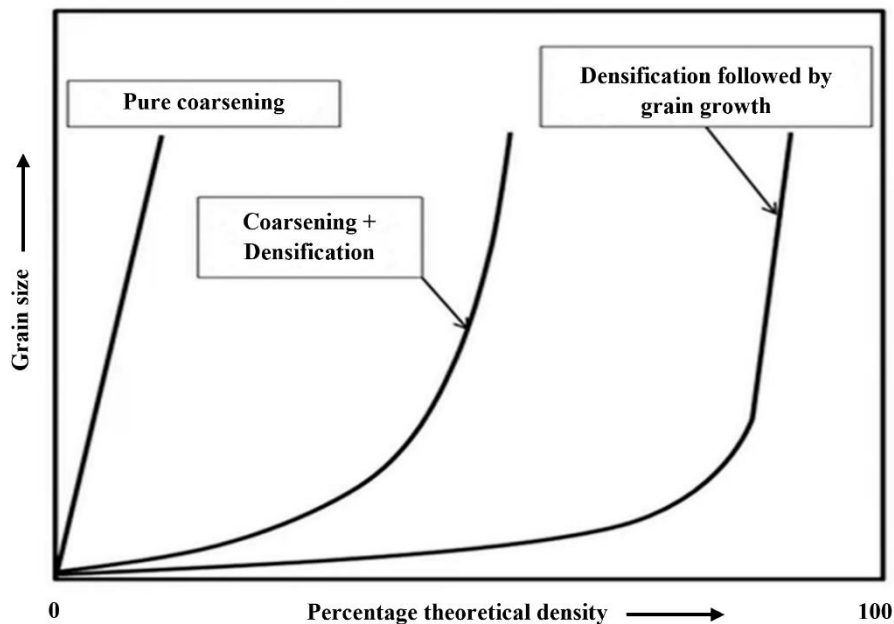


Figure 3. Variation of grain size with density at different conditions [9].

With respect to the variation in the size of the grains as a function of percentage shrinkage, typically there could be three different likely scenarios (**Figure 3**), as described pictorially in **Figure 1**. As the percentage theoretical density increases, powders could either coarsen without sintering, which is not an ideal situation, as it leads to poor mechanical strength; or the powders could sinter forming grain boundaries and later exhibit grain growth. This scenario is not preferred as well as higher grain growth could result in brittleness, sub-par mechanical behavior etc. The intermediate scenario, wherein densification and grain growth proceed gradually and simultaneously is a favored situation out of the three, as both the mechanisms are controlled.

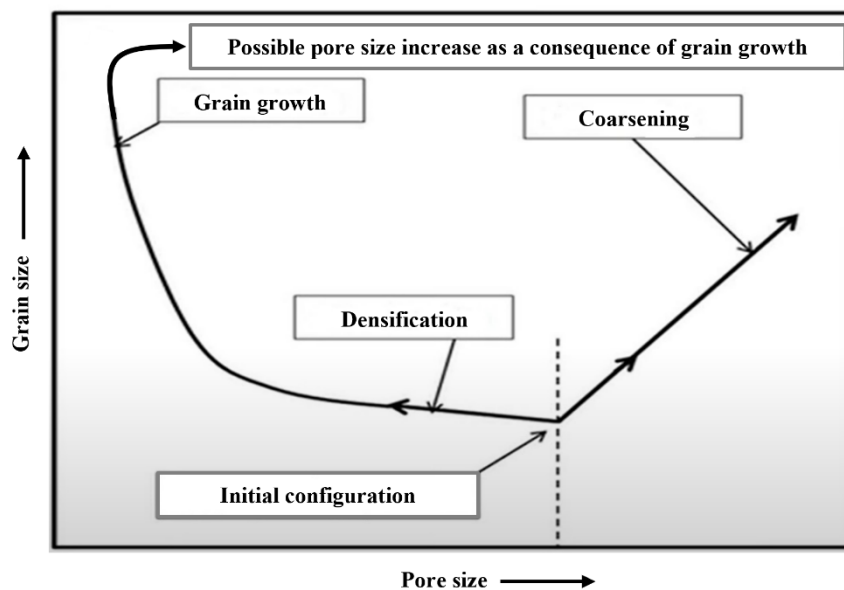


Figure 4. Variation of grain size with pore size at different conditions [9].

Plotting the above representation in **Figure 3** in a slightly different manner in terms of a correlation between grain size and pore size as in **Figure 4**, the scenario of pure coarsening leads to an increase in both grain and pore size more or less in a linear fashion. Whereas, during densification, pore size gradually reduces, and further decreases significantly towards the end when grain growth comes into the picture. This being the desired situation, the objective therefore is to avoid the coarsening of particles prior to sintering.

To sum up, the functional and structural properties of the resulting sintered products depend strongly on their microstructure - porosity, grain size and homogeneity - which are themselves determined by the *process conditions* - temperature, holding time and atmosphere and *material properties* - particle size, size distribution and composition.

1.1.4 Local driving force - Solid state diffusion

While the global driving force, as mentioned previously, is the lowering of free energy through elimination of excess surface energy, at the local level, sintering is driven by mass transport at the atomistic level.

In this context, mass transport is mainly ascribed to the *solid state diffusion* mechanisms. When enough thermal energy is made available, mass transport occurs due to the diffusion mechanisms, and the material deposits in the contact area, referred to as *neck*. As sintering progresses, the neck grows further and transforms into a surface contact (**Figure 5**) [12]. The forces driving the diffusion mechanisms are mostly attributed to the gradients of chemical potential, gradients of vacancy concentration and gradients of internal stresses.

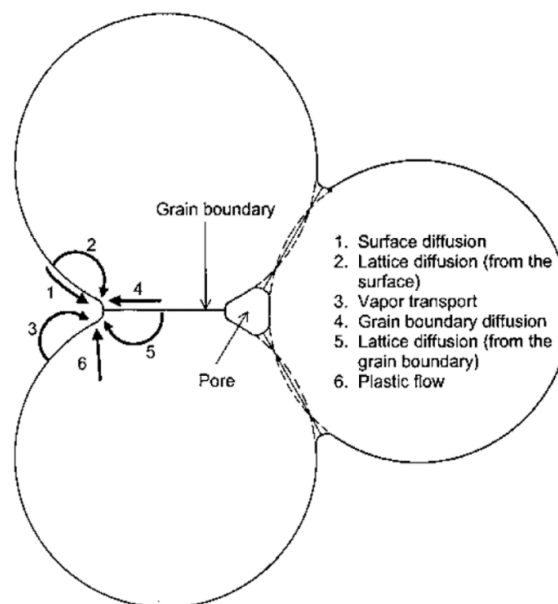


Figure 5. Material transport paths during sintering [12].

The diffusion mechanisms may follow six different paths and are classified accordingly:

Surface diffusion - where the diffusion proceeds along the surface towards the neck,

Lattice diffusion from the surface - where the diffusion occurs through the bulk of the particle from the surface to the neck,

Vapor transport - from the grain surface to the neck through vapor,

Grain boundary diffusion - wherein the diffusion takes place from within the grain boundary,

Lattice diffusion from the grain boundary - taking place through the bulk of the particle, and

Plastic flow - occurring by dislocation motion.

The first 3 mechanisms, referred to as *non-densifying mechanisms*, lead to neck growth without densification as the distance between the particles (*indentation*) does not change during sintering.

The latter 3 are *densifying mechanisms*. They contribute to neck growth as well as densification by material transport between the particles, leading to a reduction in inter-particle distance and thereby shrinkage.

1.1.5 Classical classification of the stages of sintering

Depending on the occurrence and the contributions of these diffusion mechanisms, on general parameters like time and temperature, and on geometrical shape changes, the sintering process is classically divided into three distinct sequential stages (see **Figure 6**).

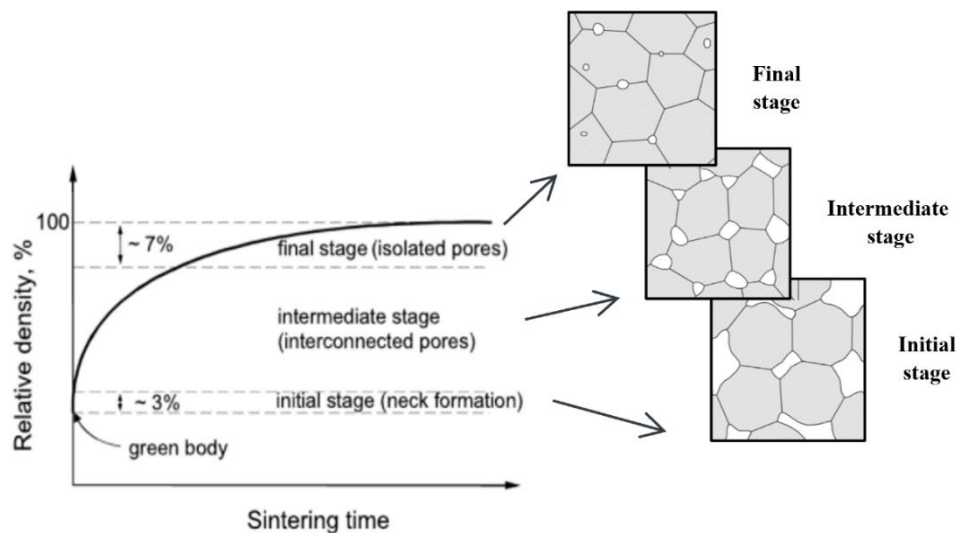


Figure 6. Densification curve and the three stages of sintering [10].

Initial stage: contact area increases from the initial point contact, by neck growth, and the relative density increases up to around 70%,

Intermediate stage: longest stage of sintering during which the relative density rises from around 70% to say, 90%. Pores remain continuous as in the beginning,

Final stage: begins beyond 90% of relative density, when the continuous pore phase tends to get separated into a large number of isolated, almost-spherical pores.

Sintering kinetics are different during these different stages of sintering. Different diffusion mechanisms of mass transport may be operative and aid the different stages as well.

1.1.6 Modeling of sintering - Classical 2 sphere models to contemporary DEM

Over the years, extensive investigations carried out to understand the thermodynamics and kinetics of the phenomena of densification and grain growth, have led to various theories on microstructural evolution, modeling and analyses to predict the path of microstructural development and its dependence on controllable parameters.

At the particle scale level, *analytical methods* were first postulated to model the notion of sintering. Geometrical relationships between two equal-sized monocrystalline grains represented as spheres were derived, with an assumption that these relationships could be extended to the entire packing at the macroscopic scale.

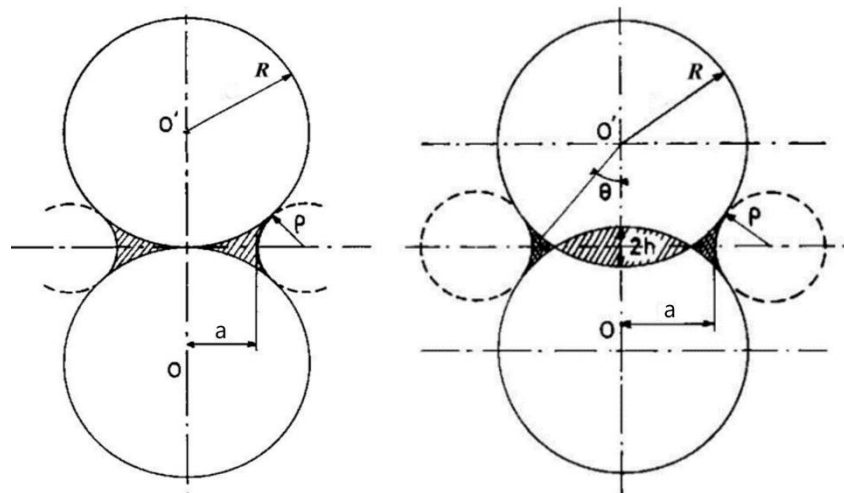


Figure 7. Geometry assumed for initial stage of sintering corresponding to (a) non-densifying mechanisms and (b) densifying mechanisms (Courtesy D. Bouvard).

For the initial stage of sintering, Coble [13], [14] presented a geometrically simple *two-sphere approximation* for the grains for the two different groups of mechanisms as shown in **Figure 7**, by means of tangent spheres for non-densifying and by secant spheres for densifying mechanisms. For the grain with radius R , the geometrical considerations give rise to the classical relation between the indentation h and the neck size a as:

$$a^2 = 2Rh \quad (1)$$

Further, depending on the operating material transport mechanisms, kinetic equations were formulated and developed in their respective works by Frenkel *et al.* [15], Kuczynski *et al.* [16], Kingery and Berg [17], Coblenz *et al.* [18] and Johnson [19]. According to the assumptions

made in their models, their equations follow a similar form, but the values of the constants have a range of plausible values.

These successful approaches to understand the mechanisms of early stage sintering have been summed up by Rahaman [12], introducing a general expression for consolidation (neck growth) and shrinkage during the first stage:

$$\left(\frac{a}{R}\right)^n = \frac{K}{R^{n-m}} t \quad (2)$$

$$\left(\frac{h}{R}\right)^{n/2} = \frac{K}{2^n R^{n-m}} t \quad (3)$$

where m and n are numerical exponents depending on the sintering mechanism and K is a function of the geometrical and material parameters of the powder system and the sintering temperature.

These equations determine the processing variables controlling the initial sintering phase. But, contrary to real powder systems, over-simplification of the geometry and the consideration of only the dominating material transport mechanism make the precision of these equations, especially the constants, debatable and variable.

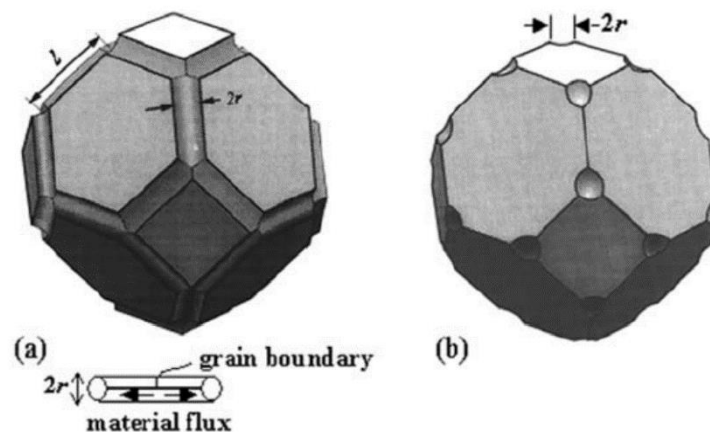


Figure 8. Geometry assumed for (a) intermediate stage and (b) for final stage of sintering [12].

For the intermediate stage of sintering, Coble proposed a *channel pore model* [19] to emulate the densifying grains, with cylindrical shaped pores on its edges to account for the open porosity as shown in **Figure 8** (a). As refinements to Coble's proposal, models for the intermediate stage were subsequently developed by Johnson [19] and Beere [20] to ascertain the intermediate shrinkage state.

For the final stage, closed porosity is represented as spheres of the same size at the corners of a tetrakaidecahedra, referred to as *isolated pore model* by Coble (**Figure 8** (b)) and further developed by Coleman and Beere [21] and MacKenzie and Shuttleworth [22] in their respective studies.

Uniform pore geometry assumed in these models for intermediate and final stage allows the occurrence of only the densifying mechanisms, and the sintering equations are hence commonly expressed in terms of the densification rate.

$$\frac{1dD}{Ddt} = \frac{K_1(1-D)^k}{G^m} \quad (4)$$

where K_1 is composed of certain material parameters, G is the grain size, with $G = 2R$ in equations (2) and (3), and (dD/dt) the relative density rate.

This equation indicates that the densification rate is inversely proportional to a power of the grain size, which is identical to the dependence of neck growth and shrinkage on particle size in the initial stage models.

Analytical models, therefore, yield explicit expressions for the dependence of the sintering rate on primary variables, such as particle size, temperature, and possibly applied pressure, but in view of the drastic simplification used in their development, the models largely provide only a qualitative description of sintering.

As an upgrade, instead of solving the diffusive fluxes analytically with simplified geometries, *numerical tools* were developed in order to track the changes in the grain shapes: one of the prominent tools being the *Finite Difference Method* (FDM).

Preliminary studies used the FDM to analyze sintering between two originally spherical particles and further incorporated a change in their curvature depending on the diffusion mechanisms [23].

Subsequently, Bouvard and McMeeking [24] developed a FDM model to account for the deformation of the particle neck by grain-boundary diffusion, surface diffusion and compressive stress. The numerically obtained results were fitted to an expression that takes the Coblenz equations (2) and (3) as basis. This empirical formula relates the shrinkage rate with the neck size and the neck stress as in equation (5):

$$\frac{dh}{dt} = \frac{\alpha \Delta_{GB}}{a^4} R\gamma_S - \frac{\beta \Delta_{GB}}{a^2} \sigma \quad (5)$$

where $\Delta_{GB} = \frac{\Omega}{k_b T} D_{GB} \delta_{GB}$ (with diffusion coefficient D_{GB} and grain boundary thickness δ_{GB}), σ being the average stress on the neck and α, β the parameters of the model.

Likewise, Pan *et al.* [25] developed a similar FDM model as in Bouvard and McMeeking [24], but kept room to adapt and analyze particles of different sizes. They fitted their results with an empirical equation:

$$\frac{dh}{dt} = 0.5 \left(1 + \frac{r_s}{r_l}\right) \left(\frac{\alpha \Delta_{GB}}{a^4} R\gamma_S - \frac{\beta \Delta_{GB}}{a^2} \sigma\right) \quad (6)$$

where r_s and r_l are the radii of the small and large particles respectively.

Equations (5) and (6) are relevant as they give important information of a sintering contact between two particles for a large range of shrinkage that was used later in other methods.

The study of Pan *et al.* [25] also presented an expression for relating the indentation and the neck size geometrically:

$$a^2 = k \left[0.5 \left(1 + \frac{r_s}{r_l}\right)\right]^\zeta r_l h \quad (7)$$

where k and ζ are fitted empirical values. Unlike the Coble equation in (2), equation (7) is valid for different particle sizes.

Additionally, as mentioned earlier, the densification of a powder compact is normally accompanied by grain growth in the microstructure.

Simple models have been developed to predict the kinetics of normal grain growth, but many of them analyze an isolated grain boundary or a single grain and neglect the topological requirements of space filling.

The densification process and the grain growth process are by themselves very complex and a detailed theoretical analysis of the interplay between the two processes does not appear to be a fruitful approach.

In the traditional sintering theories, the characteristics of grain growth during the middle stage can be expressed as:

$$R = K t^n \quad (8)$$

where R is the mean grain radius, K is a constant and n is the grain growth exponent depending on the diffusion mechanism of the sintering process.

However, in spite of the advances made in modeling the sintering by analytical and numerical models mentioned above, unanswered questions remain. These are mainly due to the phenomenological way of treating the grain-scale motions with restrictive assumptions on particle kinematics. The two-particle systems are thus not adequate to fully explain the sintering behaviors observed in realistic random packing of particles [26].

This is where relatively newer numerical methods like the *Discrete Element Method* (DEM) come into the picture. It has been gaining prominence since the end of the 90's to study sintering at the particle scale for a large set of particles.

A detailed description of the DEM methodology is given below.

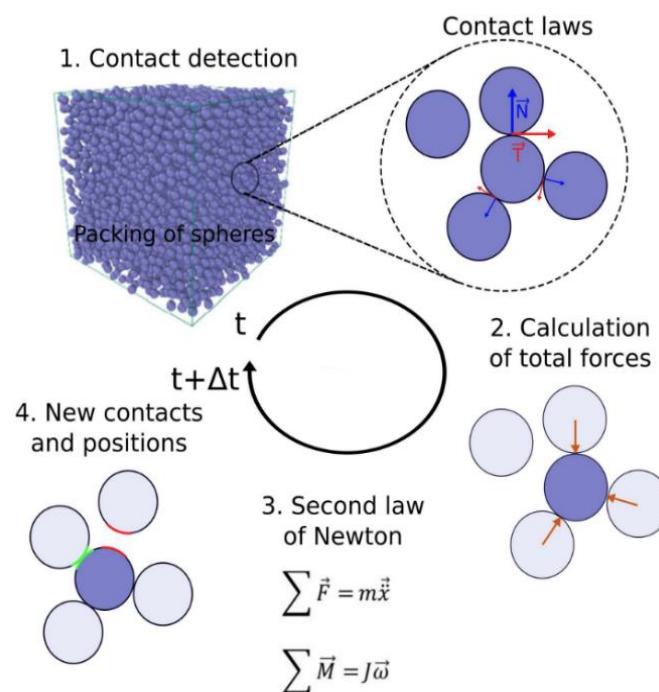


Figure 9. Algorithm of the discrete element method (Courtesy G. Hamelin).

During a DEM simulation, the ensuing procedure is followed at each time-step (see **Figure 9**):

- The granular nature of the material is taken into account by treating every particle as a distinct element and, further, for each of these particles, a list of all contacts with neighbors is created, thus providing a true microscopic approach.
- Contact forces between two particles in contact are calculated analytically taking into account the properties of the particles and the assumed interaction laws. For pressure-less sintering,

DEM models widely use laws derived from 2 sphere calculations such as the one developed by Bouvard and McMeeking [24].

- The movement of each particle (and in turn their new positions and velocities) is calculated using the second law of Newton, with the sum of all the contact forces and moments.
- At each time-step, macroscopic and microscopic physical quantities can now be calculated and saved for future examination.

DEM can thus deal with assumptions associated with analytical models as it explicitly takes the microstructure into account [27]. It also allows access to mesoscopic properties such as the position, velocity, contact area and co-ordination number of every grain [28]. Additionally, by design, it naturally accounts for the rearrangement of the particles and microstructural heterogeneity [29].

Parhami and McMeeking [30] carried out the first DEM approach to study early stage sintering by grain-boundary and surface diffusion, with a packing of a few hundreds of particles.

Later, Martin *et al.* [31] used a similar approach to investigate free sintering of a metal powder system. The simulations were upgraded, to allow for the first time, a large packing of 40,000 micron-sized copper particles.

Further, using DEM sintering models, the influence of the initial microstructure on sintering was analyzed by studying the initial size distribution [32], the original density [33] and the co-ordination number [34].

However, the limitations of the DEM models largely lie in its inability so far in handling complex grain architecture and in modeling the final stages and mechanisms of sintering.

Additionally, such theoretical efforts need experimental data to sustain and to validate their hypotheses. While description of macroscopic behavior is relatively simple to obtain from large-scale techniques like dilatometry, specific area measurements etc., there is essentially a dearth of direct and volumic (3D) microstructure data that can serve as a support to the numerical simulations, especially by providing crucial input data at the micron-scale.

1.2 Experimental Investigation - 3D Imaging

The experimental studies on sintering, in comparison with the theoretical research and numerical simulation, have been picking up speed in recent years.

Classical observation techniques such as optical or scanning electron microscopy (SEM) have been in use since decades to determine the microstructural evolution of sintered powders. The observations were fruitful in capturing the 2D information of the sintered sample, generally followed *post-mortem* i.e. by observing several specimens after pre-defined sintering times [35]. SEMs in particular have now undergone significant improvements in terms of achievable resolutions, making them ideal to witness shape changes of sintered particles.

Nevertheless, the techniques present well-known limitations. Several additional steps, which tend to alter the internal microstructure, such as cutting and grinding of the cross-sections of the sample, polishing the surface etc. are a pre-requisite for an SEM observation.

Further, *in-situ* SEM analysis, aimed at following the microstructural changes of powders in the course of sintering is hard to achieve because of the practical difficulties in reaching higher temperatures inside the experimental set-up. Also, owing to the difficulty in directly observing the processes, investigations have not been effective in capturing various operative mechanisms [36].

However, in the recent decades, the usage of non-conventional characterization techniques, like X-ray tomography has been on the rise. These techniques, due to their significant non-destructive abilities, are able to provide a 3D as well as a good resolution information of the morphology of the microstructures.

As an upgrade, using the synchrotron X-ray tomography technique, observation of the material in real time under the action of an external field such as thermal or mechanical loading becomes possible.

In this aspect, even though considerable progress has been achieved with regard to metallic powders, the experimental work has not yet attained a satisfactory level with ceramics, and numerous questions remain unanswered.

Hence, researching the internal microstructural evolution and studies on the microstructural improvement of the ceramic materials are essential for enhancing the production process as well as for improving the overall material properties.

1.2.1 Advances in 3D imaging - Metallic powder sintering

Given that the metallic powders are generally composed of almost-spherical and regular particles, with a range of around 10 - 100 μm , micro-computed tomography (μCT) apparatus are well suited to capture the intricate details at the particle length level.

Extensive research has been carried out in the μCT facilities available at the laboratories and in the synchrotron radiation facilities for the past few decades. The 3D images from the μCT investigations have been very valuable in thoroughly investigating the phenomena associated with metallic sintering.

In addition to the several ex-situ μCT experimentations carried out on metallic powder systems, focus has shifted towards imaging in-situ in the recent years, to capture the ongoings in real time.

Lame *et al.* [35] reported the first in-situ observations of a loose copper powder sintering using synchrotron μCT . Meaningful information was drawn concerning the initiation of inter-particle neck growth, the rearrangement of particles and residual pores resulting from differential densification in the sintered material (**Figure 10**).

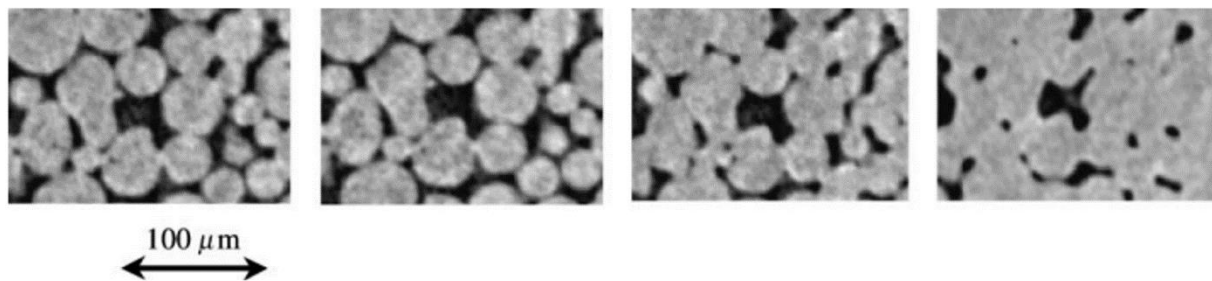


Figure 10. 2D reconstructions showing copper particles at different stages of the sintering [35].

Nöthe *et al.* [37] used μCT to prove the existence of particle rearrangement during metallic powder sintering. In subsequent studies, they coupled μCT with photogrammetric image analysis to track the positions of all particle centers to follow the metallic particles at various stages of the sintering process .

Vagnon *et al.* [38] employed real time tomography to investigate the sintering of similar mono-sized closely packed metallic powder systems to quantify relevant sintering parameters. A complete set of morphological characteristics was developed for the 3D quantitative analysis of the local microstructural parameters and was followed throughout sintering. The data

analyses proved that the sintering was quite homogeneous in nature and subsequently were used to validate classical models with the experimental data.

Particularly rewarding has been the follow-up of the pore size distribution in the course of sintering by Olmos *et al.* [39] for a more complex copper-based powder system (**Figure 11**).

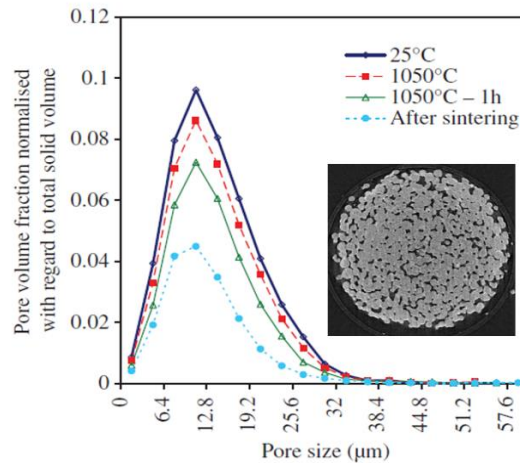


Figure 11. In-situ observation of pore size distribution of copper powder sintering [39].

It was demonstrated that in-situ X-ray μ CT was especially appropriate for gathering data on collective particle behavior during sintering.

Advancing on Nöthe *et al.*'s work mentioned above [37], high-resolution synchrotron X-ray tomography experiments were carried out in-situ to measure translational, rolling and rotation parameters of powder particles in a 3D packing of some hundreds of spheres during sintering. This accounted for a thorough analysis of the cooperative material transport processes. Additionally, occurrence of mechanisms such as grain boundary sliding caused by different crystallographic orientations were observed [40].

Kieback *et al.* further presented detailed insights on intrinsic rotations of the particles via synchrotron computer tomography. In-situ data of particle rearrangements were acquired which were later used to build a new rotation model [41].

Consequently, in the last decades, in-situ analysis by μ CT has been found to be very productive in improving the overall understanding and modelling of metallic powder sintering.

1.2.2 3D imaging complexities - Ceramic powder sintering

The same outcomes as in metallic powders cannot be realized for ceramic powders because of the typical size of their individual particles, which is around 1 μm or less, i.e. at the resolution limit of μCT . In comparison with their metallic counterparts, individual ceramic particles are generally of irregular shapes as well. Also, indeed, as a consequence of this small size, ceramic particles most often form agglomerates. In turn, the scale of grain growth is much more intense compared to metals, which further limits the usage of conventional μCT for ceramic sintering investigation.

In this regard, in the late 90's and early 2000's, CT experimentations provided preliminary understanding on the interpretation of the bulk behavior of ceramic powder systems. Better understanding of ceramic powder compaction and densification was provided through CT studies, leading to the resolution of expensive powder pressing issues [42]. CT analyses were shown to offer effective quantitative access to internal density distributions during compaction [43]. X-ray CT was further used to quantify the internal structure of the compacts, resulting in pore characterisation and pore distribution analyses [44].

The above works demonstrated the huge potentiality of the CT technique for the assessment of ceramic sintering phenomena. Due to the vast improvements that were subsequently made in micron-scale measurements and in 3D visualizations, X-ray μCT techniques have been utilised for thorough ceramic processing.

Bernard *et al.* employed X-ray μCT on ceramic samples of different materials to directly visualize, for the first time at that scale, 3D microstructural evolutions during sintering [45]. Certain preliminary quantitative measurements were also performed on the 3D images obtained.

Subsequently, attempts have been made to track ceramic sintering mechanisms in-situ using synchrotron radiation facilities.

Notably, a real time observation of the microstructural evolution of silicon carbide agglomerates during sintering has been accomplished by synchrotron X-ray tomography and basic sintering related parameters were quantified as in (**Figure 12**) [46].

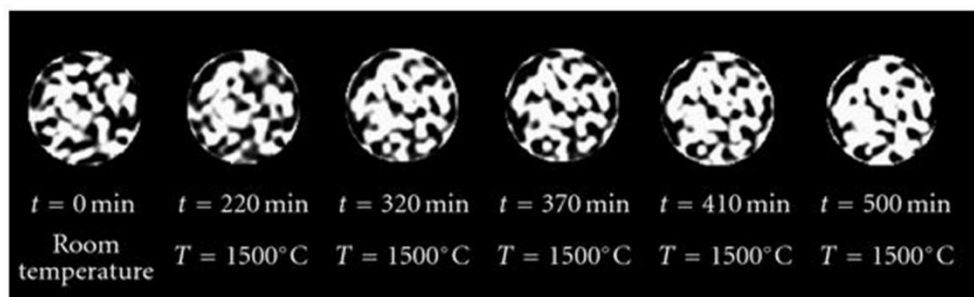


Figure 12. Reconstructed images of the same cross-section of the sample at different sintering periods and temperatures [46].

In another set of experiments, grain growth evolution of boron carbide powder during isothermal sintering was investigated in-situ at an agglomerate level as well (**Figure 13**) [47].

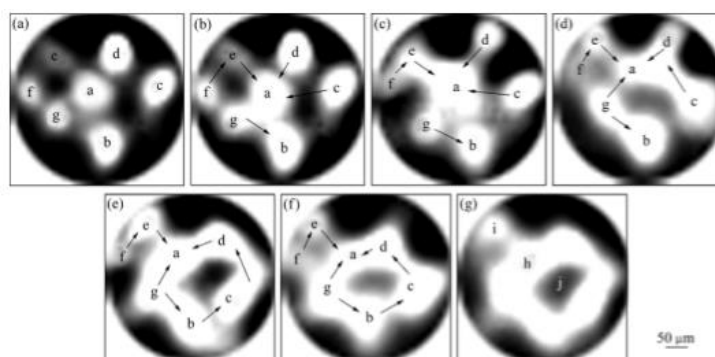


Figure 13. Reconstructed images of the same cross-section of the sample at different sintering periods and temperatures [47].

However, more recently, interparticle neck growth during the sintering of glass beads with a sintering temperature of 670°C has been monitored at the nano-scale (**Figure 14**), opening the way for comprehensive ceramic studies [5].

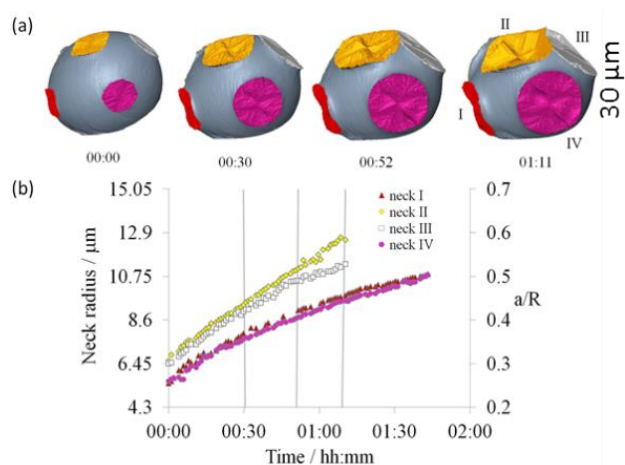


Figure 14. In-situ observation of glass bead sintering. (a) neck growth (b) Evolution of neck radii with time [5].

Likewise, the relevance of X-ray tomography investigation in ceramic sintering is stressed in the recent review work of Wakai *et al.* [48]. Added to that, tools of X-ray nano-tomography are being exploited for a variety of ceramic studies of late. To name a few, works by Yan *et al.* [49], Okuma *et al.* [50]–[52] etc.

Several other literary references are provided in accordance with the subject in hand in the introductory sections of **Chapter 3, 4, 5** and **6**.

1.3 Premise and Objectives

As established, ceramic powders exhibit greater complexities to be 3D imaged compared to metallic powders due to the fine and irregular architecture of their individual particles.

The resolutions attainable as a result of the μ CT advancements in the early 2000s were instrumental in furthering investigations on sintering of metallic powder systems and in realizing novel understandings in this research area. These resolutions, however, are not sufficient enough to examine the intricacies involved in ceramic sintering. Consequently, the experimental investigations and the outcomes are lagging behind compared to the progress achieved with their metallic counterparts.

To the best of our knowledge, both the ex-situ and in-situ μ CT investigations conducted so far on sintering of ceramic systems have been confined to the agglomerate level.

No in-situ tomography of ceramic sintering, in the real sense, at the local level, has been performed so far.

The studies conducted with lower resolutions at the agglomerate level, even though beneficial in their own right, have been compelled to a variety of limitations. A lot of work has been restricted to only the initial stages of sintering, as they were not well-equipped to handle the complications developing at the latter stages. The experiments have also been bound to sinter relatively coarser powders for the same reason.

These shortcomings thus provoke and promote a deeper understanding of ceramic sintering at the particle length-scale.

The particulars at the local level simply cannot be ignored as they might shed light on some deeper intricate details, remaining unknown for now. Accurate observations on the initiation

of various mechanisms, together with the collective behavior of the particles at the local level would certainly benefit us in expanding our overall know-how on the subject.

A much better resolution is therefore required for their 3D imaging; and, drawing inspiration from the experiments on glass beads mentioned just previously [5], the way out is thus to take advantage of the emerging X-ray nano-tomography (nano-CT) technology.

Synchrotron facilities with nano-imaging capabilities are now equipped to reach super high resolutions with voxel sizes in the range of a few dozens of nanometers and shorter scanning times - with significant and consistent path-breaking improvements in the last few years.

With a higher resolution, we should be able to work with finer ceramic powders as well as investigate denser structures, thus allowing us to analyze intermediate and final stages of sintering.

Nevertheless, real-time observations would still pose difficulties due to constraints in the existing experimental set-ups. The analyses would remain delicate because of the high temperatures required. Practical issues with regard to the extent of the time period of the experimentations will have to be taken into account as well.

Above all, it is an uncharted domain: there is no sufficient documented literary evidence - no indication of previous endeavors or expertise!

In this project, therefore, we will explore the X-ray nano-tomography technique by taking advantage of the resolutions and the scan times available at one of the nano-probes at the European Synchrotron Radiation Facility (ESRF) - to attempt at fixing the existing gaps in ceramic 3D imaging investigations.

An experimental outline will be devised to first adapt the existing X-ray nano-tomography methodologies *to investigate pre-sintered representative samples in a post-mortem context*. The 3D images obtained subsequently would offer quantitative insights into various sintering phenomena. Evolution of different parameters at different conditions would provide enough information for further comparison and evaluation.

As a further significant upgrade, the expertise gathered from the post-mortem experimentations will be channelized to develop a novel framework, with a view *to perform the first set of in-situ observations at higher resolutions during the course of ceramic sintering*.

In this regard, a furnace capable of operating at high temperatures (~1500°C), which would fit the beamline environment and the control system has to be developed. The compact nature of the furnace required to suit the synchrotron specifications would further enhance the prevailing challenges.

The subsequent quantitative analyses would enable us to monitor the sintering mechanisms in real time, providing us with the comprehension of the collective behavior of particles, including that of inter-particle neck growth, grain growth and pore changes, for several representative powder systems.

The data thus obtained by following the microstructural changes of the powders during sintering could be used *to analyze the applicability of classical sintering theories and models* - they could be of help in validating or/and improving them. The collected data would also serve as a precious help to make the existing numerical models such as DEM more realistic.

For a consistent comparison of experiments and simulations, in-situ data will thus be an undeniable advantage.

The final part of the work would be devoted *to explore the constrained sintering mode*, which remains fairly untapped so far. In the pressure-less free sintering mode discussed earlier, the material properties are homogenous and isotropic and so no internal stresses develop during densification. However, most real industrial processes involve, for example, composite materials with different densification rates, powders comprising of agglomerates and/or rigid inclusions, films sintering on substrates, or layered or graded structures with different densification rates. In these realistic conditions, constrained sintering occurs - by mismatch in the local sintering rates, either within the sintering material or between the sintering material and a substrate [53]. The mechanisms involved in such cases are still not fully understood.

In this regard, we will take into consideration one of the aforementioned cases of constrained sintering mode, *to investigate agglomerated ceramic powders mixed with inclusions, by in-situ X-ray nano-tomography*. This part of the work would be beneficial in understanding the factors preventing complete densification of the compact and in turn leaving defects in the final material. These defects are known to be detrimental to the mechanical and physical properties of the sintered parts and a thorough probe is thus mandated.

These experiments, on the whole, will hence provide us with, as far as we know, the first 3D images obtained by in-situ X-ray nano-tomography at the particle length-scale with real ceramic powders. *Simply viewing the image sequences will be rewarding enough - the novel information on sintering mechanisms they are expected to offer is an add-on!*

CHAPTER-2

EXPERIMENTAL METHODOLOGY

2.1 Process Outline

2.1.1 Powder system under consideration

Alumina powders are the most widely used in the world for oxide ceramic applications. Their versatility and reliability have made them a go-to material for sintering experiments and applications. They exhibit excellent physical and chemical properties, such as good heat, wear and corrosion resistance.

However, the microstructure of alumina powders, generally obtained by the conventional Bayer process, is usually complex, irregular and agglomerated. This is quite a hindrance to a systematic microstructural examination. A ceramic powder, if mono-dispersed, with a uniform and regular particle shape, like many of its metallic counterparts, while retaining all of its functionalities, of course, would be ideal for sintering studies and make things a lot easier.

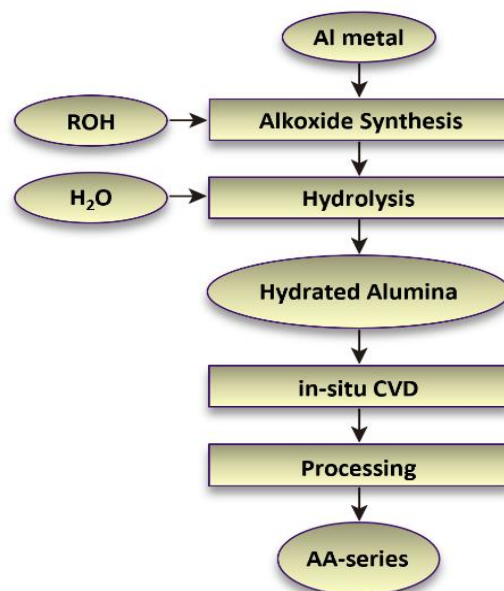


Figure 15. Manufacturing process of advanced alumina by alkoxide method.

One of the products that meets these criteria is the *High Purity Alumina* (HPA - 99.99% pure), manufactured by *Sumitomo Chemical Co., Ltd.* Sumitomo provides an alternative route to produce alumina by a unique method called *aluminium alkoxide hydrolysis* method (**Figure 15**). The products are advertised as having an almost-spherical shape, being nearly mono-dispersed and homogeneous, along with having good packing properties and a precisely controlled particle size distribution.

Aluminium hydroxide (hydrated alumina) made from high purity aluminium metal and alcohol (ROH) is the source of HPA. The Advanced Alumina (AA) series - one of the core products of HPA - is then synthesized by chemical vapor deposition (CVD). In the CVD furnace developed by Sumitomo, the particle size is controlled by adjusting the gas atmosphere, temperature and time. This process is distinctive in that the alumina particles are synthesized in uniform particle size, because of the uniform vapor deposition achievable throughout in the furnace.

The resulting almost-rounded polyhedral particle shape promotes thermal conductivity, and hence finds applications in thermal interface materials (TIM). Further applications include ceramic filters, plasma sprays and other high strength, high-density ceramics. In addition, according to Sumitomo, the AA series of powders are supposed to have isotropic, uniform and fairly non-agglomerated features. They are available in a wide range of sizes from ~0.4 to ~20 microns to meet various customer needs.

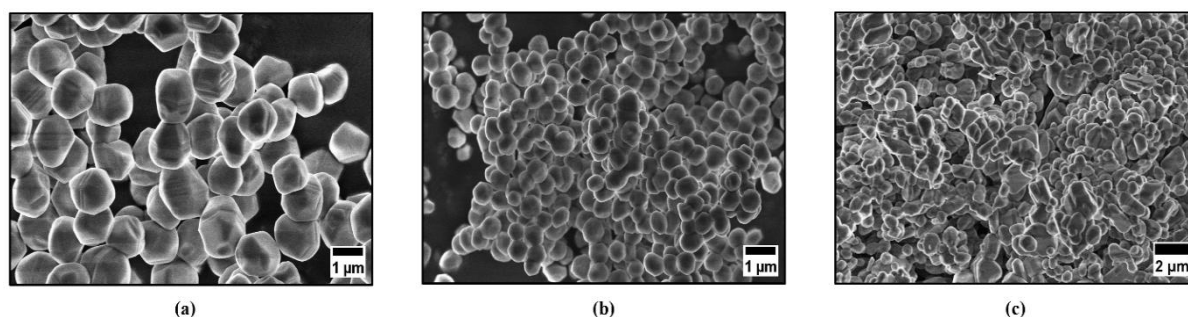


Figure 16. SEM observations of the advanced alumina (a) Al 1.3 μm and (b) Al 0.7 μm , respectively. (c) Another typical ceramic powder system, for a comparison.

In this thesis, we have chosen two of these powders, *AA-1.3* and *AA-07*, with average particle diameters of 1.3 and 0.7 μm , respectively, as seen from our SEM observations with an ultra-Zeiss 555 (**Figure 16** (a) (b)). These powders are hereon referred to as ‘Al 1.3 μm ’ and ‘Al 0.7 μm ’.

The sizes of these particles are compatible with the highest resolution attainable currently in the nano-imaging beamlines at the synchrotrons. Moreover, they have lower sintering temperatures than conventional alumina powders and are expected to form dense ceramics at around 1500°C. These temperatures are achievable in standard dilatometers for our preliminary sintering trials. The simplistic shapes they possess should be relatively easier for the subsequent image analysis as well. These superior characteristics thus make it a promising starting material for the first set of sintering studies in this work.

In addition, for the next set of experiments, with the objective of going towards *complex powders*, a commercial ZnO powder was used. The *ZnO system* (average size of ~200 nm from *Carlo ERBA*) is a collection of agglomerated and complex shaped nano-particles.

Further, to set up a constrained system, bigger *alumina inclusions* (average size of 22 μm) were chosen.

SEM pictures of both the powders are shown in **Figure 17** (a) (b). The analysis of these images is expected to be rather complex due to the morphology and size distribution of the particles.

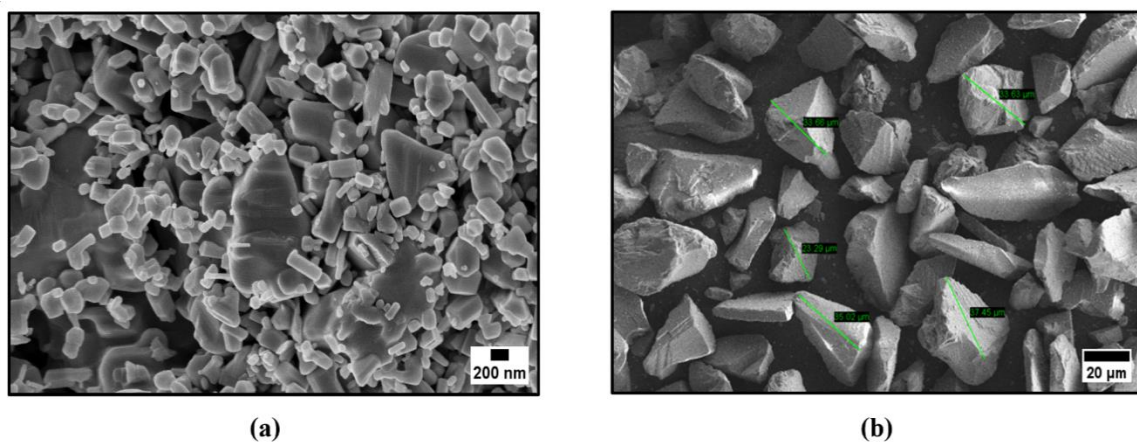


Figure 17. SEM observations of the (a) ZnO powder and the (b) bigger alumina system.

2.1.2 From powders to green compacts

As is the case with the general sequence of operations involved in powder metallurgy, the component powder is first mixed together (with a *binder*, if needed) until a homogeneous mix is obtained. The mix is then loaded into a die and compacted under pressure, to get the *green compact* (**Figure 18**). A *lubricant* often finds a role in the process to reduce the friction between the powder mass and the surfaces of the tools of the die - die walls, core rods, etc., along which

the powder must slide during compaction, helping achieve the desired uniformity of density from top to bottom of the compact. Reduction of friction also makes it easier to eject the compact and the chances of crack formation in the compact is minimized. The final compact density needed to achieve the desired properties determines the minimum pressure that must be applied in the die. Also, prior to sintering, the compacts must be strong enough to withstand ejection from the die and the subsequent handling, thus making this a crucial step.

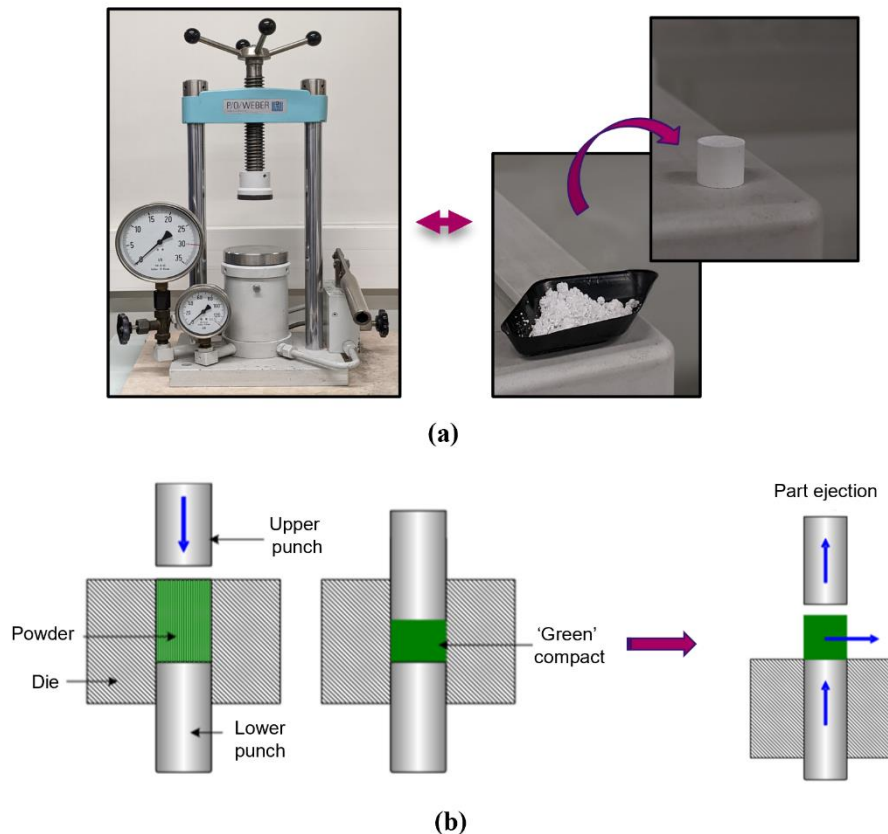


Figure 18. (a) Photograph of the WEBER compaction die, utilized to transform the powder in hand into a green compact, (b) Illustration of compaction process in a die (Courtesy D. Bouvard).

Likewise, here, the compaction process for alumina and ZnO compacts involves slightly different parameters depending on the type of material and the desired final density. For alumina compacts with AA-1.3 and AA-07, a binder of polyvinyl alcohol was added to the mixture in small quantities. The mixture was then uniaxially pressed in the rigid die (*P/O/Weber*) at a pressure of about 200 MPa, resulting in cylindrical compacts (with a diameter of around 8 mm) with a desired density of ~60% (by mass-volume calculations). For ZnO compacts, the target density was 50%. So, a lower pressure of about 60 MPa was applied. A lubricant of stearic acid mixed with acetone was also used for the die. The final density of the

ZnO compacts read ~52%. However, when 20 vol% of alumina inclusions were added to the ZnO mixture, following the same steps, the density decreased, as expected, to ~50%.

2.1.3 Thermo-mechanical analyses - From green compacts to sintered ones

As a preparation for the nano-tomography experiments, to assess the sintering behavior and advancement of the ceramic powders, die-pressed compact versions of them were sintered in a *dilatometry* set-up by applying thermal cycles. These preliminary trails were run with the facilities of the lab to identify the relevant sintering conditions of every powder that will result in significant densification and microstructural changes.

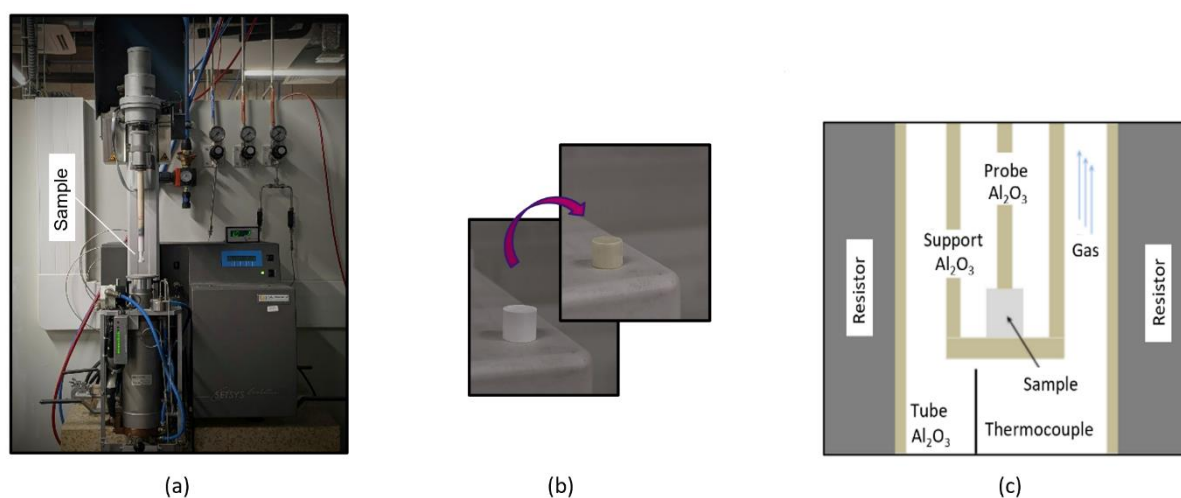


Figure 19. (a) Photograph of the SETARAM dilatometry system, and (c) schematic of the internal part of a dilatometer, (b) creating the sintered compact from the green compact.

Dilatometer records the dimensional changes (most often shrinkage) that take place during the sintering operation.

SETARAM's SETSYS Evolution - 1750 CS was employed for this purpose (**Figure 19** (a)). Internal schematic in the **Figure 19** (c) shows the components of a dilatometer. It consists of a resistance furnace with a maximum temperature of 1600°C and a possible atmosphere control. The green compact is to be placed in the designated holder as shown. Various full thermal cycles are imposed on to the powder under a suitable atmosphere. An LVDT sensor measures the displacement of the push rod (Probe Al_2O_3 in **Figure 19** (c)) in contact with the upper surface of the green compact. The variation in the height of the specimen at any time of the thermal cycle is deduced. With about a 4 μm accuracy, height variation is measured in a ± 2000

μm range. To guarantee the rod's contact with the compact, throughout the test, a constant load of 2g is applied upon it.

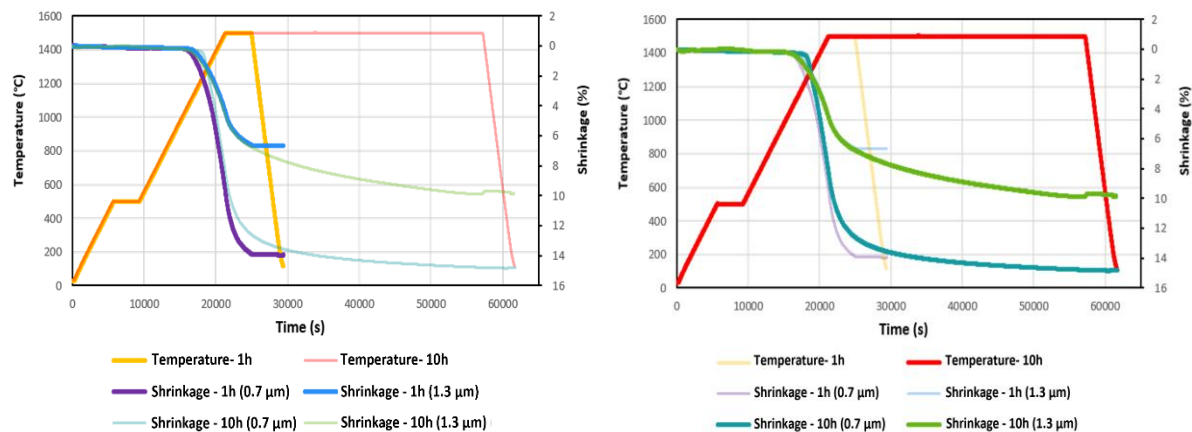


Figure 20. (a) (b) Thermal cycle and dilatometry curves for Al 0.7 μm and Al 1.3 μm , at 1h and 10h at 1500°C, respectively.

Different temperature vs. displacement curves are obtained by playing with the heating rates, the temperature, the period of isothermal condition etc. The resulting shrinkage and densification in the compact are recorded through a thorough analysis of the dilatometry curves. This is supplemented with the density measurement of the sintered compact by using *Archimedes' principle*. During the trial, the push rod is subjected to thermo-elastic deformation as well and hence a blank test is necessary to get the absolute height variation in the specimen.

As an example, thermal cycles such as the one in **Figure 20** (a) (b) are applied to the die pressed alumina compact with 0.7 μm and 1.3 μm particle sizes. They are sintered in air at 1500°C with isothermal periods of 1h and 10h respectively. A brief isothermal period is carried out at 500°C to remove the initially added binder. When sintered at 1500°C for 1h, the powders attain a final relative density of 92% and 74% respectively, while, when sintered for 10 hours, they reach 94% and 81%. As seen from the curves, therefore, Al 1.3 μm undergoes a shrinkage of ~10% in the end after 10 hours, while Al 0.7 μm shrinks much more, by about 15%.

A representational picture of one such case showing the transformation undergone in a dilatometry trial was shown in **Figure 19** (b).

The density and shrinkage estimation gives us a hint as to what stage of sintering we are in. We prepared various such samples accordingly, sintered at different stages of sintering. These

were broken into tiny fragments (fitting the synchrotron criteria) for the subsequent nano-tomography post-mortem investigations. In the case of alumina 0.7 μm , samples were sintered at 1500°C, with an isothermal treatment for 30 min, 1 h, and 10h respectively. For Al 1.3 μm , sintered samples corresponding to 1h, 10h, 30h and up to 120h at 1500°C were prepared. Whereas, the ZnO powders were sintered at temperatures of 700, 800 and 1000°C, respectively, depending on their sintering temperature range and the feasibility of the tests at the synchrotron.

For the sake of completion, the following section briefly provides an outline and summarizes the two kinds of experiments that were performed in this thesis. The very next section will explain the science behind synchrotrons and the experimental procedures in depth.

2.1.4 Post-mortem experiment scheme

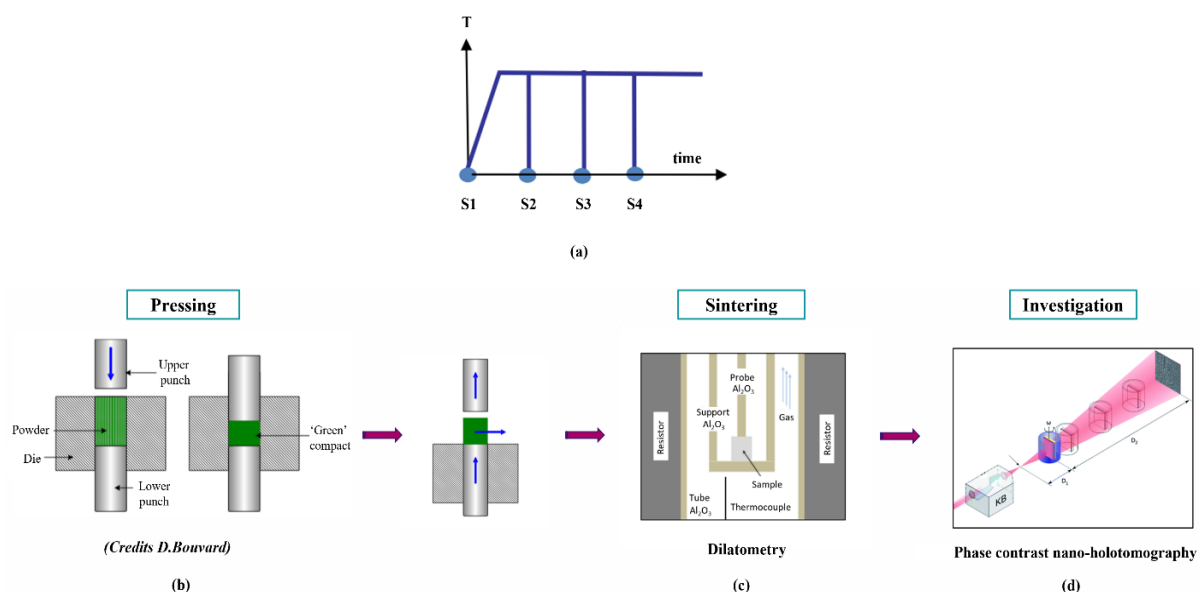


Figure 21. (b) (c) (d) Process overview of a post-mortem X-ray tomography experiment, with an illustration in terms of a graph (Credits: L. Salvo) in (a).

The experimental procedure (**Figure 21** (b) (c) (d)) for post-mortem analysis consists of these steps: First, the pressed die compacts are sintered in a dilatometer for different durations to obtain samples corresponding to different densities (i.e., different stages of sintering). Next, the sintered samples are broken into tiny fragments that can fit into the synchrotron criteria. Then, the fragments are scanned at room temperature in what is referred to as post-mortem investigation - a technique that allows the observation of the microstructure of a material after

it has undergone thermal or mechanical treatment. By comparing the tomographic images of different samples, the effects of sintering time and treatment type on the material properties can be studied.

The graph above (**Figure 21** (a)) shows a typical nature of the post-mortem analysis process. Four different samples S1, S2, S3 and S4 are subjected to heat treatments at different times, and T denotes thermal treatment.

2.1.5 In-situ experiment scheme

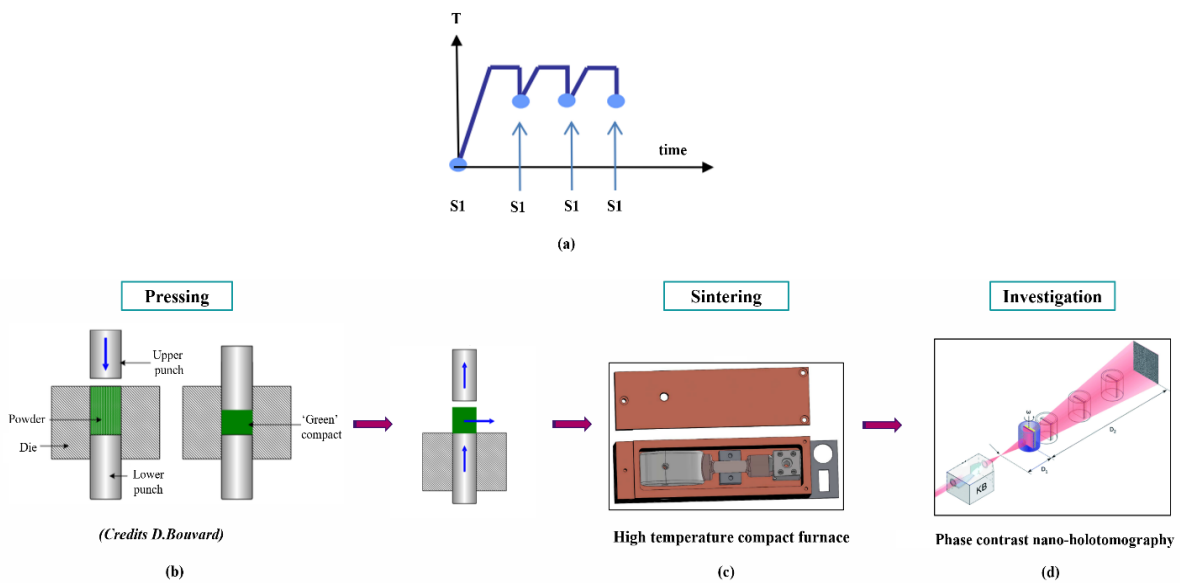


Figure 22. (b) (c) (d) Process overview of an in-situ X-ray tomography experiment, with an illustration in terms of a graph (Credits: L. Salvo) in (a).

For the in-situ investigation, unlike post-mortem, the green compact itself is broken into tiny fragments and sintered directly in the synchrotron using a high-temperature compact furnace (**Figure 22** (b) (c) (d)). More on the design and development of the furnace in the next section.

The sintering process was monitored in-situ but in an interrupted fashion. The technique allows scanning the same sample during different stages of heat treatment. Imaging was not done continuously, owing to the time needed for a full-scan. Further details are provided in **Chapter 4**. **Figure 22** (a) shows a graph of the in-situ analysis process for the same sample S1, where T denotes thermal treatment.

2.2 Science of Synchrotrons

X-rays are a very useful tool to investigate the material world, as they can reveal the structure and properties of matter at different scales. One of the premier examples of X-ray tools are the Synchrotrons. Simply stated, Synchrotrons are large-scale sources of very intense, or *brilliant* electromagnetic radiation across a broad range of wavelengths. The underlying principle - accelerating charged particles, such as electrons, in circular orbits to very high speeds and energies, and then forcing these particles to change direction by magnetic fields, which makes them emit electromagnetic radiation, also known as *synchrotron light*. Synchrotron light is increasingly finding applications in various fields of science, such as physics, chemistry, biology, medicine and materials science.

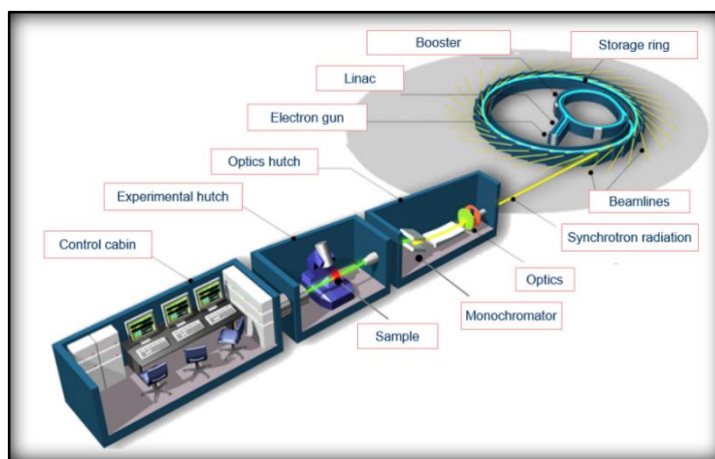


Figure 23. Overview of the components of a synchrotron facility (© Synchrotron-SOLEIL).

The main components of synchrotrons, as in **Figure 23**, are: *Electron gun* - source of electrons, with a heated metal filament ejecting electrons via thermionic emission. These electrons are then accelerated in an evacuated linear accelerator, *LINAC*. The electrons then enter the so-called *Booster ring*, in which their energy is further ramped until they attain the desired energy of the main *Storage ring*, into which they are injected and stored. The storage ring maintains the energy and stability of the electron beam. The electrons are required to remain on a closed path in the booster and storage ring, which is achieved using *Bending magnets* (BMs). They force the electrons to execute a curved trajectory, causing them to emit electromagnetic radiation. In addition, there are straight sections between the BMs called Insertion devices (IDs). IDs can be alternating arrays of magnets (wigglers or undulators) that make the electrons oscillate and produce more intense or coherent radiation. The energy of the emitted X-rays can be tuned with these undulators. Tangential to the IDs and BMs are the *Beamlines* that transport

and manipulate the radiation, normally X-ray beams, from the storage ring to the experimental stations. There can be many beamlines in a synchrotron facility, each serving different scientific fields or applications. A beamline is constituted by at least an optical hutch and one or several experimental hutches. The optical hutch is composed of optical elements such as mirrors, monochromators, lenses etc. in order to tune the beam according to its uses. The experimental hutches include devices to focus the beam if needed (zone plates (FZP), compound refractive x-ray lenses (CRL), Kirkpatrick-Baez (KB) mirrors etc.), sample stage and detector systems.

The quality of a measurement using X-radiation depends, among other parameters, on the *brilliance* of the source, which is a term that encapsulates four desired attributes of X-radiation: intense, as monochromatic as achievable, parallel and emanating from a small source. Synchrotron radiation sources have much higher brilliance than medical or laboratory sources, which therefore makes them far superior for X-ray-based measurements.

2.2.1 ESRF's nano-analysis beamline - ID16B

ESRF - The European Synchrotron Radiation Facility, at Grenoble, France, is one such center of excellence for fundamental and applied research, with *the most intense synchrotron light source in the world*. And, one of its nano-analysis beamlines, *ID16B*, is where we got the opportunity to conduct our set of X-ray nano-tomography (nano-CT) experiments. It provides state-of-the-art X-ray nano-analysis and imaging, offering a multi-modal approach (X-ray fluorescence and spectroscopy, X-ray diffraction, X-ray-Excited Optical Luminescence (XEOL) and X-ray Beam Induced Current (XBIC), and phase contrast 3D imaging) for the full and simultaneous characterization of the samples with: nanometer-scale spatial resolutions (~ 50 nm), monochromatic beam tunable in a large excitation energy range (5–33 keV), with high flux (10^9 to 10^{12} photons/second), a range of detection schemes and a large flexibility, with in-situ experimentation capabilities.

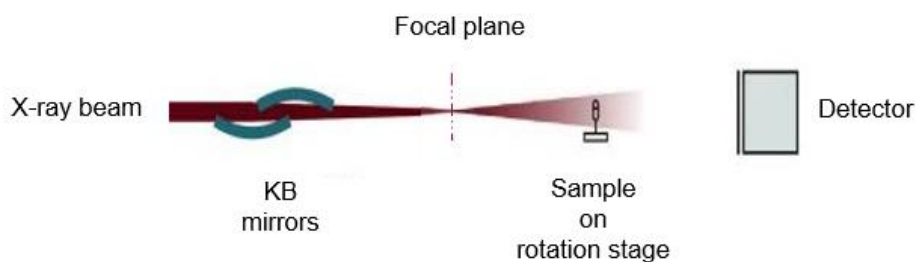


Figure 24. Schematic of the nano-CT setup at ID16B beamline of the ESRF.

ID16B's design integrates high-performance focusing optics, high-precision sample stage, and efficient detection schemes, all within a temperature-stabilized environment. A schematic of the experimental configuration for nano-CT at the ID16B facility is provided in **Figure 24**. The intense X-ray beam is focused down to a spot size of $50 \times 50 \text{ nm}^2$ using KB mirrors. This focused beam acts as a source for a conic beam projection geometry. The sample stage has motorized translation and rotation stages for precise, smooth and continuous motions. The detection system possesses, among other variants, a *scintillator screen* (LSO 17m) that converts X-rays into visible-images, an *Olympus objective x10*, and a *pco.edge 5.5 CMOS camera* enabling a fast and continuous image acquisition.

A detailed overview of the nano-probe, with more information on the optical arrangement can be found in Martinez-Criado *et al* [54].

In a recent upgrade, a new *fast in-situ 4D imaging tool* has been incorporated into the beamline, combining the nanometer pixel size resolution with a faster acquisition time ($<10\text{s}$) [5]. The relatively large free space available for samples allows the development of various sample environments. The first scientific results obtained demonstrate the great potential of the upgraded ID16B facility, in particular, its in-situ capabilities [55]–[59].

2.2.2 Imaging concepts - Tomography

Simply put, the aim of *X-ray tomography* is to use X-rays to penetrate inside objects and generate a 3D computer model of the same. Cross-sectional slices (or, radiographs) produced by the projections of the X-rays from different angles are stacked together and reconstructed into a 3D volume using mathematical algorithms. The X-rays are absorbed and attenuated by the object and the detectors measure the intensity of the remaining X-rays.

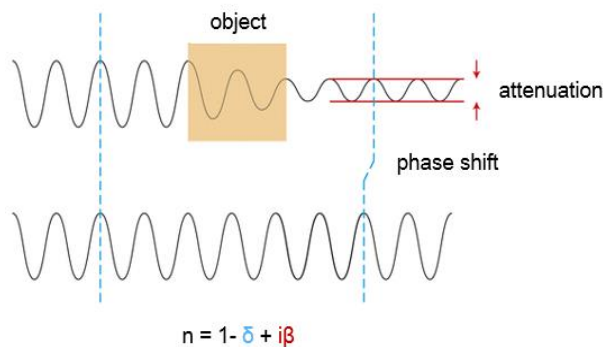


Figure 25. Illustration of the attenuation and the phase shift undergone by an X-ray wavefront [60].

In this work, however, rather than conventional tomography, we employ a *phase-sensitive tomography set-up*.

When an X-ray beam penetrates an object of refractive index ‘n’, the X-ray waves not only undergo attenuation by absorption but also the phase of the X-ray wavefront shifts, depending upon the density distribution of the object (**Figure 25**) [60]. Refractive index is given by $n = 1 - \delta + i\beta$, where δ is the refractive index decrement and β the absorption index. While δ is related to the phase shift of the incident beam brought on by the object's deflection, β is related to the attenuation of the incident beam induced by the object. *Phase-contrast* and *absorption-contrast*, two alternative contrast modes employed in X-ray imaging, are based on these two phenomena respectively.

In absorption-based methods, the detectors are required to be very close to the sample - the magnification is then limited by the optics. Phase-contrast imaging can achieve a pixel size of 25 nm, thanks to the geometrical magnification, while exploring the phase-contrast aspect with the detector far away from the sample. Phase-contrast imaging is hence favored here over conventional absorption-based techniques, mainly because it can reach high resolution as well as it can be much more sensitive to weak density variations, enabling the detection of intricate details and extraction of different phases in an object.

2.2.3 Phase-contrast X-ray nano-holotomography

At ID16B, the conic beam geometry results in a geometrical magnification, and phase-contrast is obtained by letting the X-rays propagate after the interactions with the sample. This sets up a case for a *propagation-based imaging* in *holotomography* configuration, where images can be recorded at several object-to-detector distances (**Figure 26 (a)**) [61]. Different magnification factors can be achieved by moving the sample in relation to the focal plane, i.e. distance D_1 , while keeping the detector, which records the interference patterns, fixed, i.e. $D_1 + D_2$ remains fixed.

In our experiments, we employed two types of scenarios for each sample. First, we performed lower resolution (100 nm) scans using a 1-distance formula to get a global view of what we are looking at in the sample. Once satisfied, we performed higher resolution (25 nm) scans with a 4-distance formula to zoom into a much smaller region for detailed visualization. In this case, 4 different sample-to-focus distances are used, and at each distance, a complete tomographic scan is performed.

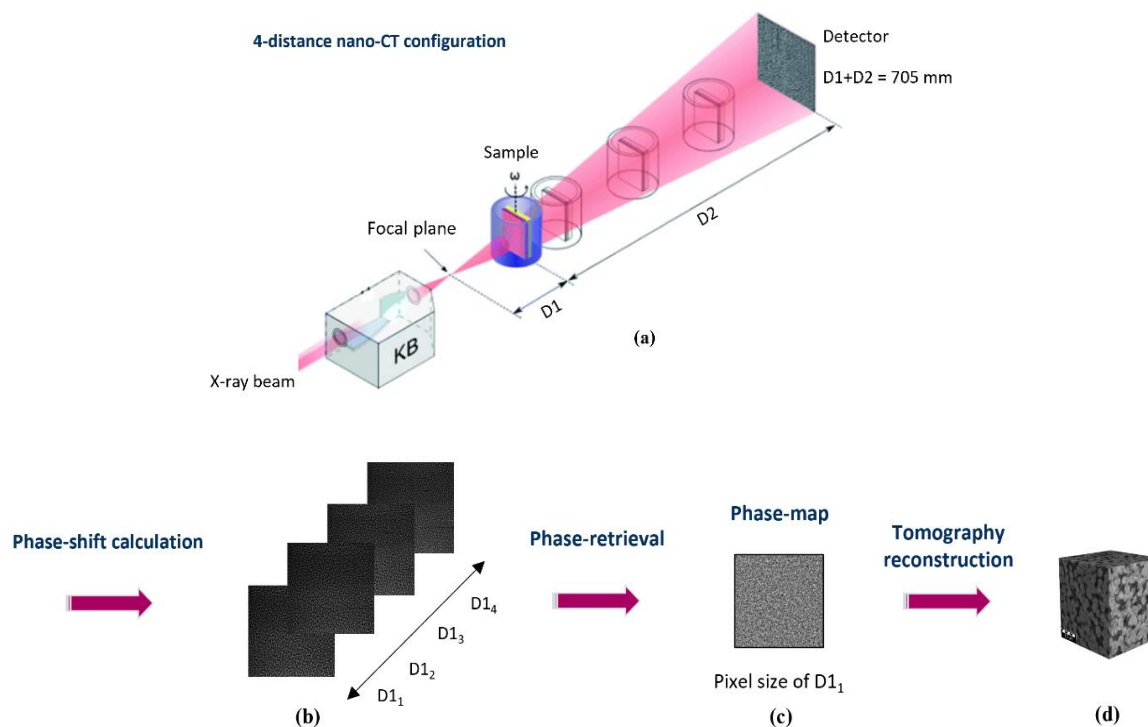


Figure 26. Principle of nano-CT at ID16B beamline of ESRF: (a) sketch of the experimental design [61], (b) radiographs taken from the 4-distance image set and (c) phase map obtained by phase retrieval, which are then used in (d) a tomographic reconstruction.

The first distance, corresponding to the highest magnification would then determine the final pixel size. Complete scans with a number of projections are taken at each distance. However, the acquired images (*radiographs*), say at D_1, D_2, D_3, D_4 are not directly used for tomographic reconstructions. All these images are magnified and aligned in accordance with the first distance image (**Figure 26** (b)), and at each projection angle, this 4-distance image set is used to retrieve the phases, i.e. to reconstruct the phase-shift at each angle, using *phase-retrieval* algorithms to obtain the so-called *phase-maps* (**Figure 26** (c)). The retrieved phase maps are then fed into the tomographic reconstruction software. Subsequent tomographic reconstructions from all the projection angles will finally yield the 3D distribution of the sample (**Figure 26** (d)).

Stages in a holotomography experimentation

The three following stages of alignment, acquisition, and reconstruction make up a typical holotomography experiment:

i. Alignment

The alignment process involves the following two tasks, briefly listed here:

- *Alignment of the optics* to have the desired beam size, energy and intensity at the focal plane.
- *Alignment of the experimental set up*, i.e., aligning the sample stage and detector to reach the targeted resolutions.

ii. Acquisition

- Setting the data acquisition parameters of the tomographic scan, like the number of projections, exposure time, etc.
- Carrying out the holotomography acquisition, recording a series of holograms, following the preceding section.

iii. Reconstruction

The reconstruction process follows different steps: The first one being the *phase-retrieval* calculation using 1-distance set of data (for lower resolution, pixel size = 100 nm) or 4-distance set of data (for higher resolution, pixel size = 25 nm) (**Figure 26 (b)**). The phase maps obtained (**Figure 26 (c)**) are used for the 3D reconstruction (**Figure 26 (d)**). Eventually, *post-processing* can be performed on reconstructed data to remove artifacts.

Here below, the different steps are fully detailed.

- Phase-retrieval

The first step in the reconstruction of the 3D volumes is to retrieve the phase information. While this phase-retrieval inverse problem is intrinsically non-linear, various approaches have been proposed to linearize it (**Figure 26 (c)**) [62].

Two different algorithms for phase retrieval were employed in this work, which are described briefly in the following section.

The first approach is based on the *contrast transfer function* (CTF). The CTF linearizes the intensity by expanding the transmittance function to the first order with respect to the amplitude and phase. This yields a linear relationship that is suitable for weak absorbent materials yielding negligible attenuation and a slowly varying phase shift [63]. The parameters that governed the phase-retrieval in this case were the limits of the lower and higher frequencies of the wiener

filter (lim1 and lim2), along with the decision to choose a recursive algorithm or not. The selection of these parameters is sample and pixel-size dependent.

The second approach is based on the *Paganin's method* [64], [65], derived from the transport of intensity equation (TIE) model. This approach assumes a homogeneous sample where the phase-map is proportional to the absorption-map. This method works well for absorbent samples, with a lower δ/β [66].

More information and a comparison of both these methods can be found in Kostenko *et al.* [67], Langer *et al.* [68], and Yu *et al.* [62].

In the case of alumina samples, the first approach usually outperformed the other method and gave better reconstructions. On the other hand, for the ZnO samples, both with and without alumina inclusions, we observed that the second approach did relatively better, with a δ/β of 59.7, and a recursive algorithm with a number of iterations.

- Tomographic reconstruction

After obtaining a set of phase maps for each angle of the tomography scan (**Figure 26 (c)**), we can reconstruct the 3D volume (**Figure 26 (d)**), of the refractive index using tomographic reconstruction algorithms. Here, we use ESRF's in-built *PyHST2* program, which is based on the *filtered back projection* (FBP) method .

- Ring removal

Subsequently, the reconstructed image stack can be post-processed to remove, if any, defects like ring artifacts.

Rings in tomography imaging are circular artifacts that appear on reconstructed images for a number of reasons. They affect the quality of the images, interfere with the image segmentation procedure and compromise both the qualitative and quantitative analysis aspects of the 3D volumes.

Rings can be caused by different factors depending on the type of experiment and the imaging modality. Sources of artefacts are discussed in Kak *et al.* [69], Michael, G [70] and investigated further in Vidal *et al.* [71].

In a post-mortem experiment set-up, rings are expected to be caused by detector mis-calibration, non-uniform response by detector elements, impurities in the optical path, dusty or

damaged scintillator screens, etc. In an in-situ experiment, in the furnace, additional factors like - thermal drift due to temperature changes during the scan, mechanical vibration of the furnace or the sample, the dirt accumulated in the furnace windows and the insulating material surrounding the sample, etc., need to be weighed in.

Ideally, the *flat-field correction*, wherein a flat image is acquired by removing the object from the field of X-ray and this is then subtracted from the radiographs acquired later to remove undesired signals, should be able to remove these impurities, but, when it does not - these errors enter into the radiographs as lines along the angular direction. These lines then turn into concentric circles in the reconstructed images.

In this thesis, two methods are employed to remove the rings - by *post-processing* or by *correcting the projection data*.

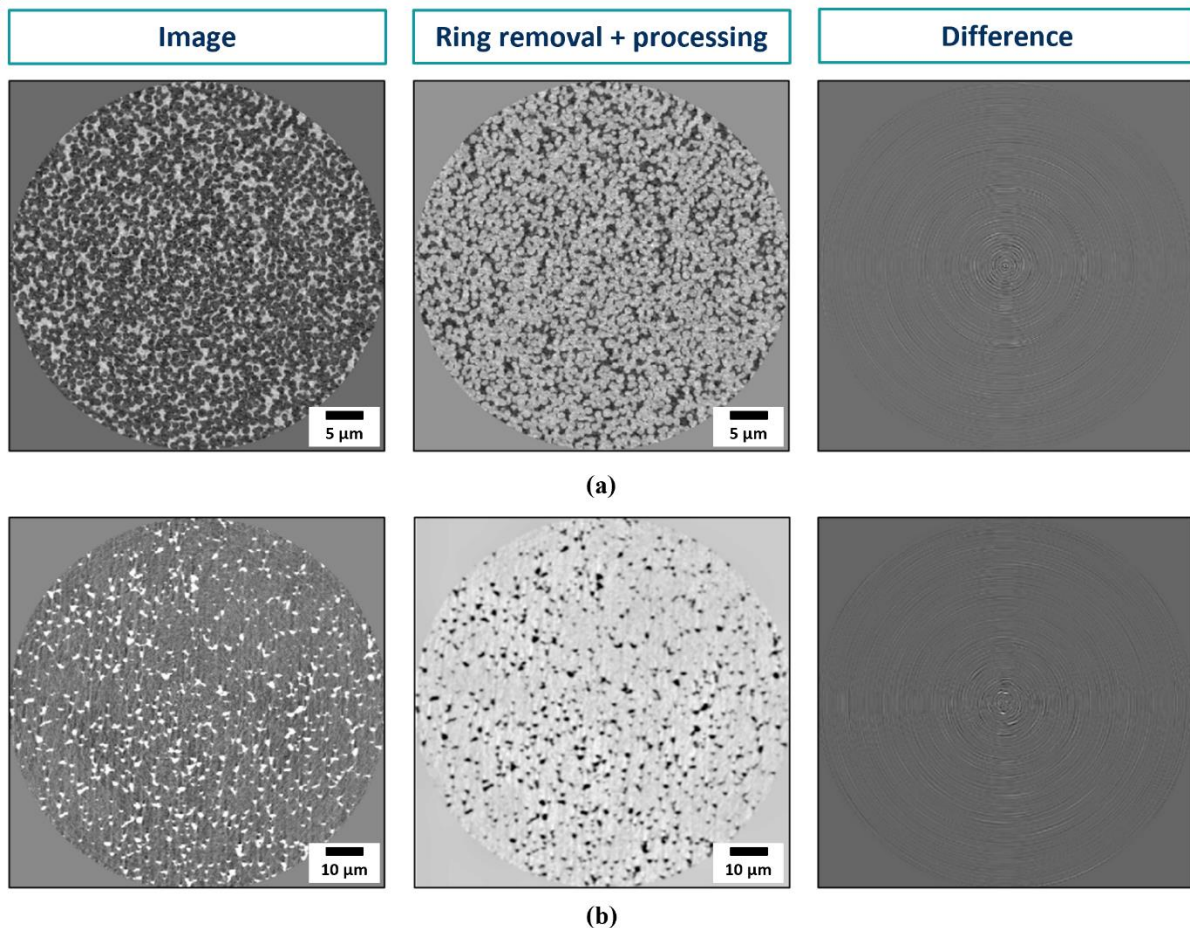


Figure 27. Results of the ring removal operation by post-processing, followed by a qualitative improvement, for the post-mortem experiments, shown here for one of the cross-section slices of (a) Al 1.3µm and (b) Al 0.7µm respectively.

Post-processing methods, following a MATLAB script incorporating the method presented in Lyckegaard *et al.* [72] for micro-CT reconstructions, fared well in the case of alumina samples. It is a trial and error approach that involves tweaking of the necessary parameters to converge toward best results. For instance, parameters like the median size of the ring (width of the largest rings visible i.e., the maximum thickness of the ring to correct - a few passes are necessary for a proper smoothing effect), blur angle (minimum arc length - if the rings seemed to be a perfect circle, the value ranged between 80-120, and if partial, a lesser value sufficed) etc.

Results show that the image can be well-restored without compromising image resolution (**Figure 27**).

In the in-situ experiments, post-processing did not give out the desired result but instead introduced fresh distortions in the image. A better approach was to target the erroneous pixel values in the projection data (radiographs), corrupted due to insufficient flat-field correction. The radiographs were hence subjected to a combination of *Double flat field correction*, *Munch correction* and *Dering correction*.

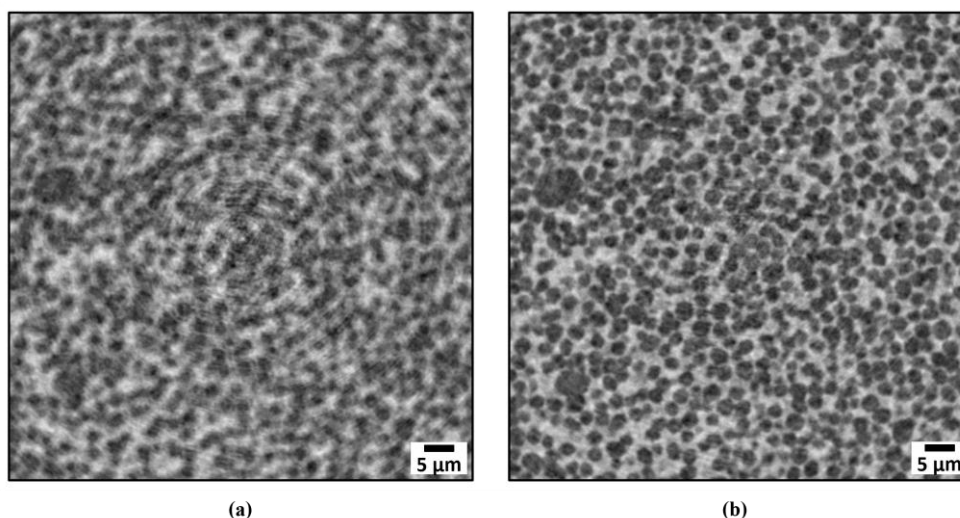


Figure 28. (b) Results of the ring removal operation by correcting the projection data, for the in-situ experiments, shown here for a (a) cropped section of one of the cross-section slices of Al 1.3µm.

In Double flat field correction, to adjust the errors of detector elements, a single radiograph is obtained by averaging all the radiographs. This radiograph is then applied as a flat-field correction to all the radiographs, reducing or removing the artefacts present. Munch correction employs a wavelet transform and a low-pass filter to revise the offset errors of detector elements. The range of these filters was altered on a trial-and-error basis to adjust the ring

correction levels. Dering correction applies a median filter to the average of the radiographs to obtain an estimate of the offset correction image, which is then subtracted from them.

The principle idea underpinning these methods and the associated parameters are detailed in depth elsewhere [66], [73], [74].

This combined approach seemed to enhance the quality of the reconstructed images of the in-situ observations, as observed in the **Figure 28**.

2.2.4 Design and development of the furnace

This section details the design and implementation involved in incorporating a special furnace system into the beamline set-up for our nano-tomography experiments. The furnace is capable of covering the temperature range from room temperature up to 1500°C. It is compact, and has a stable heating zone, ensuing a stable sample temperature throughout the experiments.

The furnace was developed at *CERHEC, Paris* (credits: *D. Girard*) in co-operation with *SIMaP* (credits: *C. Rajon*), and operated at the ID16B beamline of the ESRF.

The motivation for developing this furnace was to overcome the limitations of a furnace (with an MoSi₂ resistor) already available at the lab. It failed to cater to our demands in the initial years of the thesis. The desired temperature could not be reached, especially for long duration, and it had uneven heat distribution, which prevented its integration in the synchrotron beamline.

The new furnace has a platinoid resistor that allows better control and stability of the temperature. The design of the furnace was inspired by Guinebretière *et al.* [75] who have shown that elevated-temperature furnaces with platinoid resistors can be tailored to achieve successful results in specific applications. The furnace also has a cooling system that was modified several times to ensure effective heat dissipation. The furnace, on the whole, operates flawlessly now and has played a big part in the conduction of our experiments.

The following segments describe the special requirements and the technical specifications of the furnace.

Special guidelines to take note of

To ensure the success and safety of the nano-tomography experiment in the beamline, the following guidelines had to be adhered to while developing the furnace:

- The furnace must not alter the room temperature of the beamline, as the optical systems are very sensitive to temperature fluctuations (temperature rise in our case). Even a 0.1°C increase inside the beamline hutch is detrimental and can cause misalignment and defocusing of the beam. So, care must be taken about the furnace meant to be at 1500°C, of course.
- The ability to achieve fast heating and cooling rates is another crucial design parameter.
- The furnace needs to be well-shielded to avoid any radiation emission.
- The furnace should be compact, light-weight, stable, and isolated from other accessories in the beamline.
- Pre-calibration is necessary before starting the experiment, including the aspects of temperature measurement, power supply, coolant system, and sample positioning.
- The cables and tubes for the above components should be long enough to be controlled from outside the hutch.
- Compatibility of the coolant with other ESRF accessories, compliance with the safety regulations, and avoidance of any coolant leakage.

Technical characteristics of the furnace

The high temperature furnace used for the nano-tomography experiments has several characteristics that makes it suitable for the task (**Figure 29**). It can reach up to 1500°C and maintain that temperature for long hours.

The furnace has a hole for the beam to pass through, a hole for the thermocouple to measure the temperature, and another hole so that the sample can be inserted from the bottom. The interior has a woven architecture with a platinum resistor wrapped around coil-like (**Figure 29** (a)). The platinum resistor has high electrical resistance and low thermal expansion, which makes it ideal for high temperature applications. The furnace is insulated with a refractory foam. The resistor is connected to an arm, made of mullite, which is a transitional material that has low thermal conductivity and high mechanical strength. The arm serves as a key element to fix the furnace in place and to control the heat transmission (**Figure 29** (b)).

The outer casing is made of copper (**Figure 29** (c)), has dimensions of 65 mm in height and 154 mm in length. The furnace, including the casing, weighs around 2 kg. The platinum resistor ball has a diameter of 37 mm from the side view.

The furnace also boasts an effective cooling system that consists of passages in the casing for the coolant to enter, flow through and exit (**Figure 29** (d)). The coolant enters through a hole on the top, which then dissects into two branches. Each of these two, splits into four more branches in a perpendicular direction, amounting to 8 passages covering the sides of the furnace simultaneously where most of the heat is generated. The coolant gets hotter as it passes by and then leaves the casing through another hole at the other end of the top part of the casing. The system is designed to provide the coolant in full flow on to the critical parts of the furnace, and to prevent any fluctuations in its outside temperature. The copper casing does not alter or melt because of this effective cooling system, and the furnace remains stable throughout the process.

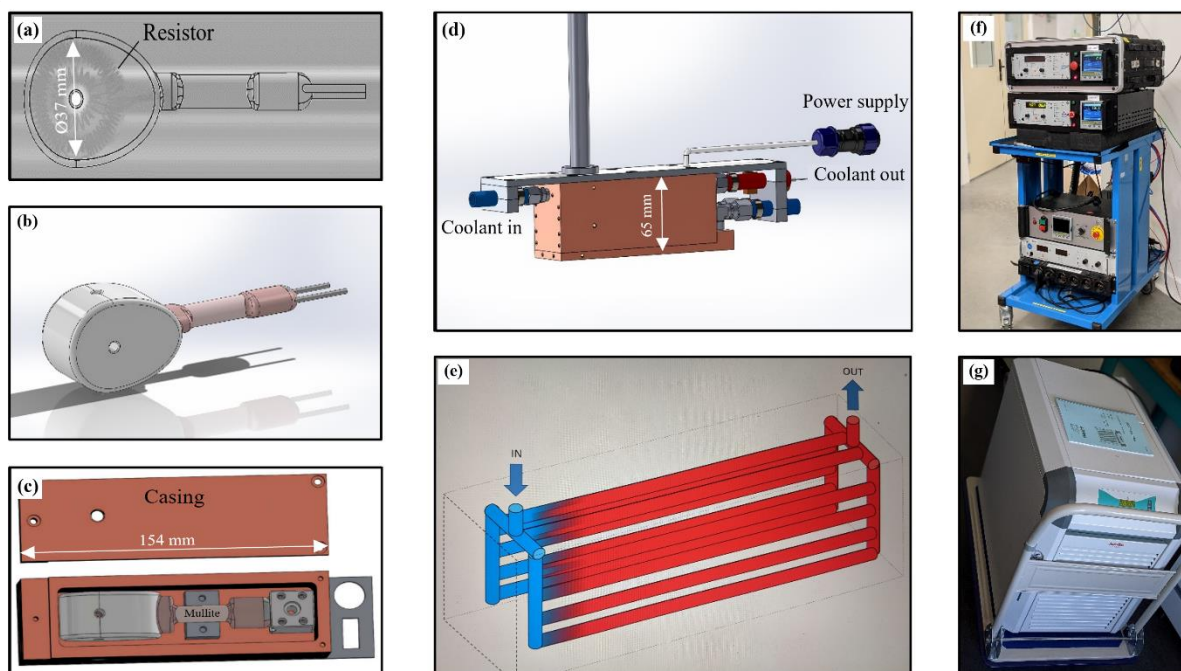


Figure 29. (a) Internal architecture of the furnace showing the coil-like resistor, (b) 3D view of the furnace, (c) furnace enclosed in the copper casing, (d) illustration of the cooling system, (e) passage mechanism of the coolant, (f) power supply indicating the voltage required to meet the temperature criteria, (g) photograph of the cooler used.

The coolant used is ethylene glycol, supplied to a recirculating cooler (from *Julabo GmbH*). The FL1203 model (**Figure 29** (g)) was chosen after trying and testing different models of the FL series, as it had a higher flow rate that matched our estimates. The FL1203 has a flow pressure range of 0.5 to 3 bars, a flow rate up to 40 l/min, a working temperature range of -20 to 40 degrees, and a temperature stability of ± 0.5 degrees.

The temperature of the coolant was set to 16 before supplying it to the furnace, and it was able to maintain an outside temperature of 23 degrees during our experiments, after going through

the cooling system. 23 degrees is exactly the temperature that needs to be at the hutch. The furnace was powered by a DC power supply (*delta electronica*), driven by voltage and controlled from outside the hutch. A voltage of 42.7 V (corresponding to a current of 6.2 amps) was needed to achieve the desired temperature (**Figure 29** (f)). A S-thermocouple was used to measure the temperature in the furnace from the top, and a K-thermocouple was used to measure the wall temperature.

In addition, efforts were put in to automatize the process as much as possible, by integrating, say, a translation arm for the furnace movement, a remotely-operated plate of aluminium to shut the sample outlet when the furnace is out, etc.

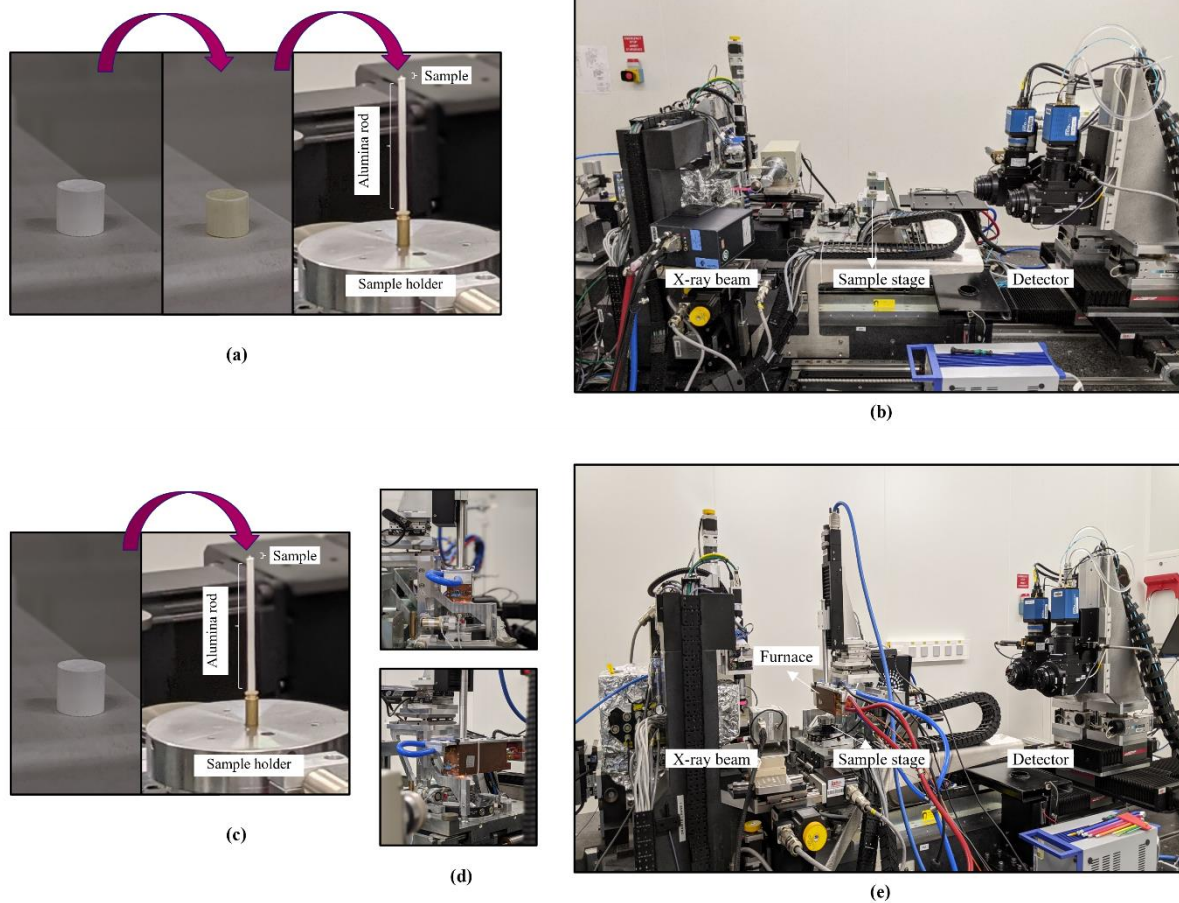


Figure 30. (a) From green compacts to sintered compacts to tiny fragments stuck on an alumina rod, to the (b) process of post-mortem nano-CT experiment. (c) From green compacts to sintered compacts to tiny fragments stuck on an alumina rod, to the (e) process of in-situ nano-CT experiment, with the incorporation of the (d) high temperature compact furnace.

Taking into account all the sub-sections in this chapter so far, for a complete picture of the process outline involved in the post-mortem and in-situ nano-CT experiments, the reader is directed towards the self-explanatory **Figure 30**.

For post-mortem, each projection took 50 ms, so 1-distance imaging lasted ~4 min and the 4-distance scanning lasted up to around ~20 min. For in-situ, some extra room for the furnace movements needs to be considered.

2.3 Image Processing and Segmentation

The success of the analyses of the 3D microstructures relies critically on the extent of the segmentation performed. A good *image segmentation and processing technique* assumes a significant role in material analysis and is a must for the quality and accuracy of the subsequent quantitative analysis workflow.

An accurate segmentation involves dividing an image into regions or *segments* that share similar characteristics, such as color, intensity, or texture. The goal is to separate the objects of interest from the background and from each other. However, it can be challenging in the case of complex microstructure geometries and a comprehensive approach with different segmentation tools and algorithms is necessary.

In this context, the reconstructed 3D samples from nano-CT are considered here and an outline for an effective segmentation was developed. Many different open-source imaging platforms, such as, *ImageJ* [76], *Scikit-image with a Python package in a Jupyter and a Spyder environment* [77]; 3D image processing and modeling software like *GeoDict* [78] and *Avizo* [79] were used for the same.

The following steps describe a general outline of image segmentation and processing for 3D microstructures, which has well been the case in the present study as well:

Pre-processing: The image/ image stack must be initially pre-processed prior to segmentation. This step aims to enhance the image quality and the visual appearance by reducing or correcting image defects like noise and artifacts. Some common pre-processing operations are median filtering, mean filtering, non-local means (NLM) filtering, Fast Fourier transform (FFT) filtering, histogram equalization, etc. These operations can smoothen the image, remove outliers, enhance contrast, adjust brightness, etc.

Thresholding: Once pre-processed, this step converts a grayscale image into a binary image by assigning a pixel value of 0 or 1 based on a threshold value. The threshold value can be determined manually or automatically using methods such as Otsu's method, which maximizes the inter-class variance between the foreground and background pixels.

Watershed transform: To get rid of the grain contacts present after thresholding, the binary images are treated with an advanced marker based tool of ‘Watershed’ with ‘Distance transform’ (**Figure 31**). The output is a set of ‘particles’ assigned to different colored masks, with no particle belonging to a mask of one color being in contact with another particle of the same color. The contacting grains are now separated, as in, the particles touching are now assigned to different colored masks. Watershed is a region growing approach, wherein, starting from user-defined markers, the algorithm treats pixel values as a local topography. The algorithm floods basins from the markers until basins attributed to different markers meet on watershed lines [80]. In this context, an important entity is the distance between the image pixels, calculated using the distance transform [81]. This involves transforming the image intensities to represent the distance from each pixel point to the nearest boundary, with pixels at the center having the largest distances, thus resulting in the formation of basins with their bottom representing a minima. The watershed algorithm is then capable of creating a boundary by finding equidistant lines between these minima, thereby segmenting the regions [81].

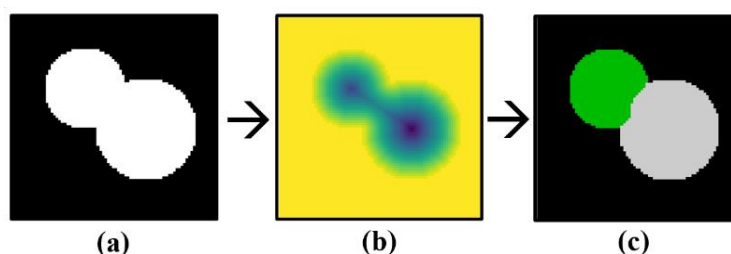


Figure 31. Process involved in a watershed segmentation [81]: (a) representative image with entities to be separated, (b) distance transform of the image, (c) watershed result.

The results obtained are satisfactory but are subjective. We take this notion of the watershed algorithm and further incorporate an improved version of the same offered in GeoDict and Avizo software as well.

For instance, in GeoDict, in the initialisation step of watershed, a ‘minimum grain diameter’ parameter is defined, specifying the minimal size of the grain, thus determining which grains are to be kept and which ones are to be neglected or merged with other grains. This effect of removing small, negligible objects is suitable for denoising ahead of watershed. Further, to fine

tune the watershed performance for complex grain shapes, a probability term called *interface ratio* is defined, setting a condition for two grain fragments to be belonging to the same grain. The ratio compares the interface area of the two touching fragments with the surface area of the fragment with the smaller surface [82]. If the ratio is larger than the percentage of the chosen interface threshold, then the two grain fragments are merged. The parameters for the interface threshold are programmed with a python script.

The contacting entities are thus separated at the end of the watershed process, as in, the particles touching are now assigned to different colored masks (**Figure 32**).

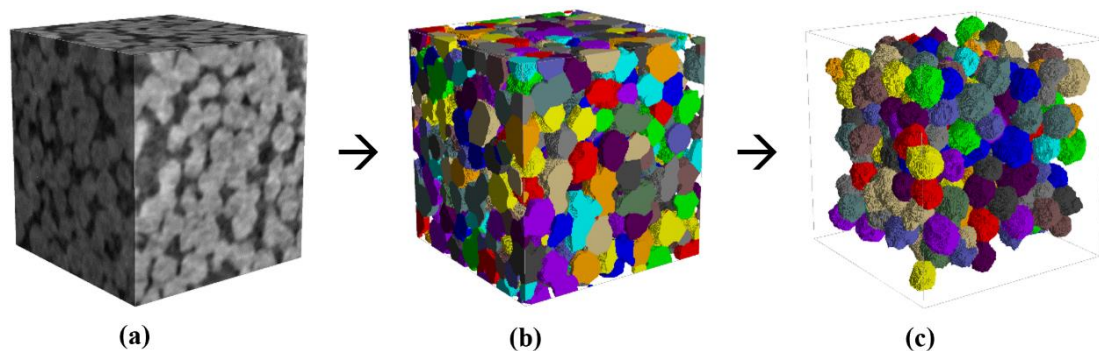


Figure 32. Illustration of outline of the improved watershed segmentation: (a) 3D image stack alumina from our study with entities to be separated, (b) watershed result, (c) structure after boundary grain removal.

However, watershed segmentation can suffer from two main problems: under-segmentation and over-segmentation. Under-segmentation occurs when some regions are merged together due to the lack of clear boundaries or the presence of noise. Over-segmentation occurs when some regions are split into too many small segments due to the high sensitivity of the algorithm to local minima. To overcome these problems, some preprocessing steps or postprocessing techniques can be applied, such as smoothing, filtering, marker-based segmentation, or region merging.

Morphological operations: In some cases, it would also be necessary to post-process the images using morphological operations. : This step aims to refine the segmentation results and correct any errors or inconsistencies. These operations modify the shape and size of the image regions by applying structuring elements. Some common morphological operations are erosion, dilation, opening, closing, etc. These operations can remove small objects, fill holes, smooth boundaries, or separate connected regions.

Furthermore, for all the samples analyzed here, in certain cases, modifications of certain processes are required, say, incorporation of additional processing operations, tweaking of some parameters depending on the complexity etc., but general framework of image segmentation and processing remains similar. The above steps are not fixed or exhaustive in that sense, and the steps vary depending on the type and quality of the image. Some images may require more preprocessing or noise removal than others. Therefore, the parameters of the segmentation algorithm were adjusted and tweaked accordingly.

For example, some images may require additional steps or different parameters to achieve optimal segmentation results. However, the general framework of image segmentation and processing remains similar for most cases.

2.4 Quantitative Analyses and Derived Outcomes

To validate the segmentation result and evaluate the degree of sintering, we performed various quantitative analyses on the segmented images. Different tools meant for imaging and modeling, such as Avizo, GeoDict, and ImageJ plugins, were employed to process and analyze the data.

For Alumina of 1,3 μm , we were able to plot and evaluate various parameters related to grain evolution, such as grain distribution, co-ordination number, diameter and shape changes etc. However, over time, the segmentation algorithm does not succeed in detecting every grain correctly and results in merging of grains in some cases.

For Alumina of 0,7 μm , grain segmentation was not feasible owing to their smaller size. Hence the segmentation and the subsequent analyses have been done from porosity point of view. The above explained watershed technique is applied to the pores in this context to segment pores and then classify the open connected pores and the closed isolated pores.

Net net, image analyses helped us understand pore and particle changes for the alumina powder, and, for powdered mixture, we tracked the flaws caused by the inclusions.

Workflow and analysis of each of the analysis is detailed at appropriate places in the following chapters pertaining to the results.

*This **Chapter 2** narrates, in a way, the journey of obtaining the results presented in the following chapters. It was not so straight-forward, as it involved selecting the appropriate*

ceramic powders, experimenting with X-ray nano-tomography techniques and apt furnace configurations, while overcoming many challenges and failures along the way. It took several months of computational effort to reconstruct the 3D images from the acquired tomography data and then several more months to secure a slot for the next set of synchrotron experiments. The subsequent deciphering of the 3D images involved trying out different imaging software and a thorough literature review for comparisons and validations. The culmination of all these efforts is the qualitative and quantitative analysis of the ceramic microstructures that are discussed in detail in the next four chapters.

CHAPTER-3

POST-MORTEM NANO-TOMOGRAPHY INVESTIGATION

This chapter addresses the first objective of the PhD thesis and presents the results of *post-mortem 3D observations* of sintered alumina samples at their particle length-scale. This chapter has been published as a scientific article, '*3D analysis of ceramic powder sintering by synchrotron X-ray nano-tomography*' in the Journal of the European Ceramic Society (JECS) with the DOI:10.1016/j.jeurceramsoc.2022.12.065. This article is reported here as it has been published, with minor modifications for consistency with the thesis format.

In **Chapter 1**, we set the premise of this thesis and listed out the objectives. The state-of-the-art in this field, the challenges and limitations of existing methods for observing ceramic sintering were discussed. The need for high-resolution imaging techniques that can capture intricate details of the evolution of grains and pores during sintering was stressed upon.

In **Chapter 2**, we described the materials and methods used in this study, including the preparation of alumina powder samples and the sintering process, with a special focus on the recent developments in the nano-analysis beamline of ESRF synchrotron, offering unprecedented imaging capabilities. We explained how this breakthrough could open up new possibilities in material science, allowing us to obtain 3D images of ceramic samples with a spatial resolution as high as 25 nm.

These methods are incorporated here in **Chapter 3** to study the sintering process of ceramic powder samples using synchrotron X-ray nano-tomography. We report on the 3D observations of alumina samples with different initial particle sizes and sintered at different time intervals. A comprehensive 3D characterization of the microstructure of sintered samples with both a qualitative and a quantitative assessment is provided, and key global parameters related to grain and pore evolution during sintering, from a morphological perspective are discussed. It is the first time that images with such a high resolution have been obtained in the context of ceramic sintering. It reveals how synchrotron X-ray nano-tomography can provide valuable insights into the microstructure of ceramic materials, and thereby into the mechanisms and kinetics of sintering.

Abstract

In-depth investigation of the sintering phenomena in ceramic powders remains challenging, with the typical size of the individual particles being around 1 μm or less, i.e., at the resolution limit of X-ray micro-tomography (μCT). This has been dealt with, thanks to the state-of-the-art hard X-ray nano-analysis beamline at the upgraded European Synchrotron Radiation Facility (ESRF). Complete 3D images were obtained for representative ceramic powder systems with a voxel size as low as 25 nm, so as to depict particles and pores with adequate details and follow the entire sintering process. Subsequent quantitative image analyses were used to explore microstructural changes, including the evolution of relevant sintering parameters with respect to the grains and the pores. Notably, a study adopted in this research on the advancement of pore curvatures can be linked to tracking the stages of sintering.

3.1 Introduction

Sintering is undoubtedly the most prominent step in powder processing of ceramics [1], involving the transformation of a powder or a powder compact into a bulk material of controlled density under thermal energy. The complete process is classically divided into three sequential and overlapping stages, characterized by the formation of so-called necks in between the individual particles in the initial stage, considerable densification resulting from the shrinkage of the interconnected pore channels in the intermediate stage, and eventually the creation of isolated closed pores in the final stage, with concomitant grain growth [10], [12].

The experimental studies in the context of powder sintering and the subsequent characterization for a quantitative investigation were largely carried out by classical observation techniques such as optical or scanning electron microscopy (SEM). The micrographs of the traditional SEMs were vital in illustrating various sintering related phenomena, but, from a two-dimensional (2D) perspective with relatively small fields of view. This restricted the assessments of complex sintering parameters, which require rather a three-dimensional (3D) outlook [83]. For instance, 2D images provide insufficient understanding of the complex network of pore morphologies in a microstructure. The 3D interconnected pore channels could appear isolated in 2D sections, giving insufficient or wrong impression on the connectivity and the closure of the pores [84], [85]. This highlights the significance of 3D imaging offered by non-conventional characterization techniques, like X-ray tomography.

In fact, 3D imaging has been proven to be of great value in improving the understanding and modeling of sintering of metallic and glass powders. Various notable works of Lame *et al.* [35], Nöthe *et al.* [37], Olmos *et al.* [86], and Kieback *et al.* [41] have employed X-ray micro-tomography (μ CT) apparatus to compute and follow-up relevant sintering parameters. These works, for instance, have employed a resolution of around 1.5 μm pixel size to detect critical sintering related features in the metallic particles of approximately 50 μm in size. This ratio of the order of 1/20 to 1/40 between the resolution and particle size has been found to be a good trade-off amongst the high resolution required to precisely quantify necks and curvatures and the low resolution required to capture particle agglomeration and rearrangement. The insights offered by the characterization of various such tomography outcomes were also found to better validate the sintering theories, as the ones proposed by Delannay *et al.* [87].

For ceramic powders, the same results cannot be realized as a considerably higher resolution is required to enable particle scale imaging. Indeed, as a result of their small size (around or below 1 μm) and complex architecture, ceramic particles most often form agglomerates. Consequently, prominent X-ray μ CT studies over the last two decades on ceramic samples by Bernard *et al.* [45], Lu *et al.* [88], Xu *et al.* [89] etc. to visualize and quantify microstructural evolutions during sintering have been restricted to the agglomerate level. However, more recently, with the advancement in the X-ray nano-tomography (nano-CT) domain at the synchrotron facilities, microstructural evolutions during sintering at the nano-scale are being investigated, as in Okuma *et al.* [51], paving the way for comprehensive ceramic studies. Particularly remarkable has been the observation of sintering phenomena of glass beads at a sintering temperature of 670°C [5]. Nevertheless, it is worth noting that the analyses of commonly used ceramic powders are more delicate because of the higher temperatures required (around or more than 1500°C). To the best of our knowledge, none of the various types of tomography, be it post-mortem, ex-situ or in-situ - choosing the terminology proposed by Salvo *et al.* [90] - has been attempted at a resolution good enough for particle length-scale observation of ceramic powder sintering at higher temperatures so far.

In this work, we explore the nano-tomography technique presented by the ID16B nano-analysis beamline at the European synchrotron (ESRF). The beamline offers a phase-contrast based holotomography set-up [63], which allows 3D imaging at the nano-scale (~ 25 nm voxel size), with fast scan times and with fields of view that are large enough to constitute representative volume elements [54]. With this high resolution, we were able to investigate two sets of pre-sintered micron-sized alumina powders in a post-mortem context. 3D images obtained at this

resolution were used to investigate densified versions of the alumina powder compacts as well, thus allowing the analysis of intermediate and final stages of sintering. The subsequent quantitative evaluations were utilized to follow the evolution of the morphologies of the grains and the pores and a few associated parameters at different sintering time intervals. The information obtained was further scrutinized by comparing them with classical analytical sintering theories. Furthermore, given that the curvature changes are the foremost phenomena in the sintering process, high resolution 3D renderings were used to plot and analyze curvature maps from a porosity reference framework. These maps are shown to serve as an indicator to track the evolution of sintering stages.

3.2 Materials and Methods

3.2.1 Powder and sample preparation

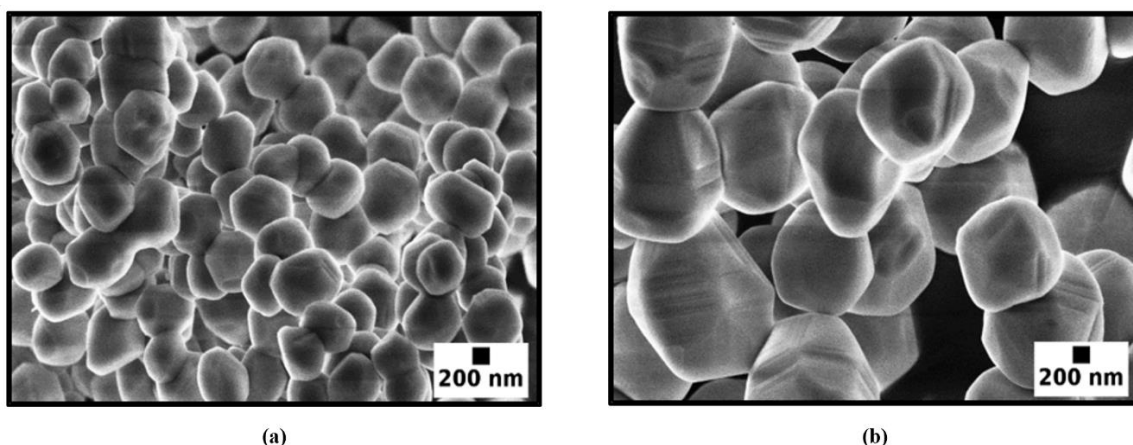


Figure 33. SEM observation of alumina powders with particle sizes of around (a) 0.7 μm and (b) 1.3 μm respectively.

Two sets of alumina powders, AA-07 and AA-1.3, procured from Sumitomo Chemical Co., Ltd. with mean particle sizes of around 0.7 μm and 1.3 μm, respectively, were chosen. These sizes fit the investigation criteria of the synchrotron experiments in terms of the expected resolution (~25 nm). Preliminary SEM evaluations show that these so-called advanced alumina powders, produced by an aluminium alkoxide hydrolysis process [91], [92], have an almost isotropic, polyhedral shape and are fairly non-agglomerated (**Figure 33**).

To assess the sintering advancement of the chosen powders, cylindrical compacts (~8 mm in diameter) obtained by uniaxial pressing of the powders in a die with a stress of ~200MPa, were subjected to sintering experiments in a dilatometry set-up in air. Small quantities of polyvinyl

alcohol were used as a binder for better compaction. Thermal cycles were imposed on to the powder compacts at a rate of 5°C/min with a sintering plateau at 1500°C. A 1-hour isothermal hold at 500°C was carried out to remove the binder prior to sintering. The powder compacts were then sintered individually for different time periods up to 120 hours at 1500°C, and the shrinkage and densification attained were recorded. Bulk densities of the sintered compacts and therewith their relative densities were determined using the conventional ‘Archimedes’ principle, with ethanol as the weighting medium. The compacts were further broken into tiny fragments (about 100 μm in diameter and 1-2 mm in height) for a subsequent investigation using the nano-CT.

3.2.2 Phase-contrast X-ray nano-holotomography

In order to visualize the sintered alumina fragments at the particle scale, X-ray nano-CT experiments were carried out at the ID16B nano-analysis beamline of the ESRF. The beamline is equipped with a set of Kirkpatrick-Baez (KB) mirror systems. These mirrors focus the incoming parallel X-ray beam onto a small beam size of 50*50 nm², which acts as a secondary source [54]. The subsequent conic beam advancement results in a geometrical magnification. An energy of 29.2 KeV was used for the experimentations.

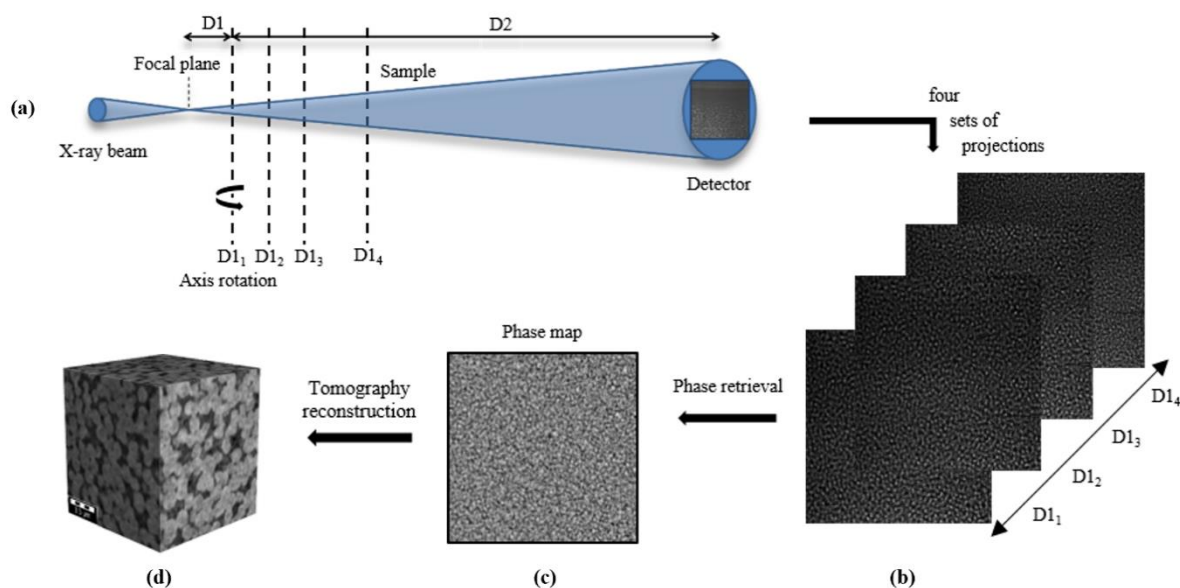


Figure 34. Principle of nano-CT at ID16B beamline of ESRF: (a) sketch of the experimental set-up, (b) radiographs recorded from the 4-distance image set and (c) phase map obtained by phase retrieval, which are then used in (d) a tomographic reconstruction.

With the holotomography system, propagation based phase-contrast imaging was performed by placing and moving the sample (at distance D_1) in the conic beam space at 4 different distances relative to the focal plane. For each of the 4 sample-to-focus distances, 3203 projections were recorded over a 360° rotation using a scintillator screen (LSO 17m) and a CMOS detector system (pco.edge 5.5) at a fixed distance $D_1 + D_2$ from the focal spot (**Figure 34** (a)) [61], [63], [93].

The recorded images at $D_{1_1} = 29$ mm, $D_{1_2} = 30$ mm, $D_{1_3} = 34$ mm and $D_{1_4} = 44$ mm were aligned and magnified according to the first distance image (**Figure 34** (b)), resulting in a pixel size of 25 nm and a field of view of $64*64*54 \mu\text{m}^3$. The exposure time for each projection was optimized to 50 ms, leading to an acquisition time of ~ 4 min for 1-distance imaging. The phase shifts undergone by the sample were captured from this 4-distance image set by means of iterative phase retrieval algorithms to obtain the so-called phase maps (**Figure 34** (c)). The filtered 2D phase maps were then fed into the in-house built ESRF PyHST2 software package [94] to reconstruct and render the 3D distribution of the sample (**Figure 34** (d)).

3.2.3 Image treatment and analyses

Regions of interest (ROIs) of $1000*1000*1000$ voxels were extracted from the reconstructed 3D image stacks. Ring artefacts present were removed with a MATLAB algorithm based on image filtering [72]. A trial-and-error approach was used to find the appropriate parameters. The ROIs were then pre-processed with filters such as fast Fourier transform filter (cut-off frequency of 5%) to remove high-frequency noise, non-local means filter (strength of 0.5) to reduce left-over noise while keeping the edges sharp etc., in image processing software ImageJ and GeoDict [76], [78]. This was followed by the application of automatic thresholding methodologies (OTSU's method) in order to further integrate the segmented 3D renderings in a quantitative analysis set-up. However, segmentation of individual features, say, the separation of individual sintered grains, was challenging, especially for image stacks above 75-80% density. Parameters requiring only effective pre-processing and global thresholding operations for their evaluation were hence chosen.

Grain volume fraction measurement

Volume fractions of the grains were first determined from the ROIs with the ImageJ software [76], to compare with the relative density estimation from the Archimedes approach.

Grain size and pore size estimation

Next, granulometric analysis in the GeoDict image processing platform was employed to estimate the size of the evolving grains [78]. The algorithm in the GrainFind module of GeoDict first converts the thresholded 3D image stacks into distance maps by Euclidean distance transform (EDT) and then evaluates the diameter of the grains by fitting pre-defined spheres into the grain space. A detailed description of the algorithm and its implementation can be found in [95]. Similarly, pore size distributions of the 3D image stacks were carried out by granulometric characterization in the pore space using the PoroDict module of GeoDict [78] [96].

Pore connectivity and pore throat characterization

In order to assess the connectivity in the pore network and their transition into closed porosity, parameters such as pore volume, percentages of open porosity, and percentages of closed porosity were measured using the Analysis_3D plugin in ImageJ [76] [97]. Furthermore, a porosimetric investigation was carried out in the PoroDict module of GeoDict [78] [96]. In contrast to granulometry, here, pre-defined spheres that are fitted into the pore structure are made to pass through from the side of the intrusion to the other side such that it encompasses the entire pore channel. With this, the size of the small pore channels or throats connecting the large pore channels are determined, while needless to say, closed pores do not contribute to the pore throat analyses.

Interface curvature analysis

To track the evolution of pore-solid interface curvature, simplified henceforth as pore curvature, the tools, ‘Shape index’ and ‘Curvedness’ proposed by Koenderink *et al.* [98] for graphical representation of 3D shapes were adopted. In contrast to the classical curvature measures like the Gaussian and the mean curvatures, these shape indicators capture the nuances in the variations of local shapes [99]. The significance of these parameters has been emphasized notably by Shahani *et al.* [100]. They are independent of each other, with the shape index estimating the local shape profile and the curvedness measuring the amount of curvature of the shape. The significance of these indicators will be further explained in **section 3.3.8**. With k_1 and k_2 as the principal curvatures, the shape index S and curvedness C are defined as follows:

$$S = \frac{2}{\pi} \arctan \left(\frac{k_1 + k_2}{k_1 - k_2} \right) \quad (9)$$

$$C = \sqrt{\frac{k_1^2 + k_2^2}{2}} \quad (10)$$

The shape index in Equation 9 can have values in the range from -1 to +1, differentiating convexities from concavities. The curvedness instead, in Equation 10, is a positive value, with 0 indicating a planar surface, quantifying the amount of deviation from a flat plane. Taking these indicators into consideration, pore surfaces of the 3D image stacks were first generated in Avizo software package [79]. Principal curvature values were then computed from the generated surfaces. Using these values, the shape indicators were subsequently calculated in a Python environment, to be further applied to plot curvature maps, i.e., 2D density histogram plots in the (S,C) plane.

3.3 Results

3.3.1 Global assessment

Detailed microstructural changes undergone by the sintered materials were revealed, thanks to the high resolution and the large field of view resulting from the multiple distance phase retrieval.

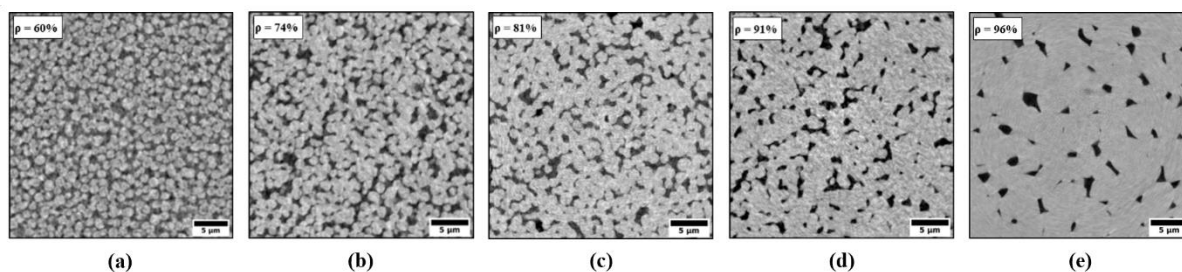


Figure 35. One of the cross-section slices of the 3D reconstructed alumina samples of 1.3 μm (a), sintered at 1500°C and observed post-mortem after (b) 1 hour, (c) 10 hours, (d) 30 hours and (e) 120 hours respectively. The relative density values ‘ρ’ are mentioned.

At a global level, many sintering phenomena such as inter-particle neck growth, densification, grain growth, pore rounding, etc. that are stated in the traditional sintering theories at different stages of sintering [1], [10], [101] are clearly observed in the two alumina samples. **Figure 35** (a) shows one of the cross-section slices taken from the middle of the image stack (1000*1000*1000 voxels) of the 3D reconstructed alumina of 1.3 μm average particle size (henceforth referred to as ‘Al 1.3 μm’), sintered at 1500°C with an original relative density of around 60%. Over time (**Figure 35** (b) (c) (d)), we see developments in this original ‘green’

sample, such as the growth of inter-particle necks, particle center-to-center shrinkage and a considerable densification, with the Archimedes relative density ' ρ ' reaching 74%, 81%, 91% and 96% after 1 hour, 10 hours, 30 hours and 120 hours respectively. The sintered samples thus appear to span the intermediate (~ 70 to $\sim 90\%$ of density) and the final stage of sintering (above $\sim 90\%$ density).

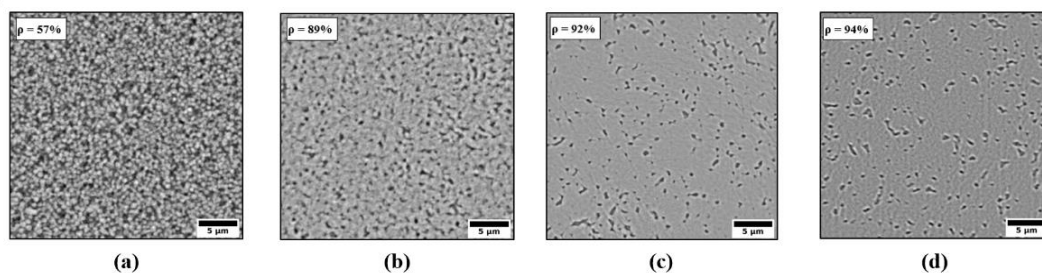


Figure 36. One of the cross-section slices of the 3D reconstructed alumina samples of $0.7 \mu\text{m}$ (a), sintered at 1500°C and observed post-mortem after (b) 30 min, (c) 1 hour and (d) 10 hours respectively. The relative density values ' ρ ' are mentioned on top-left.

Figure 36 shows the sintering progression at 1500°C of the relatively smaller alumina powder with $0.7 \mu\text{m}$ average size ('Al $0.7\mu\text{m}$ '). Global evaluations suggest that the sintering advances much faster in this case, with grains increasing in size, decreasing in number and the interconnected pores turning isolated towards the end, as in **Figure 36** (d). The relative densities were measured to be 89%, 92% and 94% after just 30 min, 1 hour and 10 hours respectively, indicating the final stages of sintering.

3.3.2 Quantitative insights

Classical parameters with regard to the evolution of the grains and the pores corresponding to all the three stages, which are extensively used in the sintering literature, were measured from the 3D data, together with the introduction of some novel parameters.

3.3.3 Density – Grain volume fraction correlation

At each time period, volume fractions of grains extracted from the 3D images, when plotted against the experimentally measured relative density values (**Figure 37**), show an excellent fit for most of the points for both the alumina samples. This in turn proves the effectiveness of the resolution attained, the representativeness of the ROIs and the subsequent image processing. The fit especially suggests that the samples possess a uniform green density. The agreement

between the values at different time periods also provokes interchangeable usage of the terms ‘grain volume fraction’ and ‘relative density’ further in this work.

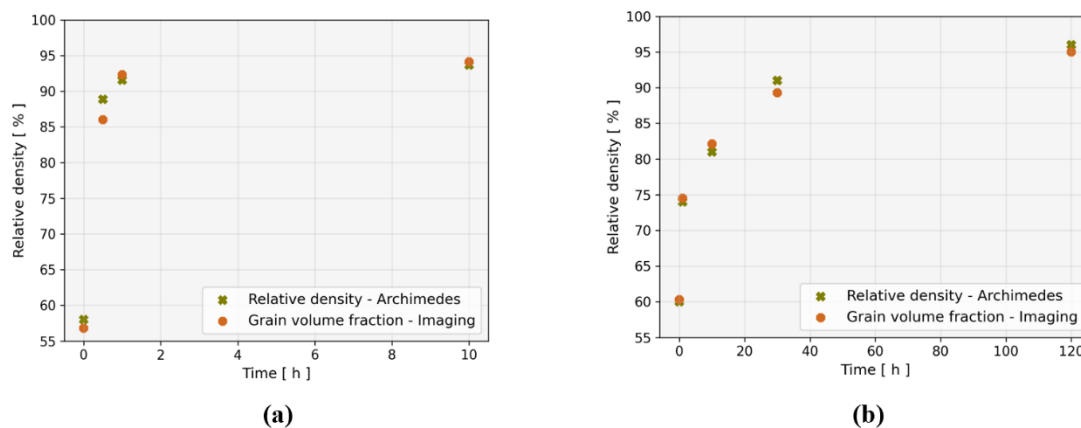


Figure 37. Correlation between the density of the sintered compact measured by the Archimedes approach and the grain volume fraction obtained by image analysis of the tomographic data for (a) Al 0.7µm and (b) Al 1.3µm, respectively.

3.3.4 Grain size progression

Advancements in tomography techniques have led to expressing the grain growth phenomenon occurring during sintering in terms of 3D grain size distribution, replacing the earlier quantitative assessments through 2D micrographs and other stereological methods [102], [103]. Here, the grain size deduction is carried out by granulometry measurements, as described in the previous **section 3.2.3**. **Figure 38** (a) and (b) show a fairly narrow original grain size distribution, with a geometrical deviation of 1.17 and 1.2 for Al 0.7µm and Al 1.3µm respectively. De-agglomerated micron and submicron sized powders with uniform narrow size distributions are proven to improve the sinterability [104] [105] and thereby the densification of the ceramic products to more than 90%, which is very well the case in **Figure 38** (a) (b) as well. Further, the curves for both the samples follow the established fact that the growth of the grains is limited in the early stages of sintering and speeds up as sintering progresses, especially after attaining over, say, 80% of the relative density.

Also to be noted is that these distributions do not show a distinct bimodal shape, thus indicating a pattern of normal grain growth for both the samples [12]. Average grain sizes were calculated from each of these distributions and their conformity with the scaling law proposed by Herring [106] was examined. In accordance with the analysis by Rahaman [12], this law correlates the sintering time period required to reach a given particle size, for two powders with similar

shapes but different sizes (with say, radii a_1 and a_2 , where $a_2 = \lambda a_1$), sintered under the same experimental conditions. The required sintering times t_2 and t_1 , in this case, the time t_2 required by Al 1.3 μm to produce a geometrically similar change as exhibited by Al 0.7 μm in time t_1 , are then interrelated as $t_2 = \lambda^\alpha t_1$. Here, with $\lambda = \sim 2$, α takes a value of around 3.5, which falls in the acceptable range of values found in the sintering literature. As per Rahaman [12], the exponent is 4 for surface diffusion and grain boundary mechanisms and 3 for lattice diffusion.

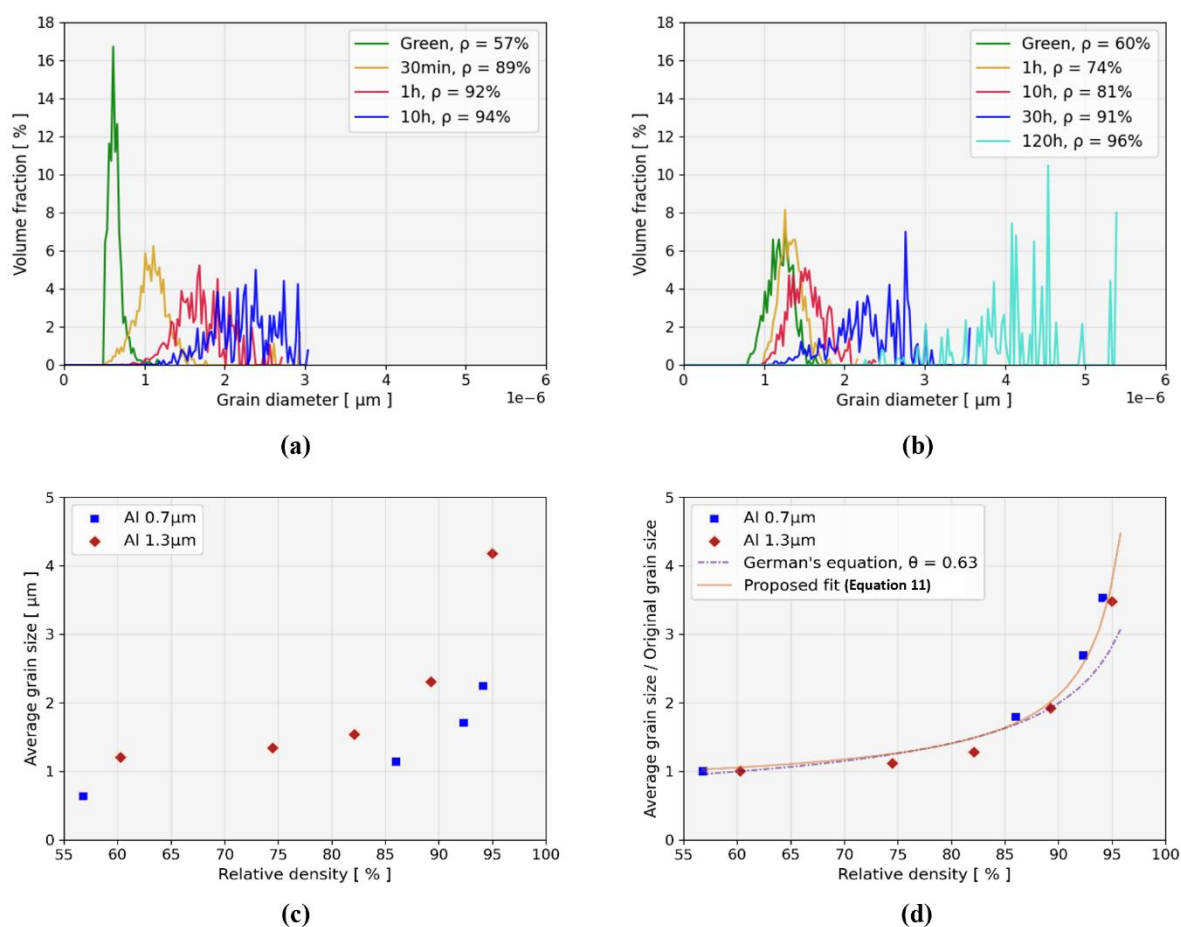


Figure 38. Evolution of grain size distribution for the two alumina samples, (a) Al 0.7 μm and (b) Al 1.3 μm , respectively; (c) comparison of average grain size versus density; and (d) average grain size over original grain size versus density for both these samples, along with the corresponding curve fit according to German's equation [107] and the proposed fit.

Another way of evaluating the grain growth involves plotting the evolution of the average grain size as a function of the relative density attained [107]. In fact, average grain size is considered to be the only basic microstructural descriptor necessary to evaluate the microstructural evolution in many analytical estimations. From the distributions in **Figure 38** (a) (b), the

average grain size points are thus extracted and plotted in **Figure 38** (c). Also, the average grain size points for the two samples are divided by their original grain size and plotted against the density values as in **Figure 38** (d). These points are then compared with the equation proposed by German in [108], [109] for grain size, $G = \frac{G_0 \theta}{\sqrt{1-f}}$, where G_0 is the initial grain size, θ is a constant with a value of 0.6, and f is the grain volume fraction. Trying different values of θ , particularly a value of 0.63 for both our samples, shows a satisfactory match, with goodness-of-fit, $R^2 = \sim 0.8$. This value of θ falls in the range of 0.41 and 0.72, as compiled in the recently conducted studies by Paredes *et al.* [110] for various samples of alumina, with different sizes, sintered at different temperatures. However, an empirical fit below (Equation 11), in line with German's equation, appears to show a better agreement. The proposed expression has an $R^2 = \sim 0.96$, with two constants, $a = \sim 0.5$ and $b = \sim 0.4$ respectively.

$$\frac{G}{G_0} = a \exp\left(\frac{b}{\sqrt{1-f}}\right) \quad (11)$$

3.3.5 Pore size measurements

During sintering, in addition to densification and the corresponding grain size evolution, changes in the pore space occur concurrently. This is evidenced by the decrease in total porosity over the sintering stages. In fact, the pore features play a key role in the physical and mechanical properties of the final sintered product. Quantification of sintering would then be best realized not only by density determinations but also by a thorough understanding of the morphological evolution of porosity in terms of pore size distribution and other associated parameters [111]. These are realized by way of granulometric analysis here, while, over the years, methods like nitrogen adsorption and mercury intrusion with commercial porosimeters were made use of [102], [112].

Unlike in the grain size distributions in **Figure 38** (a) (b), the pore size distribution curves rather appear to be restricted between more or less the same range of values (**Figure 39** (a) (b)). Interestingly, a slight shift to the right is observed in the final curves for both the samples. The average pore size values from each of the distributions were then calculated and plotted against the relative density (**Figure 39** (c)). A slight decrease in the values initially followed by an increase was observed in the case of Al 1.3 μm , whereas for Al 0.7 μm , there was limited variation except for the increase in the values towards the end, above 90% density, consistent with the shift observed in **Figure 39** (a) (b). This increase in the average pore size at the end of sintering, as opposed to a drop as in classical theory, could be attributed to coincident grain

growth, which leads to pore coalescence. The initiation of this phenomenon seems to be reflected in the sets of images in **Figure 36**, especially in **Figure 36 (d)**. Further, this variation could be understood by a normalization as in **Figure 39 (d)**, which gathers all the points for both the samples on one master curve.

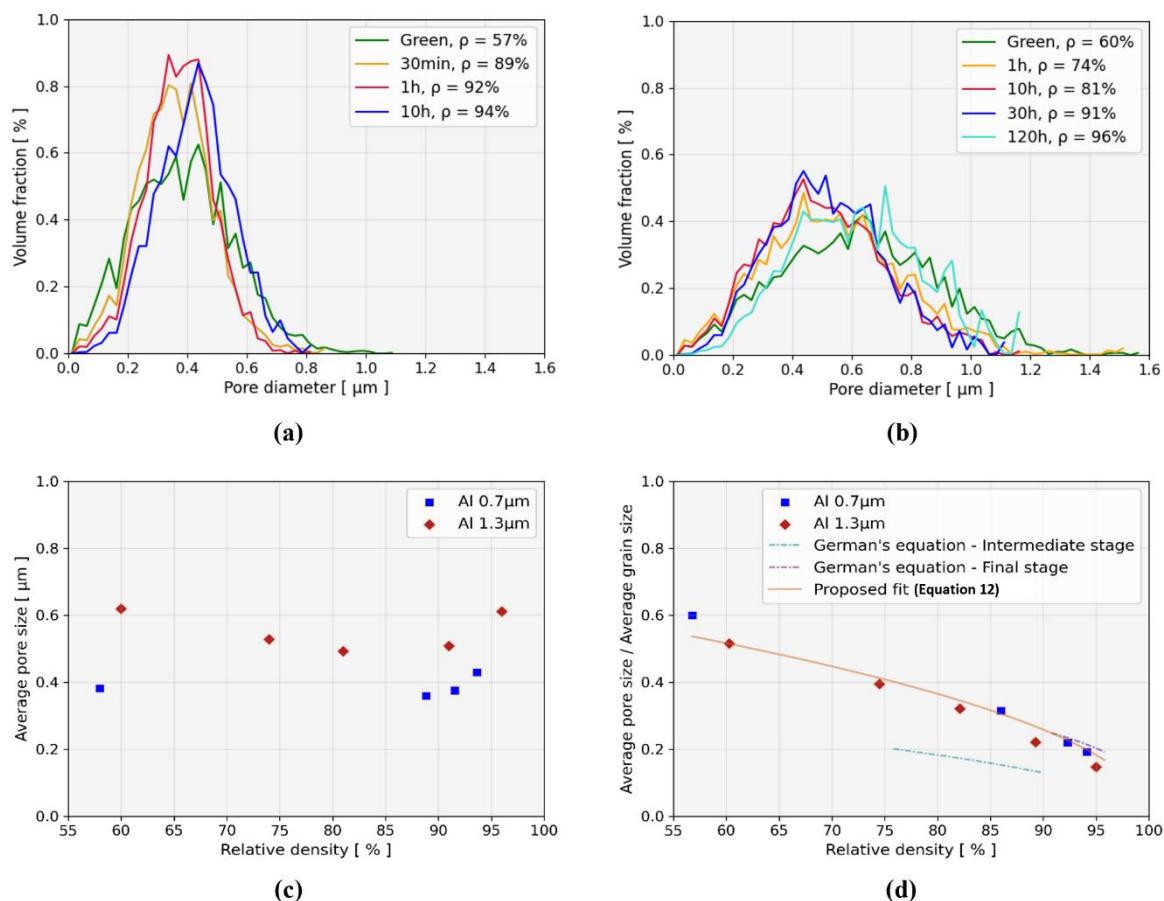


Figure 39. Evolution of pore size distribution for the two alumina samples, (a) Al 0.7µm and (b) Al 1.3µm, respectively; (c) comparison of average pore size versus density; and (d) average pore size over average grain size versus density for both these samples, along with the corresponding curve fit according to German's equation [107] and the proposed fit.

Taking analytical models into consideration, porosity advancement in the intermediate stage and the final stage of sintering proposed by German [108] follows, $p = G \left(\frac{\varepsilon}{6}\right)^{1/2}$ and $p = G \left(\frac{\varepsilon}{6}\right)^{1/3}$ respectively, with a link between pore size p , pore volume fraction ε and grain size G . These analytical relations, particularly the one for intermediate stage, do not yield a good fit when compared to the values obtained in **Figure 39 (c)**. For instance, initial pore size in **Figure 39 (c)** for Al 1.3µm reads 0.61 µm, whereas the porosity relation rather gives 0.3 µm

instead. In order to assess this misfit, a packing of spheres with a similar grain size distribution was considered in a discrete element method (DEM) framework, as in Paredes *et al.* [110]. The packing was rendered in 3D and fed into the granulometry algorithm in GeoDict. This exercise yielded an initial average pore size value of $\sim 0.5 \mu\text{m}$, closer to the initial experimental value of $0.61 \mu\text{m}$. A probable reason for the misfit could be the assumption related to geometry made in classical theories of the intermediate sintering stage. German [108] assumed grains to have the shape of a regular tetrakaidekahedron with open pore channels residing along the grain edges, as have Coble *et al.* [113], [114], Beere [115], Johnson [19] and Yan *et al.* [105]. Eudier [116] and Svoboda *et al.* [117] criticized and disapproved these models in their respective works as these assumptions were not substantiated by enough experimental justifications. Also, in addition to simple theoretical models having a limitation in characterizing the complicated porosity behavior, unlike porosity, the definition of pore size is not so straightforward, much less its way of measurement [118].

However, a modification to the analytical expression above was found to give a rather good fit.

$$p = G \left(\frac{\varepsilon}{1.5} \right)^{1/2} \quad (12)$$

Interestingly enough, it holds true for all the stages of sintering for both the samples (**Figure 39 (d)**).

3.3.6 Pore connectivity and closure

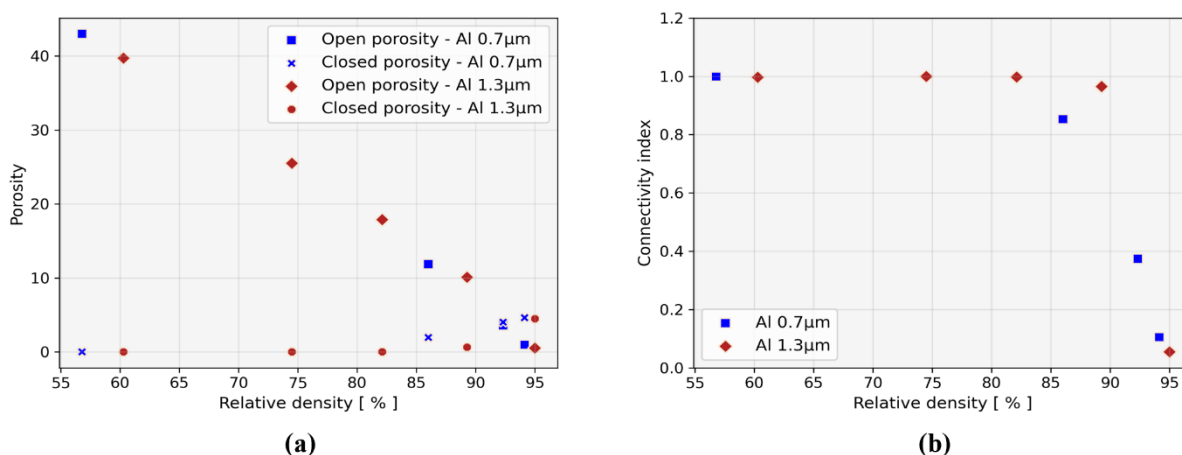


Figure 40. Evolution of (a) open and closed porosities and (b) connectivity index values versus density for the two alumina samples, Al $0.7 \mu\text{m}$ and Al $1.3 \mu\text{m}$, respectively.

As sintering proceeds, towards the end of the intermediate stage, open porosity gets progressively converted into closed porosity [12]. According to the observations by Coleman *et al.* [119], there exists a critical minimum grain volume fraction when the networks of

interlinked, open porosity collapse to form closed, isolated pores. To track this transition, open and closed porosity values were plotted against the relative density in **Figure 40** (a) for both the alumina samples.

The open porosity values decrease throughout for both, meaning the pore channels transform continuously into newer pore networks of lower connectivity. The closed porosity values, on the other hand, remain largely unchanged at 0 until about 85% density for Al 0.7 μm and about 90% for Al 1.3 μm , after which the values rise up. The plot thus gives an idea of the transition, while making it clear that the pores get fully closed at ~94-95% density for both the samples, which is the value most often reported in the literature. The fact that there is no aberration in the trajectory of the values is also another indication of the homogeneity in the microstructure and the absence of large agglomeration [109].

Another indicator for pore closure, called connectivity index (CI) is proposed here. It is essentially the ratio of the largest pore volume over the total pore volume. The concept of CI, presented in Babin *et al.* [80], was further shown by Burr *et al.* [120] to be better suited for X-ray tomography analysis than the conventional closed porosity ratio to predict the close-off density. The advantages and drawbacks of both these methods are properly discussed in [99] and [80]. Accurate determination of pore closure requires high-resolution images, which is incompatible with large fields of view. Consequently, pores that are large with respect to the sample size could appear artificially as open porosity (intersecting the boundary of volume of interest). Closed porosity ratio is thus a biased measure with a smooth variation at pore closure. The connectivity index, meanwhile, is far less sensitive to the sample size and presents an abrupt variation at the closure. The latter is chosen here and as shown in **Figure 40** (b), the connectivity index is equal to 1 when the porosity is totally open, while it is 0 when all the pores are closed. In particular, a clear drop in the index is observed at a density between 80% and 85% for Al 0.7 μm and slightly below 90% for Al 1.3 μm , indicating a switch from open porosity to closed porosity. Additionally, consistent with **Figure 40** (a), the pores appear to be totally closed at ~95% density.

3.3.7 Pore throat characterization

As an additional analysis on the connectivity of the pores, a porosimetric investigation, outlined in **section 3.2.3**, was performed to determine pore throats. The two samples exhibit similar patterns, when the average pore throat size is plotted against density (**Figure 41** (a)). The values show a decrease throughout except a sudden increase in the end. This indicates that, at around

that density, when the pores tend to close-off, most of the smaller pore throats get closed in the process, while the larger ones remain and would get closed eventually afterwards. Taking the changing grain size into consideration, as in **Figure 39** (d), the points show the scaling effect and follow a master curve for both the samples in **Figure 41** (b). However, above a relative density of 92%, the normalized pore throat size shows an increase while the normalized pore size does not.

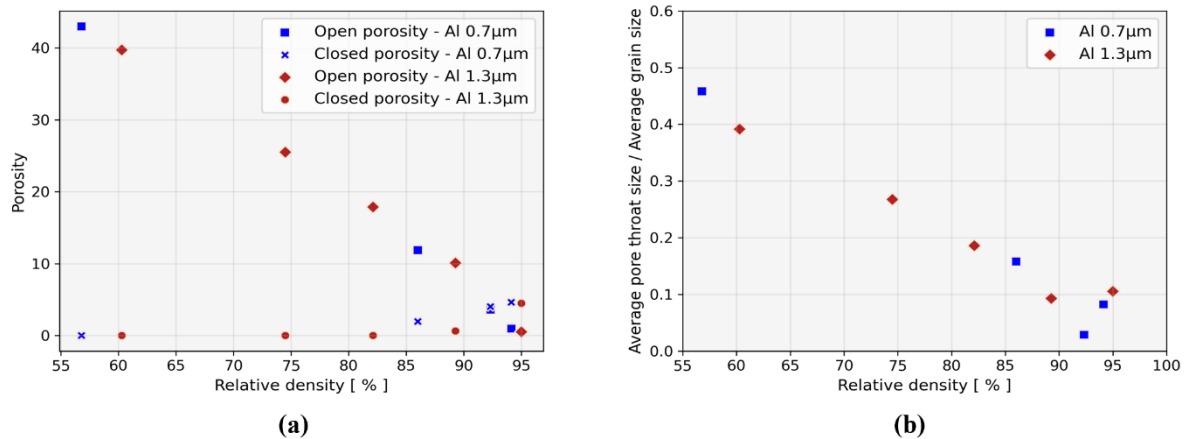


Figure 41. (a) Comparison of average pore throat size and (b) average pore throat size over average grain size versus density for the two alumina samples, Al 0.7µm and Al 1.3µm, respectively.

3.3.8 Curvature maps

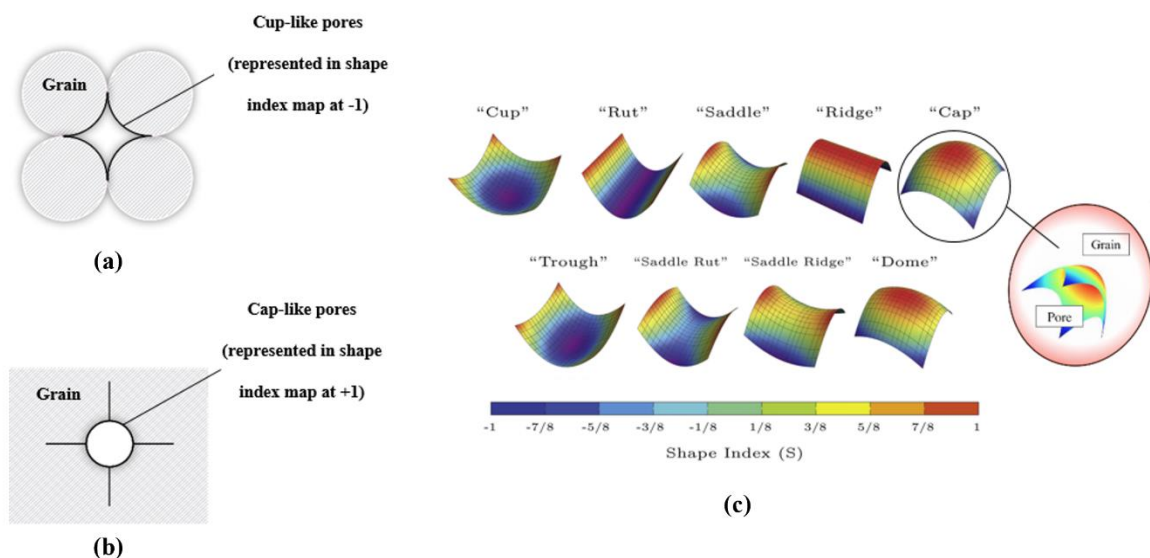


Figure 42. Representation of pore evolution during the sintering process from (a) the initial cup-like pores to (b) the final cap-like pores. (c) Shape index map showing local shapes, adapted from Shahani *et al.* [100] and Burr *et al.* [99].

As illustrated in **Figure 42** (a), particles in the initial stage of sintering have tiny necks between them, with the pores mainly exhibiting a curvature opposite to the curvature of the particles. The process of sintering leads to an intensification in the neck growth phenomenon. This eventually tends to create isolated spherical pores in the final stage with an opposite curvature as against their initial curvature, as in **Figure 42** (b). We expect to visualize and capture this ‘concave-to-convex’ transformation in the pore curvature in the course of sintering [121]. In this regard, the shape indicators, ‘Shape index’ and ‘Curvedness’, defined in Equations 9 and 10, are adopted. These shape indicators have been extensively used in the medical community [122]. Some adaptations were found in metallurgical applications as well [123]. More recently, Burr *et al.* [99] used these indicators to explore snow metamorphism.

The shape index map in **Figure 42** (c), adapted from Shahani *et al.* [100] and Burr *et al.* [99], shows local shapes represented in a color scale and categorized into nine different shapes. The shape indices thus distinguish the shapes in the neighboring surface of a point. Cup-like concave shapes would have a shape index of -1, saddle-like cylindrical shapes equal to 0 and cap-like convex shapes +1.

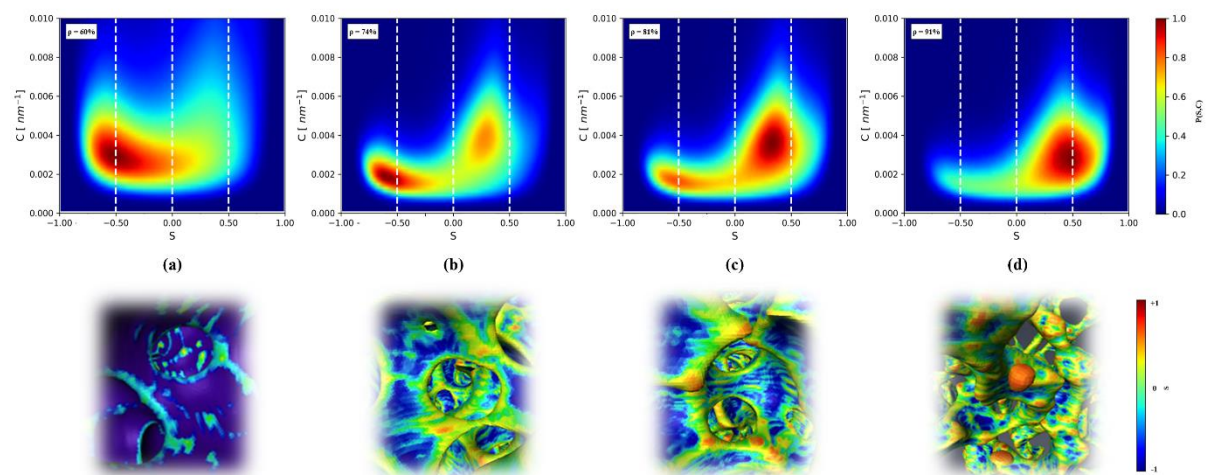


Figure 43. Pore curvature maps for 3D reconstructed alumina Al 1.3 μm (in **Figure 35**) at (a) the initial stage and after sintering at 1500 $^{\circ}\text{C}$ and observing post-mortem at (b) 1 hour, (c) 10 hours and (d) 30 hours respectively, along with snapshots of cropped sections of the 3D rendering of the pore network.

Following the generation of pore surfaces in Avizo software and the calculation of shape indicators, these were then represented as curvature maps in the form of 2D histograms. For the 3D renderings of the image stacks of Al 1.3 μm in **Figure 35**, the curvature maps show an evolution, as in **Figure 43**. These histograms are scaled with a normalized probability density $P(S,C)$ ranging from 0 in blue to 1 in red. In other words, regions in the map with $P(S,C) = 1$

represent the local surfaces with the highest occurrences of the corresponding shape index and curvedness values.

With reference to the shape index map in **Figure 42** (c), the original pore network of Al 1.3 μm exhibits a variety of shapes in **Figure 43** (a), spanning from trough to saddle-like shapes. Eventually, with increase in time, after 30 hours of sintering in **Figure 43** (d), the maximum density point P shifts to the right towards dome-like shapes, indicating that the pores are now on the verge of pinching off from the connected pore channels to become isolated.

Interestingly, somewhere between relative densities of 74% and 81%, there is a clear shift in the maximum density points (**Figure 43** (b) (c)).

Adjacent to each of these maps, snapshots of 3D rendering of the pore network corresponding to that particular stage are shown for better visual comprehension. These renderings display only the pore phase, with the ceramic particles appearing as void. The circular contours in the snapshots could be related to the necks between particles. Evolution of the pore curvature is clearly observed with the beginning of the development of isolated closed pores towards the end, as reflected on the shape index map.

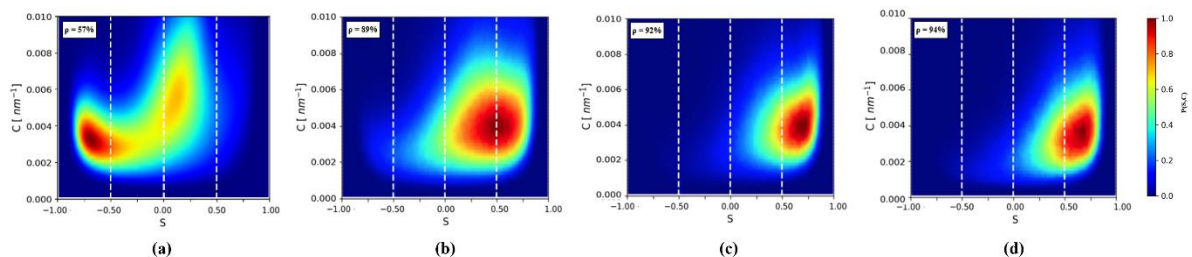


Figure 44. Pore curvature maps for 3D reconstructed Al 0.7 μm (in **Figure 36**) at (a) the initial stage and after sintering at 1500 $^{\circ}\text{C}$ and observing post-mortem at (b) 30 min, (c) 1 hour and (d) 10 hours respectively.

With respect to the 3D renderings of the image stacks of Al 0.7 μm in **Figure 36**, since the relative density reaches 89% after just 30 min and further increases progressively to 94% at the end, the curvature maps in **Figure 44** have already undergone the transition observed in **Figure 43** (b) (c) for Al 1.3 μm . The shapes move further to the right at every stage, towards +1 of the shape index, signifying the spheroidization of pores, leading to their closure.

The values of curvedness, though, do not evolve much throughout the sintering sequence for both the samples. One could have expected a substantial increase in its values when the sintering was nearing its end, as a result of closed pore shrinkage. However, as proved by

Figure 39, the pores do not show significant growth at longer times. Curvedness measurement is thus consistent with this previous result. The isolated pore in the final stage of sintering in **Figure 42** (b) are hence assumed to have similar dimensional characteristics as the initial pore in **Figure 42** (a), otherwise often illustrated to be much smaller in sintering literature, in the absence of grain growth.

This study therefore permits to make a proposition of classifying the stages of sintering in terms of the evolution in pore curvature. While the classical classification of a sintering process involves three sequential stages depending on parameters such as the relative density attained and other associated microstructural evolution, pore curvature advancement clearly reveals two distinct stages. The first stage is characterized by mostly cup-like pores with values of shape indices below 0 and relative densities below, say, around 80%. The second stage pertains to the latter half of the shape index map with the pore curvatures moving towards cap-like pores, after crossing 80% of the density. A transition step occurs in between these two stages, though not precisely observed in the curvature maps.

Moreover, sintering works mainly use conventional curvature parameters such as mean or Gaussian curvature (see for example Okuma *et al.* [50]). Various authors in different fields have emphasized the interest in the parameters we chose, notably Shahani *et al.* [100], for describing coarsening in solid-liquid systems. In the field of sintering, our parameters are particularly useful in the occurrence of grain growth, as the shape index is insensitive to the grain size. It thus allows for a more relevant comparison of the state of the material at various sintering times.

3.4 Conclusion

3D investigation of micron-sized ceramic powder systems at the particle length-scale are now feasible, thanks to the ultra-high-resolution capabilities (~25 nm voxel size) offered by upgraded synchrotron facilities. Two sets of alumina powders with particle sizes of 0.7 μm and 1.3 μm were sintered and observed post-mortem using the nano-CT technique at the ID16B beamline of the European synchrotron, ESRF.

Complete 3D images were obtained for these sets of powders after sintering at a given temperature for various time periods. A comprehensive quantitative analysis was performed on the evolution of grains and pores with increasing sinter density. Several classical trends and some unusual, interesting aspects occurring during the grain and pore growth kinetics were

taken note of. Progression of grain growth was captured and validated with existing sintering theories. Accompanying pore growth was analyzed in terms of the changes in pore size and pore throat size. An equation to describe the pore size evolution valid for all the stages of sintering has been proposed. A connectivity index indicator was employed to trace and predict the density range at which the pore channels tend to close off.

Additionally, the data acquired from the 3D images was used to plot and analyze the so-called curvature maps. By virtue of this, a novel way of classifying the stages of sintering in relation to the advancement in pore curvature has been presented. The maps give information on the development of pore shapes throughout sintering, proving to be an indicator to track and assess the effect of sintering mechanisms on microstructural changes.

All of the information acquired may serve as datasets for the calibration of numerical models and for testing their veracity.

However, subtler but important effects at the local level go unnoticed in global analyses. Therefore, further thorough research including many more sintering parameters is needed in order to take into account the collective behavior occurring in a sintering process and to validate the obtained results. A real-time in-situ tracking of the sintering progression at a similar resolution scale could bring about a substantial improvement in this regard, by exploring relevant details and associated parameters at the particle length-scale. An in-situ analysis would also enable tracking of initial (and perhaps intermediate) stages of sintering by segmenting individual features. These aspects are being dealt with in our ongoing research.

CHAPTER-4

IN-SITU NANO-TOMOGRAPHY INVESTIGATION

This chapter presents the results of the *first-ever local in-situ observations* on ceramic sintering. The chapter is based on an article, '*In-situ 3D X-ray investigation of ceramic powder sintering at the particle length-scale*', that has been submitted for publication in the Journal of Ceramics International. The article is currently under review. The version reported here is the original submission, with some adjustments to fit the format and the style of the thesis.

The post-mortem experiments, achieved at the particle length-scale in **Chapter 3**, set up a framework for further tweaks and exploration in ceramic sintering observation. As stated in the chapter's conclusion, the high quality 3D images allowed us to present a global trajectory of the sintering at various time intervals. However, it could not present information on the transient phenomena, due to a lack of the follow-up of subsequent images. This highlighted the need for in-situ methods that can reveal the real-time evolution of the microstructure of ceramic particles during sintering.

The overall practical aspects of the beamline for a X-ray nano-tomography observation were defined in **Chapter 3**. Additional adjustments necessary for an in-situ observation directly inside the synchrotron beamline are factored in here. The investigation included a custom-designed high-temperature furnace, the operation of which is detailed in **Chapter 2**.

The same alumina samples that were examined in **Chapter 3** are subjected to in-situ observation here in **Chapter 4**. The set-up was effective in presenting a novel series of 3D images in the course of alumina sintering. Thanks to the super high resolution, together with the morphological aspects as in **Chapter 3**, several local scale phenomena that govern sintering local phenomena are detected and monitored over time.

Moreover, this chapter provides a comprehensive overview of the theoretical framework, the findings of the in-situ study, as well as a discussion on the implications and limitations of the research. This study further demonstrates the potential of in-situ sintering as a powerful tool for understanding and optimizing the sintering behavior of ceramic materials.

Further, for a consistent comparison of experiments and simulations, this in-situ data set is considered to be of an undeniable advantage. Consequently, a comparative study with simulations is attempted later in **Chapter 6**.

Abstract

We report an in-situ investigation of a high-temperature ceramic powder sintering performed for the first time at the particle length-scale. This was made possible by the phase-contrast X-ray nano-holotomography technique at the ID16B nano-analysis beamline of the European Synchrotron Radiation Facility (ESRF), featuring nanometer resolution (25 nm) capabilities. To perform sintering inside the synchrotron hutch, a compact high-temperature furnace was designed and developed. The sequence of real-time 3D images captured the collective behavior of the particles as well as the local-level specificities. A list of sintering indicators corresponding to the evolution of the particle shape, particle size, inter-particle neck size, pore size and pore curvature were extracted. The effect of these parameters on densification and their influence on the overall microstructural development were analyzed. Our results demonstrate the potential of synchrotron-based X-ray nano-tomography for studying complex sintering phenomena in 3D.

4.1 Introduction

The properties and performance of sintered materials are reflective of their microstructural evolution during sintering. This evolution is in turn driven by the thermodynamics and the kinetics of the sintering mechanisms [124] [125] [12] [10] [126]. Studying these mechanisms would in essence be best possible by looking not just at the macroscopic conduct, as in, by dilatometry etc., but rather by a real-time monitoring of the microstructural development in the course of sintering. A complete grasp on the intrinsic microstructure is therefore vital for a comprehensive study of sintering.

For ceramic materials, considering that sintering is the main fabrication route, the progress achieved with respect to microstructural inspection is not yet adequate. Reasons for this being - the complex architecture of the ceramic particles, their small (micron or sub-micron) size, their tendency to agglomerate, the ensuing limitations on the experimental set-ups to address these concerns and moreover, the difficulties encountered in the subsequent imaging context. As far as we are aware, no three-dimensional (3D) in-situ examination on ceramic sintering at the particle length-scale has been performed so far. A direct access to the 3D morphology of a

particle as a whole could provide us with comprehensive information about its associated arrangement, behavior and interaction with other sets of particles. This could then help us cast light on still-unresolved aspects of ceramic sintering such as, particle rearrangement, evolution of the shape of particles and pores, coupling of densification with grain growth, etc.

In the early 2000s, with the onset of the usage of X-ray tomography in material science, substantial advancements leading to 3D visualization in metallic sintering at the local particle scale were carried out, especially using synchrotron facilities [35] [37] [86] [41]. Simultaneously, Bernard *et al.* [45] were the first ones to deploy micro-computed tomography on sintered ceramic samples. Same sets of grains on pre-sintered samples were observed in 3D at the micrometer scale in an *ex-situ* framework. Baruchel *et al.* [127], in their collection of studies on X-ray tomography, illustrated the various prospects offered by the techniques in a ceramic sintering setting. They were optimistic about the forthcoming breakthroughs in the field of synchrotron X-ray sources, enabling nano-range capabilities. Furthermore, Upadhyaya *et al.* highlighted the decisive benefits offered by 3D imaging over 2D from a practical viewpoint [128]. The importance of 3D input data in modeling an ever-more accurate description of the sintering evolution was stressed upon by Exner [129].

Around the 2010s, exploring the synchrotron X-ray resources available at that time, Xu *et al.* achieved preliminary success at observing a packing of boron carbide powder in-situ during isothermal sintering. Studies were performed on the porosity evolution and the material migration between the grains in their successive works [130] and [47]. The experimental findings were found to be consistent with conventional sintering theories. Likewise, three distinct stages of sintering in alumina samples were observed and distinguished, together with a few associated phenomena from the reconstructed 3D images by Xu *et al.* [131]. The same research group further went on to qualitatively rationalize the observed 3D image results in silicon carbide particles sintering.

Nevertheless, as the spatial resolution capabilities at the synchrotron sources at the time were not fine enough to capture intricate local details, the aforementioned studies on ceramic sintering were all conducted only at an agglomerate level.

Although, of late, considerable progress has been achieved on that front. Villanova *et al.* have developed a fast in-situ X-ray nano-tomography (nano-CT) apparatus at the European Synchrotron Radiation Facility (ESRF) [5], presenting a combination of previously unheard of pixel size (few nanometers) and acquisition speed (few tens of seconds). This tomography

configuration was applied to report for the first time, an assessment of the neck curvature development during the glass-sintering process. Subsequently, nano-CT advances in other synchrotron facilities worldwide have since found applications, for example, an attempt at monitoring the high-temperature sintering of SiC/TiO₂ [132], in detecting detailed 3D morphology of defects developed during alumina sintering [133], and in examining the origin of the defects and the microstructural evolution during the sintering of multi-layer ceramic capacitors [49] [51].

More recently, taking advantage of the nano-CT route, our research group managed to carry out sintering observations on micron-sized alumina samples at the nano-scale [134]. These post-mortem experiments were undertaken at the ESRF with an unprecedented resolution of 25 nm pixel size, enabling the detection of the particle and the pore phases with ease. Classical sintering parameters were both qualitatively and quantitatively analyzed.

However, the post-mortem experiments provide only the final state of the sintered material corresponding to a specific time or temperature, without revealing the intermediate and dynamic changes in the process. A proper follow-up of the sintering parameters over time cannot be done, and a thorough understanding of the heterogenic behavior in the material, if present, is not possible.

The aim of the present work is to go beyond the limitations of the above-mentioned work and to have an even deeper exploration in the nano-CT domain during the sintering process. A successful attempt was made to track alumina sintering in-situ, in 3 dimensions, at the same super-high resolution of 25 nm, and encompassing different stages of sintering. A high temperature compact furnace was designed, developed and integrated into the X-ray nano-tomography set-up at the nano-imaging beamline of the ESRF for the same. These are the first set of high-temperature in-situ experiments to be accomplished at this length-scale on ceramic powders, offering a visual confirmation of a sintering cycle. Tackling open questions on the mechanisms and kinetics of ceramic sintering, while capturing the collective behavior taking place during a sintering process should now be feasible. Accordingly, here, key parameters governing sintering such as the inter-particle neck size, grain size, pore size etc. have been monitored over time. In addition, it was possible to take a closer look at the same set of image sections at a local level to find the existence of non-uniformity, if any. Making use of the local observations, an analysis is conducted on the evolution in the shape of the grains in the early

stages of sintering. Also, with the real-time data, the sintering process is classified into different stages based on the evolution of their pore curvatures.

4.2 Materials and Methods

4.2.1 Sample preparation

The two alumina powders considered for the in-situ investigation are from Sumitomo Chemical Co., Ltd.'s advanced alumina series – AA-07 and AA-1.3 respectively. The manufacturers claim the powders to be of superior characteristics, having high purity, uniformity, precisely controlled particle size distribution and almost-rounded polyhedral shapes [92]. The corresponding average particle sizes of the two powders were around 0.7 μm and 1.3 μm (**Figure 45**), which are compatible with the resolution achievable in the synchrotron set-up. The two powders sinter at 1500°C, as evident from the preliminary dilatometry trials conducted.

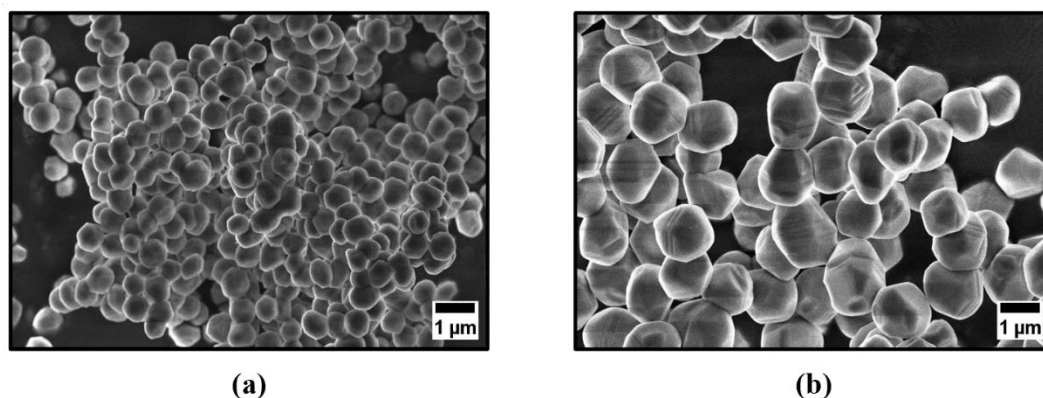


Figure 45. SEM (scanning electron microscopy) images of the chosen alumina powders with average particle sizes of around (a) 0.7 μm and (b) 1.3 μm respectively.

The powders were subjected to die compaction to instill mechanical strength enough to attain a relative density of $\sim 60\%$. These samples were further broken into tiny fragments of $\sim 100 \mu\text{m}$ in diameter and $\sim 1 \text{ mm}$ in height, so as to allow imaging of a significant number of grains under the field of view expected. The fragments were attached on to an alumina rod using a ceramic glue, to be placed on the sample holder in the synchrotron beamline and to be later introduced into the furnace.

4.2.2 Furnace - design and development

We report a high temperature compact furnace specially designed and developed (in coordination with *CERHEC, Paris*) for the in-situ studies. Extending the scope of the technique presented by Villanova *et al.*[5], the unique characteristics of the furnace open new possibilities across domains requiring this particular synchrotron investigation. The major attribute of the furnace is its ability to reach higher temperatures (1500°C) rapidly, while withstanding it for a very long duration (~50 hours for this experiment), with barely any fluctuations. It is compact and compatible with other accessories present in the synchrotron beamline. Its functioning complies with the restrictions in the beamline hutch, especially with regard to the ambient temperature and the radiation.

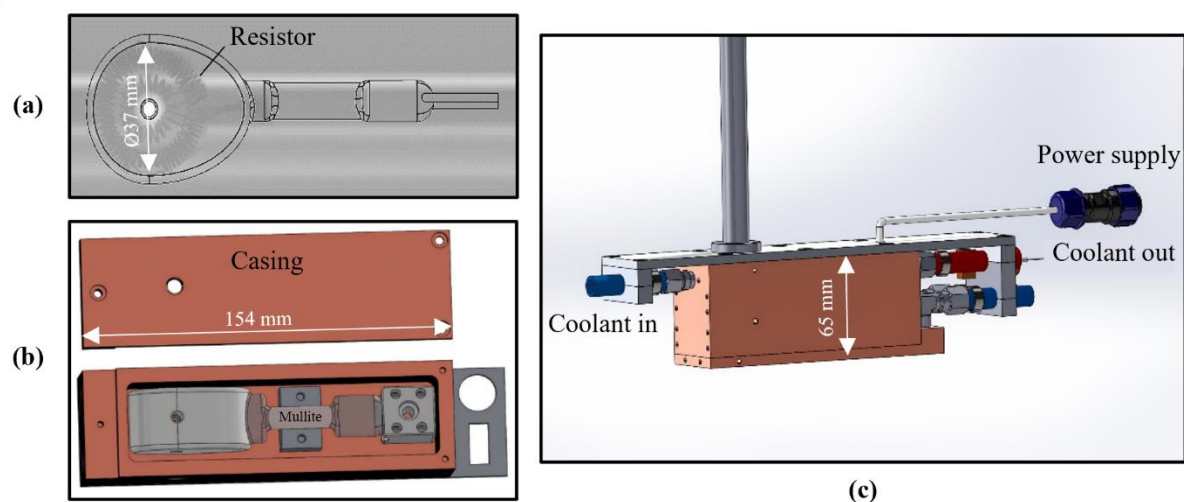


Figure 46. (a) Internal design of the furnace resistor, imaged from a laboratory tomography source (*EasyTom XL by RX-Solutions*), (b) components of the furnace system inside the casing, assembled together to set up the (c) cooling system.

Taking inspiration from the research work of Guinebretière *et al.* [75], a platinum resistor which meets the temperature requirements was used as the heating element. The internal arrangement ($\text{Ø}37$ mm) of the coils can be seen in **Figure 46** (a), providing a homogenous heating in the chamber. The resistor is wrapped in an insulating ceramic foam, with a hole in the center for beam transmission. The system is held by an arm, made of mullite (possessing lower thermal expansion properties), which is further connected to an external power supply. (**Figure 46** (b)). The components were then placed inside a casing made of copper, specially devised for an effective cooling of the system (**Figure 46** (c)). The coolant branches into 8 channels, giving a continuous surge in full flow. This constant circulation maintains the outer surface temperature of the system efficiently during the course of the experiment. This is

critical as even slight fluctuations in the temperature would have an impact on the focusing system in the hutch, which would lead to a change in the size of the source and consequently affect the nano-resolution of the images. The entire assembly is 65 mm in height and 154 mm in length. The architecture also has provisions to introduce the sample, for the X-rays to pass through, and for the insertion of the thermocouple meant for temperature measurement. The DC power supply (*delta electronica*) was set to a voltage of 42.7 V to achieve and sustain the specified temperature.

4.2.3 Synchrotron X-ray nano-tomography experiment

Isothermal sintering treatments and X-ray nano-tomography measurements were performed on the alumina samples at the nano-analysis beamline ID16B of the ESRF [54]. The beamline presents a phase-contrast X-ray holotomography system, its state-of-the-art being introduced in Villanova *et al.* [5] and the general applicability of which, especially in material science, are detailed in Mayo *et al.* [135] and Cloetens *et al.* [63].

Please refer to Venkatesh *et al.* [134] for the details on the set-up as the configuration of the experiment remained the same (**Figure 47**). Images were acquired via 4-distance imaging. 3203 projections with a pixel size of 25nm (field of view $64*64*54 \mu\text{m}^3$) were collected over 360° using an X-ray incoming beam with an energy of 29.53 keV.

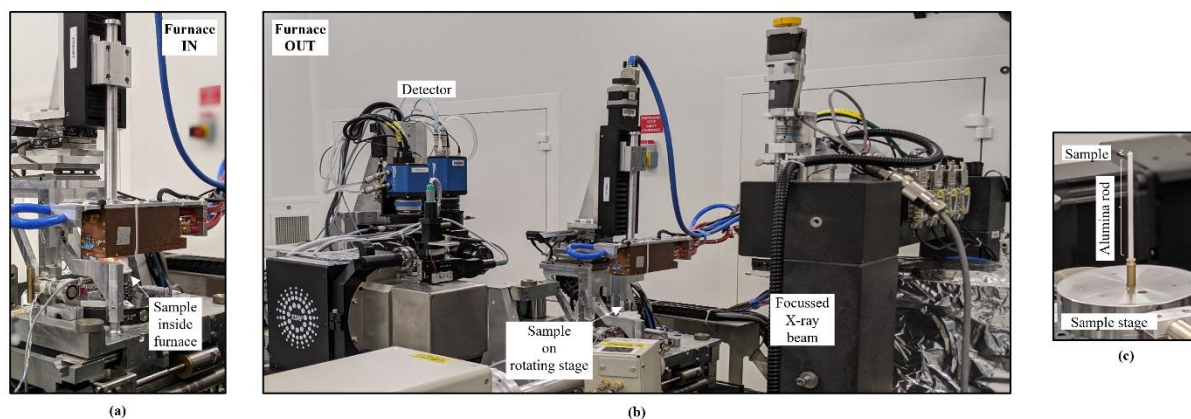


Figure 47. Stages in the nano-CT imaging: (a) heating of the furnace with the sample inside and (b) launching of holo-tomography with the furnace out of the sample. (c) Depiction of the sample placed on the rotating holder.

The alumina sample was mounted on the sample holder (**Figure 47** (c)) and aligned with the detector. The furnace was arranged in such a way that it could be moved down for the sample to be placed inside it and later taken out, as and when required (**Figure 47** (a) (b)). Thanks to

this mounting, holo-tomography could be performed with the furnace above the sample at all times, without having to dismount the sample or the furnace. This guarantees that the same area of the sample gets imaged through the experiment.

The parameters of the acquisition were validated in Venkatesh *et al.* [134], with 4-distance imaging taking ~20 min of time while achieving a resolution high enough to detect fine details in the alumina microstructure. Here, as the sample would have drastically evolved in that period of ~20 min, the scan time was not compatible vis-à-vis the sintering kinetics for a continuous in-situ investigation. Any changes in the acquisition parameters ran a risk of degradation in the resolution obtained. As a trade-off, in-situ trials in an interrupted manner were preferred to a continuous acquisition.

As in **Figure 47** (a), isothermal heating was secured with the furnace moving down on the sample for pre-defined times. After each time step, the furnace was taken out of the sample (**Figure 47** (b)), to initiate and carry out the imaging process. The X-rays passed through the sample to be recorded by the detector system. The microstructure was expected to be frozen for that period.

The entire process was automatized and controlled from outside the beamline hutch. Accordingly, the furnace was powered from an external source and the temperature was maintained at 1500°C throughout the experiment. The thermocouple in the furnace was earlier calibrated with a eutectic (Ni 23.2 wt.% Nb - 1282°C) to determine the current temperature of the sample. A recirculating cooler FL1203 (procured from *Julabo GmbH*), filled with an ethylene glycol coolant, clubbed with the effective casing design of the furnace ensured that the temperature just outside the surface of the furnace system was ~23°C, which is the regulated ambient temperature of the beamline hutch. Following the imaging, phase-retrieval based on the contrast transfer function (CTF) was carried out in an iterative fashion. Tomographic reconstruction followed by means of the ESRF PyHST2 software package [94], rendering the 3D distribution of the sample.

4.2.4 Image processing and segmentation

Ring removal

To deal with the so-called ring artefacts visible on the reconstructed volumes, a method which works on the phase-retrieved radiographs that store the information of the 2D projections, was attempted here. Errors, if present in the radiographs, later appear as rings on the reconstructed

volume. Defective detector elements, dust from the insulating wool etc., could be the plausible reasons for the same as listed out in [73] and [66].

A blend of Double flat field correction, Munch correction and Dering correction were imposed on the radiographs. The principle underlying these methods and the corresponding parameters involved are explained elsewhere [66], [73], [74]. Particularly, in Munch correction, the range of Fourier and wavelet filters were tweaked on a trial-and-error basis for adjusting the ring correction levels. A visual assessment confirmed that this approach improved the quality of the reconstructed images.

Image-filtering prescribed in Lyckegaard *et al.* [72], using a MATLAB script, worked well in the case of post-mortem experiments for the same samples in Venkatesh *et al.* [134]. This script, which targets the reconstructed volume and filters them, proved unsuccessful here at removing the rings completely.

Image registration and correlation

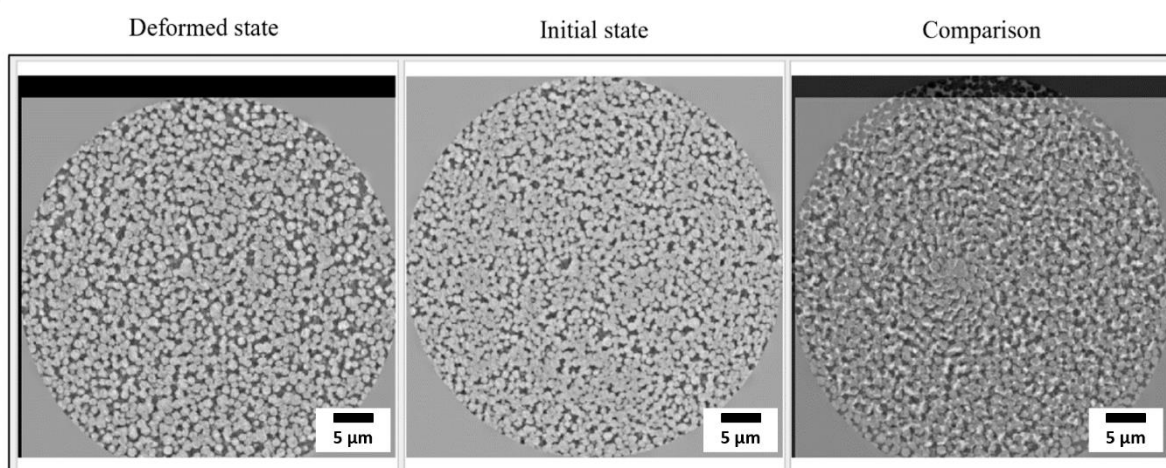


Figure 48. Visual alignment scheme in the SPAM software showing the initial eye-alignment between two image configurations of the alumina sample of 1.3 μm .

A look at the processed reconstructed volumes at different time-steps revealed misalignments (shifts and rotations) in the imaged area between the respective image states, combined with a global evolution of the sample during sintering. A manual correlation was too demanding and toolkits for image correlation provided by SPAM software were used to solve this issue [136].

To track the same regions of interest, the approach involves an initial guess to be taken by the user to deform a particular image state to match the other one (**Figure 48**). Visual feedback inputted with regard to the translations and rotations is registered as a global deformation

function Φ . This Φ was used to say, pin point a particular detail in one image state and track its progression in the subsequent state. (see SPAM documentation for more details [137]).

Along these lines, incremental correlation was performed between two sequential scans for the image stacks of all the time-steps. However, the large data size (2560*2560*2160 pixels) of the reconstructed images proved to be a constraint in SPAM. Only a few Z-slices at a time were hence considered. They were further cropped into smaller volumes of interest (VOIs) of 520*3 voxels for the following image treatment and quantitative measurements.

Segmentation methodology

Synchronized image states, once obtained, are to be subjected to pre-processing operations prior to computing quantitative analyses. The image treatment was carried out in Avizo software package [79] and consisted of the following workflow, as shown for one of the cropped image stacks of the reconstructed alumina 1.3 μm in **Figure 49** below. The instruction manual of Avizo has a detailed explanation of the methodologies and their corresponding parameters.

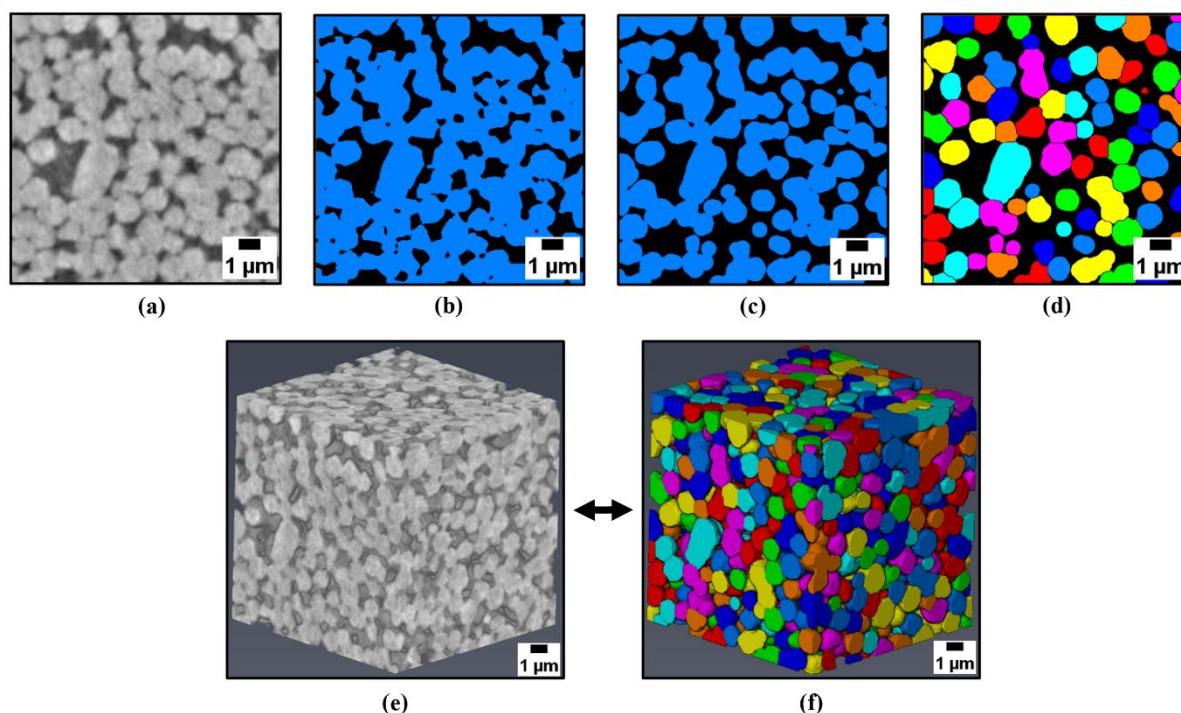


Figure 49. Steps of image improvement leading to segmentation, showing different pre-processing operations for a (a) raw image data - (b) binarization, (c) morphological opening and (d) watershed segmentation followed by labelling of grains. (e) 3D rendering of the initial volume and (f) its final segmented state.

Interactive thresholding – to convert the normalized image from before into a binarized image. While letting the threshold be chosen interactively, the image was split up into two classes - voxels of interest, i.e., the grains here in blue and the background, i.e., the pores in black (**Figure 49** (b)). A grayscale normalization was performed prior to thresholding to facilitate consistency and enhancement of the contrast in the image.

Opening – operation carried out next to smoothen the inconsistencies along the edges of the grains observed in **Figure 49** (b). It is a combination of morphological operations in 3D - erosion, which shrinks the object, followed by dilation, using a structuring element. This ends up smoothening the contours of the grains while eliminating isolated pixels (**Figure 49** (c)). A precise mode is chosen in Avizo, which ensures a structuring element matching a real sphere, referred to as ball opening, with half-kernel sizes (value of 2).

Segmentation and labelling – to split the connected components from the thresholded image for further analyses by means of separate objects module. This module performs a marker-based watershed segmentation on a distance map. The image is processed as a whole in 3D, adjusting the values of the markers (value of 2). More on watershed in the context of image processing could be found in the review work of Kornilov *et al.* [138]. The process largely fares well overall, assigning different colors to the segmented components, except in some cases where it fails to separate a few of the merged grains (**Figure 49** (d)). On rendering in 3D, the segmentation outcome looks like **Figure 49** (f) when compared to its original version in **Figure 49** (e).

Further, a label analysis module was used on the separated objects to extract a variety of statistical and numerical quantitative measures in 3D.

4.3 Results and discussion

During the in-situ measurements, the heat treatment for the two alumina samples in the furnace consisted of an increment with a rapid rate of around 40°C/min till 1500°C, and then an isothermal stay, with breaks at pre-meditated time-steps for the 4-distance imaging. For alumina with 1.3 µm particle size - Al 1.3µm, the imaging was carried out after 20 min, 40 min, 1 hour, 1.5, 2, 3 and 5 hours at 1500°C; while for Al 0.7µm, the time-steps were set at 10 min, 20 min, 30 min, 45 min, 1 hour and 2 hours of isothermal sintering. The reconstructed volumes were then treated to the image processing workflow proposed in **section 4.2.4**.

Unfortunately, for both the samples, it was not possible to follow the same regions for the initial two time-steps, even with the alignment technique in the SPAM software [136]. Pronounced particle rearrangement phenomena was noticed, as the image sections had different sets of particles with a considerable change in their numbers. The phenomena seemed to stabilize soon after and the same image sections could then be tracked in SPAM.

Particle rearrangement is an aspect of sintering which has not been thoroughly studied yet. There are, however, experimental evidences of its existence and its influence on the densification process in the initial stages of solid state sintering in the studies, to cite a few, by Exner *et al.* [139], Nöthe *et al.* [37], Wonish *et al.* [26], Wang *et al.* [140], McDonald *et al.* [141] etc. The classical theories, however, do not account for particle rearrangement, and rather only hold diffusion related mechanisms to be responsible for densification.

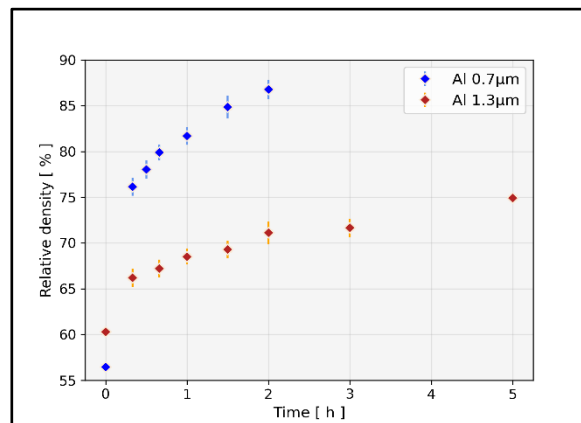


Figure 50. Relative densities as a function of time for the sintered samples of Al 0.7µm and Al 1.3µm.

The densities attained at the time-steps were determined using the ImageJ software [76]. Their progression with time is plotted in **Figure 50**. After 5 hours at 1500°C, the relative densities moved from ~60% to ~75% in the case of Al 1.3µm. For Al 0.7µm, the density rose to ~87% after 2 hours of sintering. A sharp rise in density was observed for the first time-step, with a gradual increment later on. Based on the densities reached, the samples ought to be in the initial (till ~70% of density) and intermediate (~70 to ~90% of density) stages of sintering. The time constraints with respect to the in-situ set-up were not conducive enough to let the samples reach the final stage (over 90% of density).

For the time-steps that were possible to be followed-up, evolution in one of the cross-section slices of the 3D reconstructed alumina samples of 1.3 μm and 0.7 μm are displayed in **Figure 51** and **Figure 52** respectively.

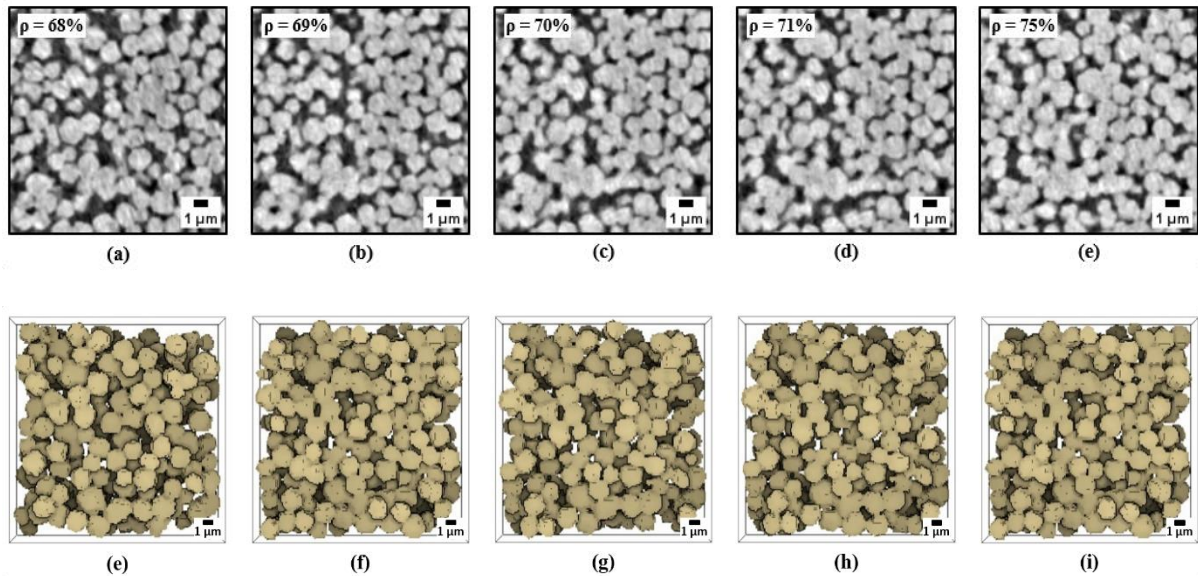


Figure 51. Follow-up of a cropped section of the in-situ observation of the 3D reconstructed Al 1.3 μm , with the corresponding 3D rendering below, after (a) (e) 1 hour, (b) (f) 1.5 hours (c) (g) 2 hours, (d) (h) 3 hours, and (e) (i) 5 hours of sintering at respectively. The relative density values ' ρ ' are mentioned on top-left. Scale bar is 1 μm .

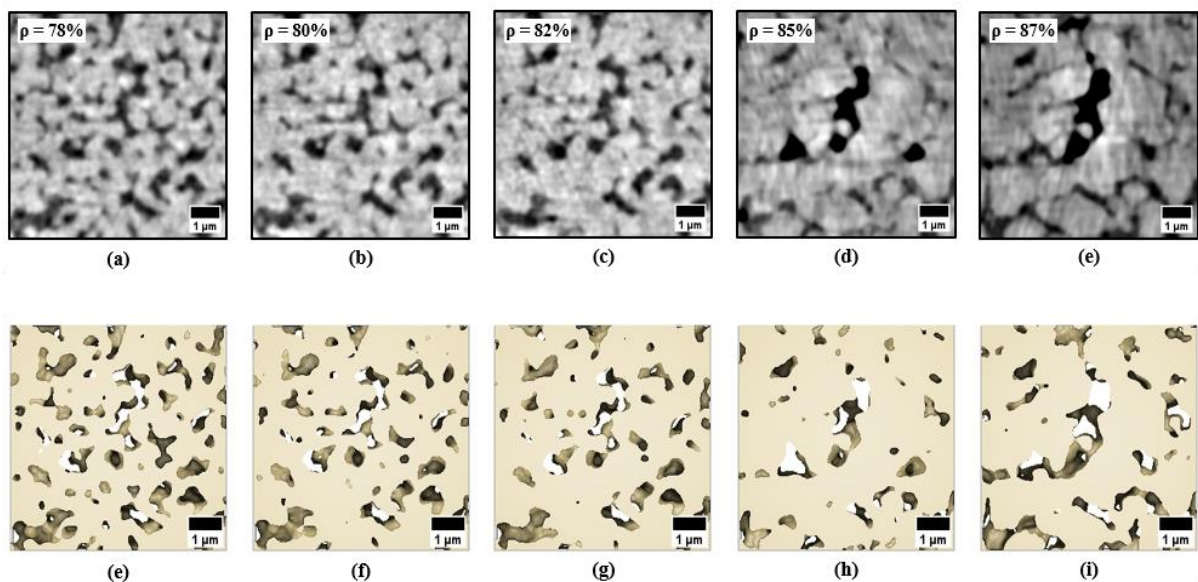


Figure 52. Follow-up of a cropped section of the in-situ observation of the 3D reconstructed Al 0.7 μm , with the corresponding 3D rendering below, after (a) (e) 20 min, (b) (f) 30 min (c) (g) 45 min, (d) (h) 1 hour, and (e) (i) 2 hours of sintering at 1500 $^{\circ}\text{C}$ respectively. The relative density values ' ρ ' are mentioned on top-left. Scale bar is 1 μm .

The grain segmentation methodology proved feasible for Al 1.3 μm but not for Al 0.7 μm . Consequently, quantitative analyses that require an effective segmentation such as the evolution of the inter-particle necks and grain shapes have been achieved with Al 1.3 μm only. And, the analyses that do not need a segmentation, like the progression of the grain and the pore sizes, and the pore curvatures, were carried out for both the powders.

Grain size and pore size estimation

The size of the evolving grains was estimated using granulometric analysis in the GeoDict image processing software. A thorough explanation of the algorithm and its implementation is contained in [95]. Granulometry does not require the separation of individual particles as it is only a geometrical assessment. Another method to estimate grain size involves segmenting the grains into separate entities. As detailed in **section 4.2.4**, after the segmentation in Avizo, label analysis was carried out on the grains to measure their sizes to later average them by volume. Meanwhile, the pore phase was subjected to only granulometry analysis in GeoDict as the separation of individual pores would be a rather vague exercise [96].

Grain size evolution

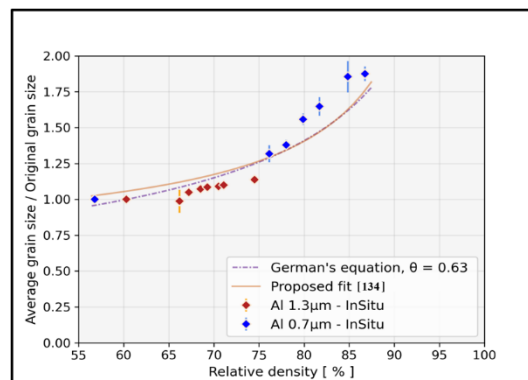


Figure 53. Comparison of average grain size over original grain size versus density for the two alumina samples, Al 0.7 μm and Al 1.3 μm , along with the corresponding curve-fit according to the equations proposed by German [108] and Venkatesh *et al.* [134].

For the in-situ image stacks here for both the alumina powders, grain size measurements by means of granulometry were taken from multiple cropped stacks at different regions in the image over each time-step. The evolution of grain size was noted and plotted on a graph of average grain size over original grain size versus the relative density attained at those time-steps (**Figure 53**). The variability of data at each time-step was taken into consideration and plotted in terms of error bars.

For Al 1.3 μm , the variability, mostly limited in its range, suggests that the grain growth is homogeneous at this stage of the sintering. The relatively higher variability at the first time-step could be a consequence of the observed particle rearrangement phenomena. The grain size progression is almost flat and shows no considerable increase till the density of $\sim 75\%$ is reached. The 2D stack follow-up shown earlier in **Figure 51** substantiates this size progression behavior. Additionally, post segmentation, grains were also measured individually in the case of Al 1.3 μm . This method gave out similar outcomes as in the granulometric analysis, as the density is limited to $\sim 75\%$. However, beyond this density, at later stages of sintering, a convergence in the values cannot be expected due to failure of the segmentation approach.

For Al 0.7 μm though, a significant increase is seen at each passing time-step, together with slight changes in the variability of the data. The average grain size gets almost doubled on reaching a density of $\sim 87\%$. The fact that the smaller alumina powder Al 0.7 μm shows a relatively faster densification coupled with a more intense grain growth is reflected in the **Figure 52**, displayed earlier. Rapid disappearance of grains, mostly the smaller ones, could be noticed over time as well, acting as a reason for increasing the average grain size.

To track the grain size progression, in Venkatesh *et al.* [134], an equation proposed by German [108], [109], $G = \frac{G_o \theta}{\sqrt{1-f}}$, was found to deviate from the obtained points at densities over 85%. In this equation, G_o is the initial grain size, θ is a constant with a value of 0.6, and f is the grain volume fraction. A revised equation covering all the points in a reasonable manner was hence proposed, which read $\frac{G}{G_o} = a \exp\left(\frac{b}{\sqrt{1-f}}\right)$, with two constants, $a = \sim 0.5$ and $b = \sim 0.4$ respectively. As the maximum densities do not go well past 85%, both the above stated equations fare well here by coming close to encompass the obtained range for the grain size values for both the powders, as seen in **Figure 53**.

Furthermore, although from **Figure 51** and **Figure 53**, it could be assumed that the whole of Al 1.3 μm would report a regular grain growth behavior at this stage of sintering, taking advantage of the available in-situ images, a closer local observation was attempted. Interestingly enough, it revealed localized heterogeneities at a few locations. **Figure 54** shows one such instance.

This set of images displays a disproportionate consumption of the smaller grains, leading to their gradual disappearance over time. This feature of coalescence, where two grains merge to

create a single grain progressively, is a prominent aspect of grain growth and is generally a highlight of the final stage of sintering.

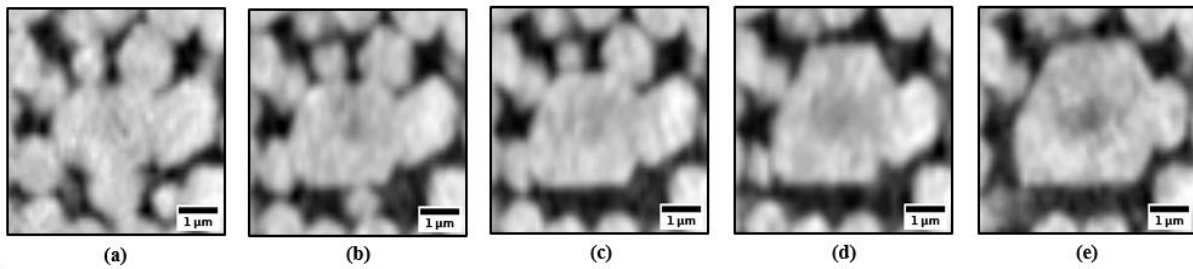


Figure 54. Follow-up of the particle coarsening phenomena for the in-situ observation of Al 1.3µm after (a) 1 hour, (a) 1.5 hours (c) 2 hours, (d) 3 hours, and (e) 5 hours of sintering at 1500°C respectively.

Nevertheless, Kang [10] and Rahaman [12], in their review publications on sintering, have cited peculiar situations which could lead to such particle coarsening in the initial stages. According to German [108], this type of behavior could arise in the case of large grain size differences - the larger grains would eventually eat their smaller neighbors and grow at their expense. As the larger grains have a lower surface energy per unit volume, incremental surface diffusion events across the neck interface progressively swell them up while eroding away the smaller neighboring grains with a higher surface energy. Coarsening becomes much more prominent in the late intermediate and the final stages of sintering, but unfortunately the images available here are limited to a relative density of 76%. Further pursuit beyond this density would bring an added value to check the preferential growth of these large grains developing from the initial large seed particles and their influence over time on the overall microstructural evolution.

Yet, this local phenomenon does not have a significant impact on the overall behavior and statistics, as evident from the negligible variability in the data from the graph.

Pore size evolution

Together with the grain size estimation, a clearer interpretation of microstructural development also requires an understanding of how the pore network develops. An estimation of the pore size evolution, normalized with respect to the average grain size, is therefore plotted as a function of density in **Figure 55**.

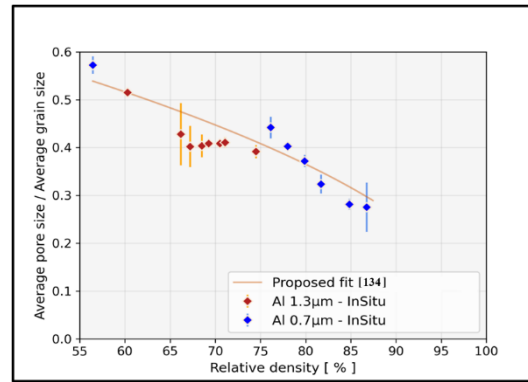


Figure 55. Comparison of average pore size over original grain size versus density for the two alumina samples, Al 0.7µm and Al 1.3µm, along with the corresponding curve-fit according to the equations proposed in Venkatesh *et al.* [134].

In the case of Al 1.3µm, a limited reduction in the pore size can be seen. The size ratio decreases from the initial ~0.5 to ~0.4 after 75% density. As observed in **Figure 51**, the pore phase is still continuous, since the sintering is still in the intermediate stage. On the contrary, as Al 0.7µm has been sintered till around 90%, gradual changes in the pore network, initially all connected, could be observed in **Figure 52**. The larger pores originally present in the initial green state shrink, coinciding with an increase in the densification. As a result, a much sharper reduction in the average pore size is noticed in **Figure 55**, as compared to the evolution in Al 1.3µm. The pore size has nearly halved from ~0.6 to begin with to ~0.3 on reaching ~87% density.

Moreover, a larger variability in the data could be noted here in the pore size evolution as opposed to the grain size observations. This could be due to the fact that the porosity could be larger in areas where the initial packing was not optimal.

As in the case of grain size evolution, an equation valid for all the stages of sintering, $p = G \left(\frac{\varepsilon}{1.5} \right)^{1/2}$, where p is the average pore size, ε is the pore volume fraction and G is the average grain size, was proposed in Venkatesh *et al.* [134] to predict the evolution of the pore size. The proposed equation fits well and passes through the range of pore size values at each time-step for the in-situ images.

To corroborate the above-mentioned findings, a local observation was also carried out on the porosity phase of Al 0.7µm, the 3D renderings of which are displayed in **Figure 56**. It captures the interplay of a variety of phenomena in the pore network, such as the large pore in the center (in yellow) getting ruptured and steadily losing its branches; the pores smaller in size (in pink) disappearing completely; and some of the bigger pores either remaining the same or slightly growing (in white).

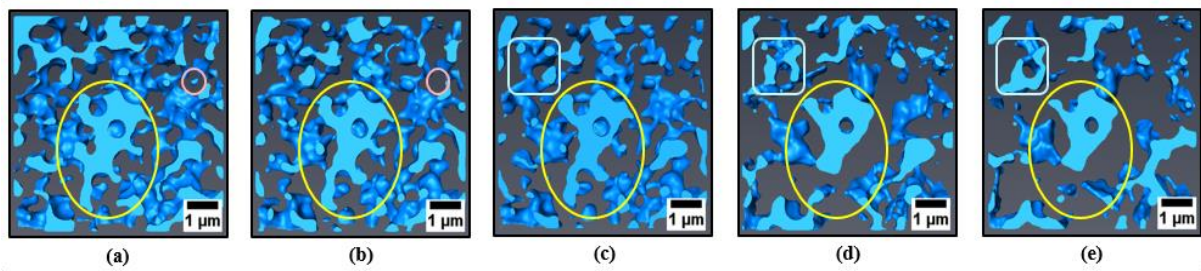


Figure 56. Follow-up of the mechanisms occurring in the pore network for the in-situ observation of Al 0.7µm after (a) 20 min, (b) 30 min, (c) 45 min, (d) 1 hour and (e) 2 hours of sintering at 1500°C respectively.

Grain shape evolution

For obvious reasons, grain shape variations during ceramic sintering have never really been tracked and observed at the particle scale. Here, morphological changes in the grain shapes have been investigated through the evolution in values of their sphericity and smoothness. For this purpose, image stacks after Avizo-segmentation (section 4.2.4) were fed into the GrainFind module of GeoDict [95]. The discussion here is limited to Al 1.3µm as the observations on Al 0.7µm and consequently their grain segmentation are relatively harder.

The sphericity analysis in the module allows for the best possible grain-fit in terms of ellipsoids into each segmented grain. While there are a lot of ways in which sphericity could be defined and calculated, Krumbein's definition of sphericity [142], which is an isotropic measure, reading, $S = \sqrt[3]{\frac{bc}{a^3}}$ is adopted in this work. a , b and c are the three principal axes of the ellipsoid (with 'a' being the length of the longest axis, while 'b' and 'c' are the lengths of the other two shorter axes). S takes the values from 0 to 1, with 1 marking a perfectly isotropic grain.

For the in-situ image stacks of Al 1.3µm, as in **Figure 57**, the Krumbein sphericity values obtained are plotted against their relative frequency.

At the green state, we expected our almost-rounded Al 1.3µm powder to have a sphericity of close to 1. However, as seen in **Figure 57** (a), the sphericity in the initial state is spread across a range of values. This goes on to say that the powder system indeed consists of particles that are anisotropic in nature. After 20 min of sintering, at the first time-step (**Figure 57** (b)), a sharp transition in the values is seen in the graph. The sphericity values then shift gradually to the right from **Figure 57** (b) onwards at every time-step till ~1 hour of sintering (**Figure 57**

(c)). Later, a slight indication of a leftward shift is observed for the images after 5 hours, as in **Figure 57** (e). After this point, with prolonged heating and the resulting progressive increase in grain size, the sphericity values are speculated to decrease and further move to the left. The underlying reason for this behavior is pursued with the help of scatter plots, displayed adjacent to the corresponding sphericity assessments. The plots classify the shape of the fitted ellipsoids into 4 categories: spheres, prolates, oblates and flat-bars. Spheres have equal lengths for all three axes of the ellipsoid. Prolates have one axis longer than the other two, which are equal. Oblates have one axis shorter than the other two, which are equal. And, flat-bars have two axes much shorter than the third one.

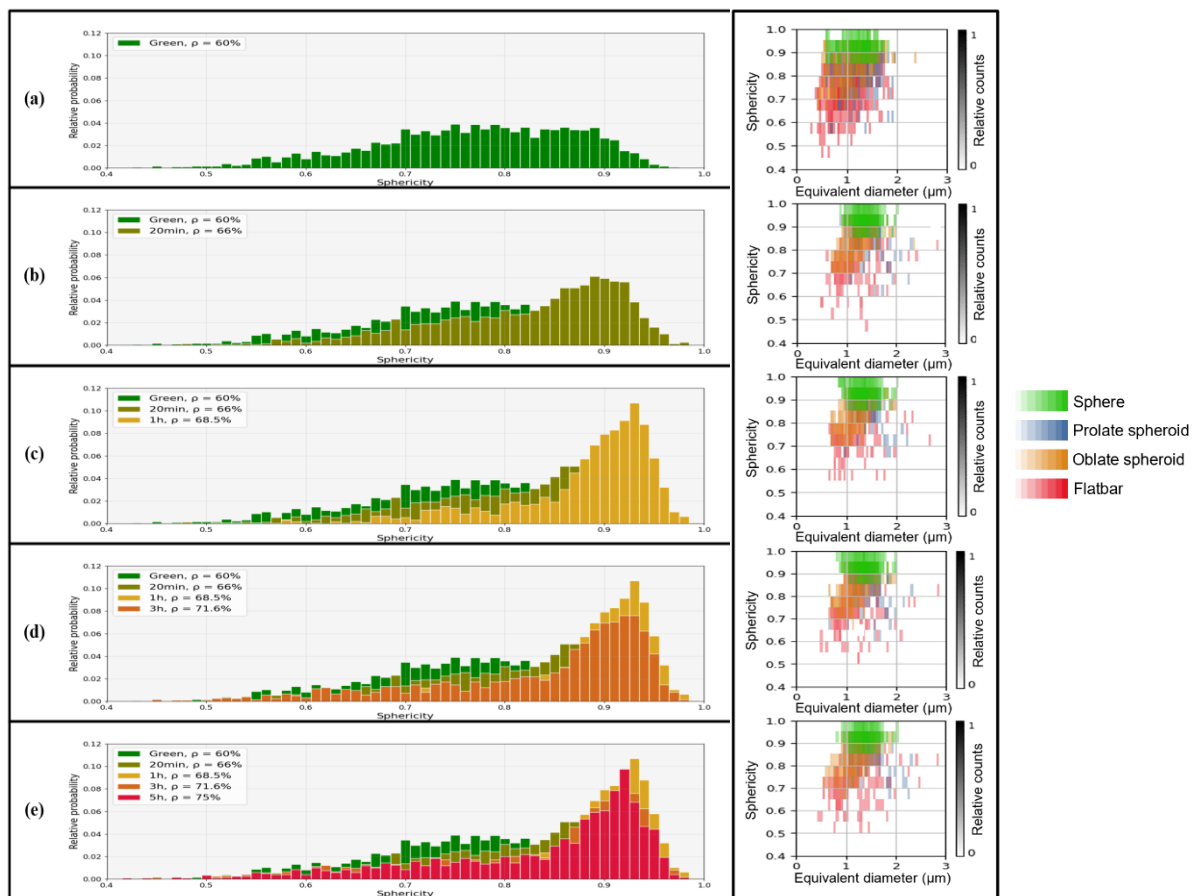


Figure 57. Evolution of sphericity for the in-situ X-ray nano-CT observation of Al 1.3 μm at (a) the green state, and after (b) 20 mins, (c) 1 hour, (d) 3 hours and (d) 5 hours of sintering at 1500 $^{\circ}\text{C}$ respectively, with their corresponding scatter plots.

Equivalent diameter and the sphericity of the particles, together with their relative counts, are chosen as the variables for the plot. Comparing the first two plots, it is evident that a large number of non-spherical particles tend to disappear or turn close to spherical at the very first time-step. Also to be noted is that these are mainly the smallest particles in the considered stack. The grains could have also simply merged with their neighbors as a consequence of

particle coarsening detailed earlier. The subsequent plots show a similar trend, with less drastic changes. However, the number of spherical particles either increases slightly or remains stable throughout the time-steps in consideration. The relatively larger particles appear to stay put. Towards the end, after 5 hours, a marginal increase in the number of irregular particles could be observed, which is probably because of grain interactions leading to improper segmentation.

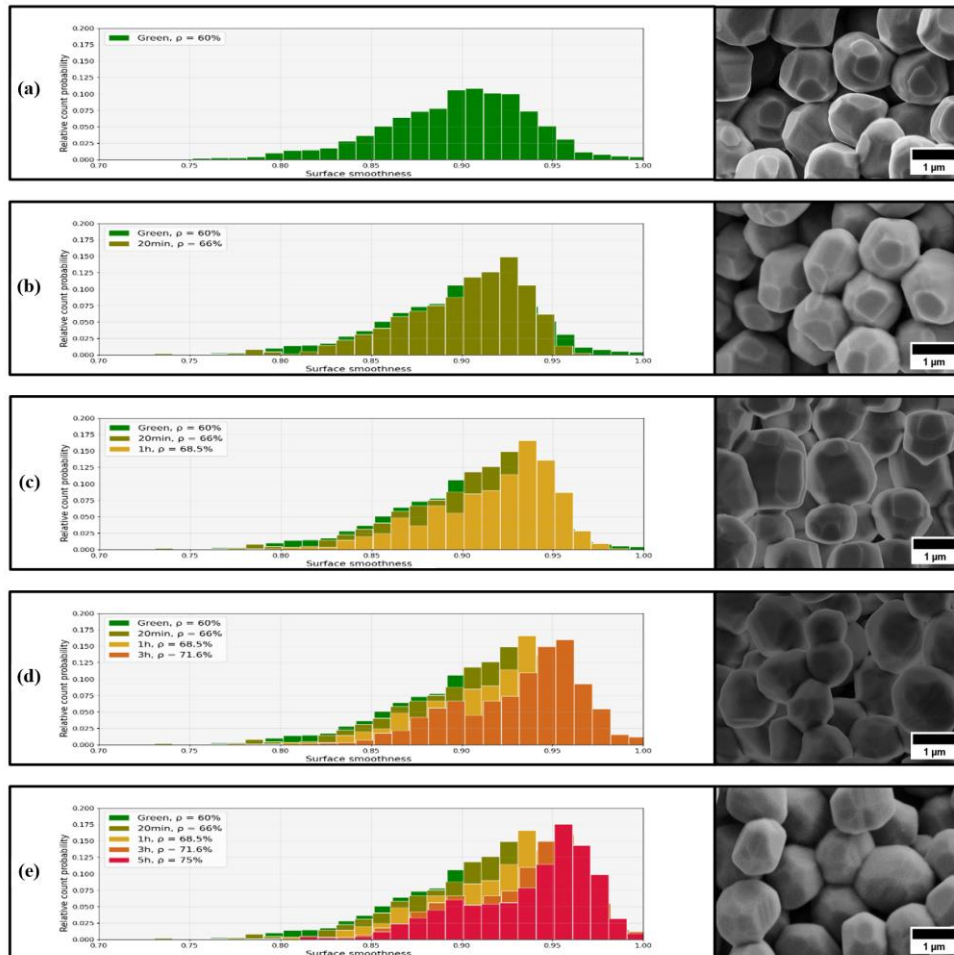


Figure 58. Evolution of surface smoothness for the in-situ X-ray nano-CT observation of Al 1.3µm at (a) the green state, and after (b) 20 mins, (c) 1 hour, (d) 3 hours and (e) 5 hours of sintering at 1500°C respectively, with their corresponding SEM observations.

Another aspect that we investigated with regard to the grain shape was the variations in the smoothness of the surface of the grains over time. We used a method that calculates the surface of the segmented grains by an algorithm put forth by Ohser *et al.* [82]. Smoothness value of each grain is then based on the surface of the best-possible-ellipsoid-fit into these grains divided by the algorithm-calculated surface. The values range from 0 to 1, where 1 means the grain is perfectly rounded.

Figure 58 shows the probability plot for the surface smoothness. Although the average value of the smoothness value is around 0.9 initially, the distribution hints at the presence of grains having rougher surfaces than others. Further, as the time progressed, we observe that the smoothness value only increases, indicating the consequent smoothing of the grains. Surface diffusion is expected to be behind this transition, as the diffusion mechanism would first smoothen the edges and corners of the polyhedral shape and transform it into a smoother version of the same. Combining this assessment with the earlier observation in the sphericity section, smaller grains which seem to vanish at the start could have been aided by their relatively faster tendency to undergo diffusion mechanisms. This would result in a better fit of the ellipsoid approximation, ensuing in an increase in the smoothness values.

To cross-check the observed phenomena, since we could not co-relate the first few of the tomography images (**section 4.3**), samples sintered up to the given time-steps were subjected to SEM examinations. The observations, shown besides each time-step for the in-situ graphs in **Figure 58**, were carried out using secondary electrons, SE2, so as to capture the details from an angle, with good topological contrast. The SEM studies reveal that the presence of facets in the initial polyhedral is responsible for the lower smoothness values. The initial particles are seen to turn smoother before the actual sintering begins; and over time, the facets can clearly be observed to disappear. This confirms the initial increase noticed in the smoothness plots and their stabilization later. Also, with increasing time, grains appear to come closer towards each other as a consequence of sintering.

Integrating the observations from the plots presented in the section, one or more factors that influence the grain shape behavior can be summarized as follows:

- Smaller irregular grains tend to merge with other grains due to the particle coarsening phenomenon discussed in the previous section.
- Smaller grains also experience a faster diffusion process than larger grains, resulting from shorter diffusion paths. This is supplemented by the loss of facets and the formation of smoother and isotropic grains.
- Larger or regular grains mostly maintain their shape and size in the initial stages of sintering.

The grain shape phenomenon observed in such particular powder systems, coupled with thorough research on the geometrical aspects involved could evidently bring about valuable new information to the modelling realm. The classical theories of sintering are generally

described using idealized models represented by spheres for the initial stage; while the grains are assumed to adopt the shape of a tetrakaidecahedron, enclosing cylindrical-shaped pore channels at their edges in the intermediate stage; and spherical pores at their corners for the final stage [10], [12]. A fully accurate module as per Coble *et al.* [14] should take into account progressive changes in grain shapes. And, according to German, a comprehensive analysis on grain shape progression could lead to the usage of grain shape, instead of grain size, as the basis for predicting grain growth or shrinkage [108].

Neck growth

The commencement of sintering is marked by the formation of so-called necks at the particle junctions. These necks show an incremental evolution during sintering and their quantification serves as an ideal indicator to monitor the progress of sintering. The high-resolution 3D images here permit us to visualize the necks at the local level and are therefore well-suited to provide a better picture.

As the grain segmentation with regard to Al $0.7\mu\text{m}$ does not yield satisfactory results because of higher densities, the analyses were carried out only on Al $1.3\mu\text{m}$. Following the thresholding operation, opening operation and the segmentation in Avizo, a logical difference AND NOT is performed with the post-opening and post-separation images as the two input images [79] (**Figure 60**). This gives out an image with only the inter-particle contacts. A labelling operation is carried out subsequently to separate the connected components and display the individual necks. Measurements on the labelled necks are not straightforward because of their varying shapes. So, a ‘feret’ concept is used for the calculations, where in the length of an object is computed along different directions and the maximum of all is considered.

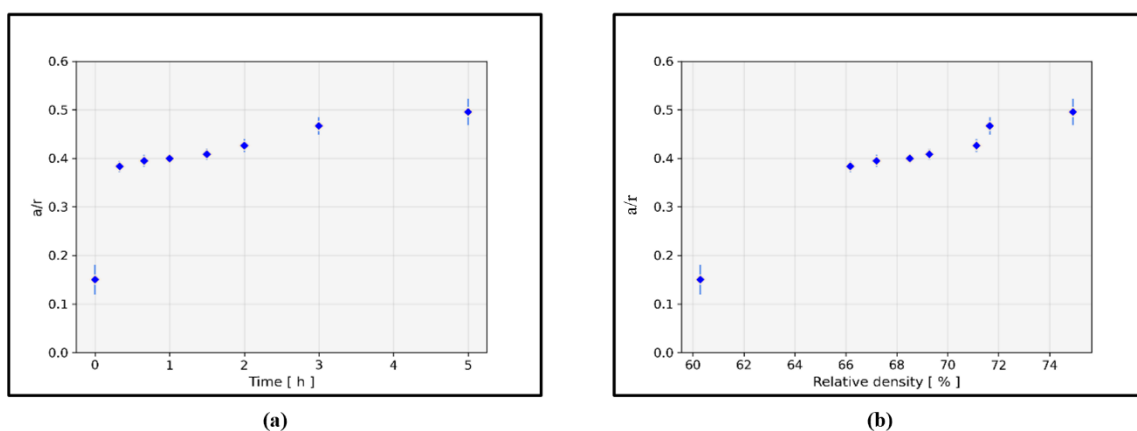


Figure 59. (a) Growth of the average inter-particle neck ratio (a) over time and (b) versus density for the alumina Al $1.3\mu\text{m}$.

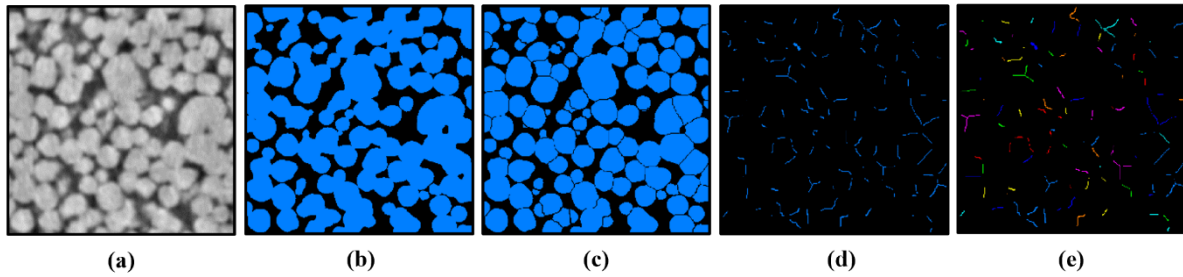


Figure 60. Steps in the retrieval of the necks from the (a) image stacks of Al 1.3µm - (b) thresholding + opening operation, (c) segmentation, (d) logical operation, (e) labelling of necks.

Neck growth is commonly expressed as the change in neck size ratio, a dimensionless parameter corresponding to the ratio of the neck radius ‘a’ to the particle radius ‘r’ (half of the average grain size). This ratio denotes the degree of sintering and, as per German [109], the value of the ratio up until 0.5 corresponds to initial and intermediate stages of sintering, and more than 0.5 to the final stage of sintering. This makes 0.5 the transitional value between intermediate and final stages.

Figure 59 (a) shows a plot of the average neck size ratio versus the sintering time taken from different VOIs for Al 1.3µm, with the corresponding variability in the data. The neck size ratio, taken into account from the time $t = 0$ of the sintering plateau already has a value of ~ 0.15 . A huge increment in the value can be observed for the first time-step of 20 min. Later, with increasing time, the average neck ratio ‘a/r’ shows a progressive increase. From a density perspective (**Figure 59** (b)), the values go from ~ 0.15 to ~ 0.5 for the densities from $\sim 60\%$ to $\sim 76\%$ after 5 hours. The ratio would further certainly increase beyond 0.5 with increase in sinter time, while not having yet reached the final stage of sintering. The trajectory would therefore go on and not satisfy the postulation by German mentioned above.

With regard to neck growth kinetics, many models are found in publications by Kuczynski *et al.* [16], Kingery *et al.* [17], Coble *et al.* [13] and Johnson *et al.* [143]. They have been summarized and expressed in a general form by Rahaman [12] as $\left(\frac{a}{r}\right)^m = \frac{H}{r^n} t$, where ‘H’ is a term made up of material and geometrical parameters of the powder system, while ‘m’ and ‘n’ are constants typically with values corresponding to a sintering mechanism. The retrieval of ‘m’ from this time-dependent neck growth behavior would then hint at the possible sintering mechanism and thereby the different growth kinetics acting on the system at different times.

However, the linear fitting in this case has been unsuccessful, pointing out the fact that the powder system in hand is too far away from an ideal system assumed in the model. The model fares well for two spheres equal in size, but as seen in **Figure 61**, Al 1.3 μm constitutes particles of different sizes and shapes and, consequently, necks of different sizes and shapes.

Furthermore, the expression above assumes a point contact at the beginning of the sintering plateau, which is not the case in this context as well.

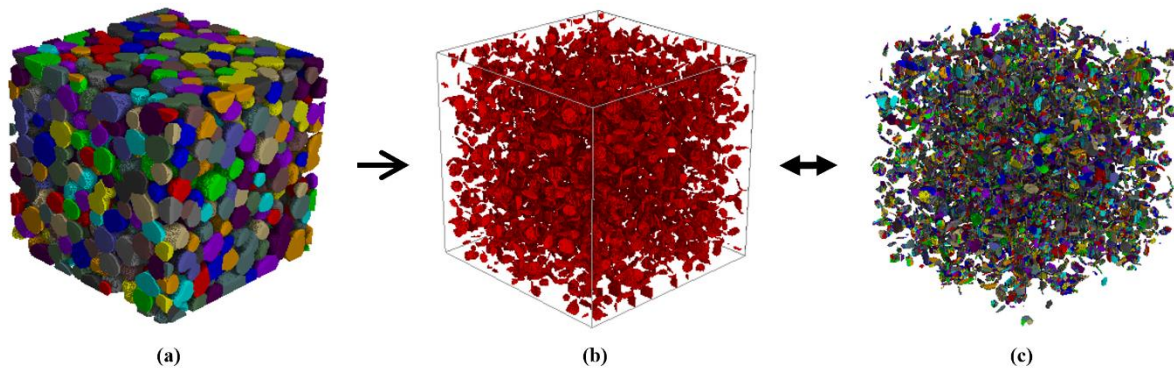


Figure 61. Close-up of (a) cropped segmented section of alumina Al 1.3 μm and its corresponding neck morphology, (b) prior to segmentation and (c) post-segmentation.

Curvature maps

Two shape indicators, namely, Shape Index (S) and Curvedness (C) were found to be well-poised to quantify the 3D morphology of pore-solid interface curvature. These two indicators are formulated as, $S = \frac{2}{\pi} \arctan\left(\frac{k_1+k_2}{k_1-k_2}\right)$ and $C = \sqrt{\frac{k_1^2+k_2^2}{2}}$, respectively. k_1 and k_2 in the equations are the principal curvatures. These representations are de-coupled from one another and represent distinct properties of a surface [98], [122]. The shape index conveys relevant information on the shapes surrounding surface points, while curvedness is a measure of deviation from a flat surface [100]. These indicators can be computed and interpreted in terms of 2D histograms called ‘curvature maps’, normalized with a probability density P(S,C).

The constituents of the curvature map, shape index and curvedness are represented as in **Figure 62** for a visual comprehension.

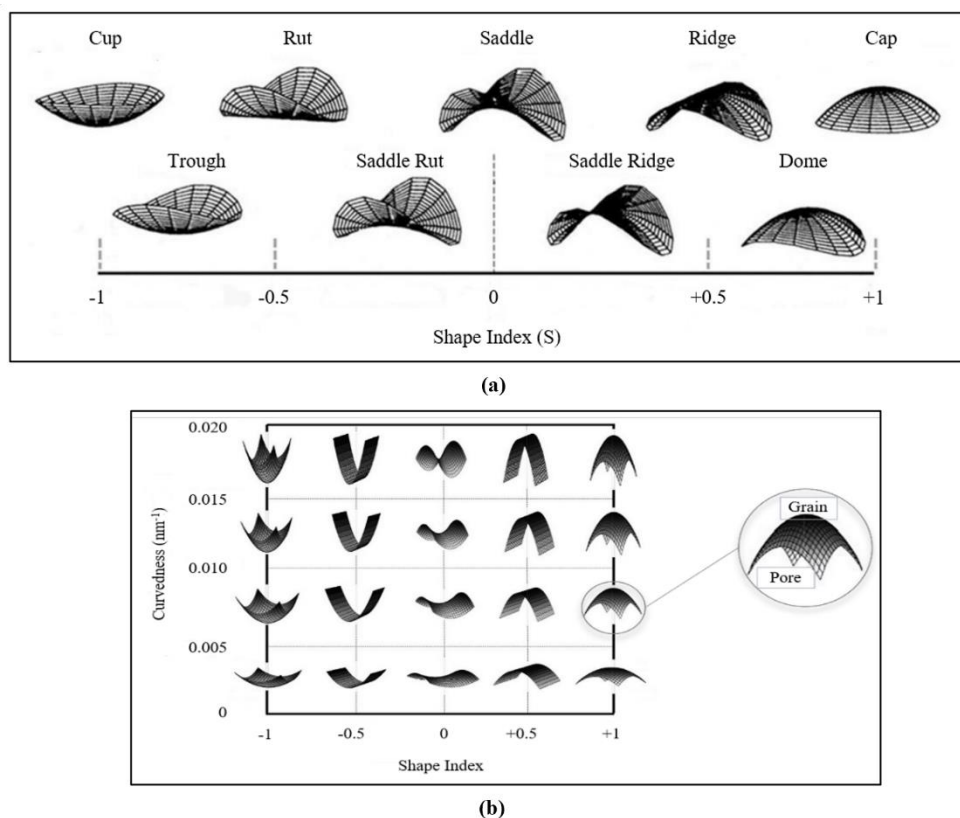


Figure 62. (a) Several local shapes fitted in the shape index profile [122], (b) depiction of increasing curvedness values with respect to shape index (Adapted from A. Burr).

Figure 62 (a) shows an array of local shapes with their corresponding shape indices. The shape index carries all the pertinent information in the form of a single number, either negative or positive, to wholly describe interfacial shapes, as opposed to the requirement of two different measures, like the Gaussian and mean curvatures [100]. A concave-shaped cup-like profile has a shape index value of -1, while it is +1 for a convex-shaped cap-like profile. The convexities are separated from the concavities by a symmetric saddle-like profile in the middle with an index value of 0. **Figure 62** (b) indicates that the curvedness is a positive value, and an increase in its value represents a more angular surface. A flat plane would have a value of 0 for both the shape index and the curvedness.

Preceding study on pore curvature maps in Venkatesh *et al.* [134] demonstrated their potential to trace the distribution of the pore-interface shapes for the set of post-mortem image stacks at different sintering time intervals. Taking a cue from this, with an aim of capturing the pore interface shape evolution in the initial stage of sintering, curvature maps in the (S,C) plane were plotted as in **Figure 63**, for the 3D renderings of the in-situ image stacks of Al 1.3 μ m. With reference to the shape index profile in **Figure 62** (a) (b), the initial spread after 1 hour of

sintering primarily comprised of rut-like shapes (**Figure 63** (a)). The distribution then showed a clear, continuous movement in the rightward direction (**Figure 63** (b) (c)), with increasing sinter time and density. The shapes gradually evolved and concentrated around different saddle-like shapes on reaching $\sim 75\%$ relative density after 5 hours of sintering in **Figure 63** (d). These cylindrical saddle shapes represent the interconnected open porosity present at this stage, formed as a consequence of neck growth and the resulting densification.

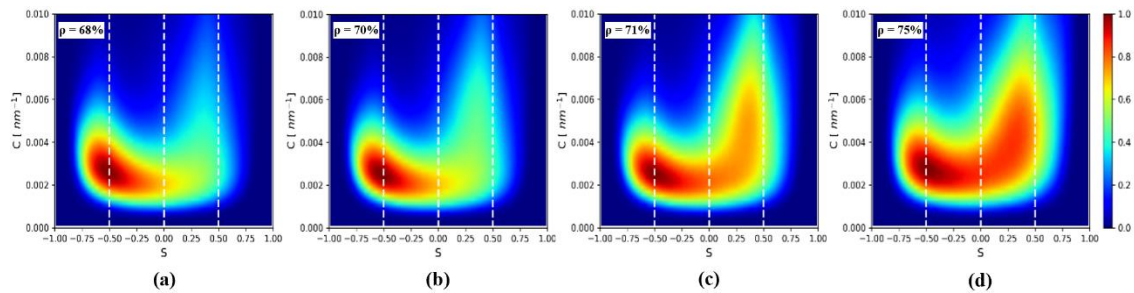


Figure 63. Pore curvature maps for the in-situ observation of Al 1.3 μm after (a) 1 hour, (b) 2 hours, (c) 3 hours and (d) 5 hours of sintering at 1500°C respectively.

Furthermore, as the available Al 1.3 μm stacks are restricted to $\sim 75\%$ density, in order to check the behavior of the maps at a higher density, Al 0.7 μm image stacks were used as they already attain 76% of density after just 10 min of sintering. The curvature maps are plotted for Al 0.7 μm in **Figure 64**. The probability density P in the maps is around the saddle-like shapes in **Figure 64** (a). With increasing density, in **Figure 64** (b) and (c), a transformation in the distribution is observed and P moves significantly to the right, going past the saddle shapes and settling around ridge-like shapes (shape index of ~ 0.5).

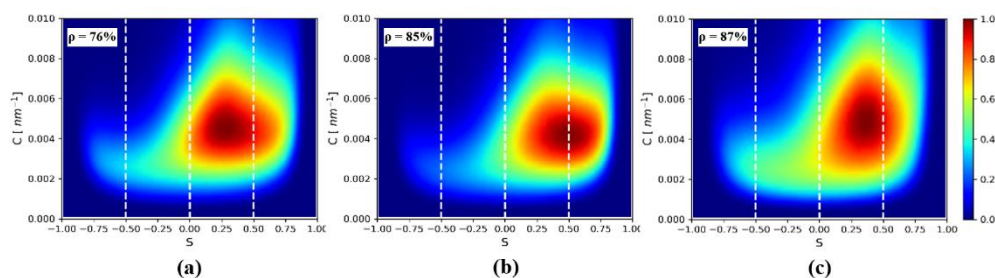


Figure 64. Pore curvature maps for the in-situ observation of Al 0.7 μm after (a) 10min, (b) 1 hour and (c) 2 hours of sintering at 1500°C respectively.

Although they are two different powders, we can gather **Figure 63** and **Figure 64** in order to trace a continuum of sorts. With this information, it is safe to assume that the maps for Al 1.3 μm , except for their shape, would have undergone a transition at just about 75% density and converged into a distribution like the one seen in **Figure 64** (a) onwards, only to further follow the rest of the map and keep moving to the right during the course of sintering.

This is consistent with the observations made for the post-mortem stacks in Venkatesh *et al.* [134]. The distribution there moved from the left and advanced towards the right with each passing time interval. Taking advantage of this, an attempt was made to categorize the sintering process into two distinct stages based on the evolution of the pore shapes: an initial stage with more of cup-like pores and another stage corresponding to cap-like pores. The maps there, however, missed out on the changeovers occurring in between particular time intervals. Although, here, the interrupted in-situ observations do not necessarily disclose startling new information, the time-steps of much shorter extent succeed in giving an added visual information to explain the phenomenon of gradual shifts in the maps and the transition at around 75% density, which were only a subject of speculation in Venkatesh *et al.* [134].

Additionally, the in-situ images are predominantly expected to not just provide statistical changes over sintering time, but offer insights on how this statistical information could be understood in terms of local observations. As the same set of microstructural details can be monitored, a follow-up of the pore-interface evolution would help decipher the curvature maps more precisely.

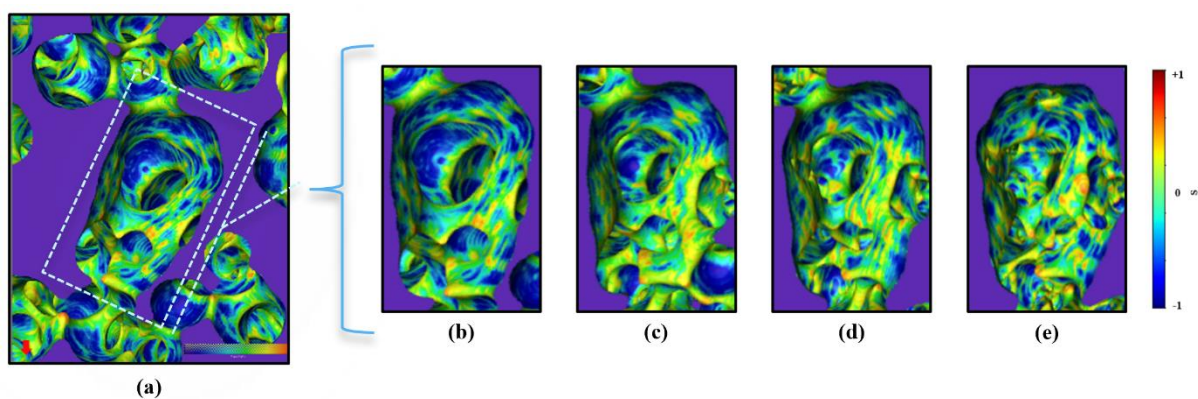


Figure 65. Snapshots of the (a) 3D rendering of the shape index values of the evolving pore network, for the in-situ observation of Al 1.3 μm after (b) 1 hour, (c) 2 hours (d) 3 hours and (e) 5 hours of sintering at 1500°C respectively.

Accordingly, a cropped section of the pore network is 3D rendered below in **Figure 65**. It shows the gradual local variation in the shape index values explained above. A closer look at the rendering from in **Figure 65** (b) to in **Figure 65** (e) shows an increasing number of higher intensity points on the scale bar for the shape index. This in turn suggests the gradual shape variation happening at the local surface level and the resulting rightward shift in the shape index profile.

Consequently, with this updated set of information obtained from the in-situ images, the novel way of classification of sintering proposed in Venkatesh *et al.* [134] based on pore shapes could be expanded from the previously defined 2 stages. A transition step could be integrated in between the cup-like shaped initial stage and the cap-like shaped final stage. This endorses the classical understanding (**Figure 66**) of sintering - the formation of closed porosity with an opposite curvature towards the end of sintering with regard to the pore curvature in the initial stage, together with an intermediate stage constituting a network of pore connectivity.

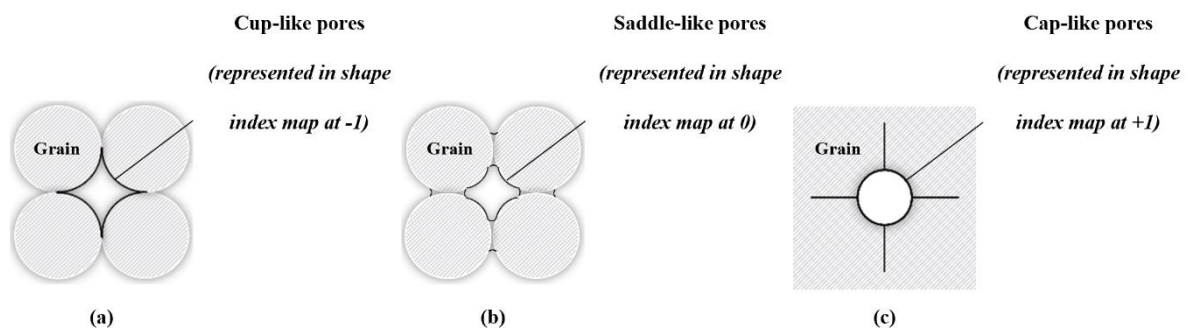


Figure 66. Representation of pore evolution during the sintering process from (a) the initial cup-like pores to (c) the final cap-like pores, including an (b) intermediate transition step with saddle-like pores.

4.4 Conclusion

This paper showcases a first-of-its-kind in-situ nano-tomography experiment exploring the ceramic sintering process at high temperature and at the particle length-scale. The experiment was conducted using the phase contrast X-ray nano-holotomography technique at the European Synchrotron Radiation Facility (ESRF). A custom-made high temperature furnace, built for the purpose, proved fit enough to operate inside the synchrotron hutch for the entire duration of the experiments.

We chose a model alumina powder system for the studies, and the high resolution of 25 nm attained allowed us to capture the collective behavior of the particles at different time intervals during the sintering process. Even though the powder system is rather simple compared to commonly used industrial powders, it is still complex and heterogenous as the local observations demonstrate.

Analysis on several key sintering parameters complemented by a thorough local assessment of the microstructure were attempted upon, using the 3D rendered data.

The parameter study included the progress of the size of the grains and the pores, and the inter-particle neck growth over time. Local examination revealed some uncommon phenomena, such as particle coarsening, at the early stages of sintering, which is usually a highlight of the latter stages of sintering. It was also possible to delve into critical unresolved aspects like particle shape evolution. Two indicators viz. sphericity and smoothness were used to describe the shape of the grains and their further advancements. Considering these shape effects and/or incorporating realistic grain shape behavior obtained by in-situ images should greatly enhance the quality of the simulation models. Underlying factors for each of these behaviors is reflected upon at the end of the respective sections.

Furthermore, the prospects of monitoring of the pore-interface curvature at different time-steps were exploited to classify the stages of sintering based on the shapes of the curvatures attained - two clearly distant stages corresponding to the pore shapes, with a transient step in between.

Expanding the scope of this research, a continuous in-situ examination at an even higher resolution could bring in more revelations. Concentration could be wholly directed, say, on the neck contact area to observe and track the mass transport phenomena. This could improve our understanding on the various diffusion mechanisms and could be incorporated into the existing models by integrating realistic parameters. A detailed study on the evolution of the shape of the necks should be possible as well.

Also, incorporating the latter stages of sintering, especially beyond 90% density, could provide 3D insights on a number of phenomena, such as the interaction between pores and grain boundaries that move as a result of grain growth, 3D visualization of pore closure transition, pore shrinkage during grain growth or the inability to do so, attachments of the pores to the grain boundary or their separation, pore annihilation, distortion in the pore shapes over time etc.

Nonetheless, this experiment is a significant step forward in understanding the underlying phenomena of ceramic sintering and can serve as a framework for future studies in this research area. Efforts are now being made to serve the obtained in-situ data as an input to one of the improved DEM models developed by the research group [110].

CHAPTER-5

TOWARDS A MORE COMPLEX CERAMIC POWDER SYSTEM

This chapter builds on the successful in-situ observation of **Chapter 4** and applies it to a less explored aspect of *constrained sintering* in an agglomerated nano-sized powder system. This chapter meets the third and final objective of the PhD thesis and is written in the form of a technical paper. Some minor revisions are needed before submitting it to the journal of Acta Materialia. The title is thought of to be on the lines of, '*In-situ X-ray nano-tomography investigation of the sintering of a complex ceramic powder system*'.

As described in the **chapters 3** and **4**, using the ESRF nano-analysis beamline's resolutions and scan periods, micron-sized alumina powders have been imaged in 3D throughout sintering.

For the sake of completion, it was deemed necessary to analyze another type of ceramic powder, more commonly used, and consisting of particles with a size of a few hundreds of nanometers. In this subsequent chapter, therefore, we will use the procedure as in **Chapter 4** for an in-situ observation of agglomerated sub-micronic zinc oxide powder compacts that exhibit inter-agglomerate pores. Additionally, 20% by volume of alumina particles of a relatively bigger size (which are supposed to be inert during sintering) are inserted into the ZnO mixture, setting up a constrained system.

The expertise gathered from earlier in-situ experiments is put into use, and the ESRF nano-analysis beamline's own furnace is employed for the same. The sintering behavior of the constrained system is examined in-situ at different temperatures.

These experiments provided us with 3D images obtained by in-situ X-ray nano-tomography with industrial sub-micronic ceramic powders. It is an outstanding step forward compared to the post-mortem and in-situ images acquired for the model powder systems of alumina in **Chapter 3** and **4**.

Tracking the changes in the inter-agglomerate pores during sintering, which are crucial to the characteristics of sintered ceramic components, was possible. The 3D images also revealed the adverse effects of constraints, such as crack formation. The chapter establishes a method for

investigating constrained sintering in more detail, opening up new possibilities for further research.

Abstract

In the framework of constrained sintering, the behavior of a complex ceramic powder system with multi-heterogeneities has been investigated. This powder system comprises inherent imperfections as well as rigid inclusions that act as constraints to densification. The sintering process of the system was monitored by in-situ X-ray nano-tomography at the European Synchrotron Radiation Facility (ESRF). This technique enables three-dimensional (3D) imaging of the microstructure with a voxel size of 25 nm. The images obtained reveal the distribution of imperfections in the powder system, such as particle aggregation and pore segregation in and around them. The subsequent in-situ evaluations show the evolution of the microstructure in the presence of the inclusions. The study addresses the questions pertaining to the effect of the added constraints, the consequent crack generation and their implication on the final densification of the material.

5.1 Introduction

One of the current trends in ceramic processing is the usage of fine nanopowders, which have attracted growing interest due to their superior properties and functionalities. An intrinsic feature of nanopowders, however, is the presence of inhomogeneities at various stages of powder preparation and compaction. Particle features (shape, size distribution, agglomeration, defects) arising from the synthesis method, the forming conditions etc. can all contribute to these inhomogeneities. These inhomogeneities strongly affect the sintering behavior and the quality and performance of the final product. To overcome these concerns, it is essential to have a thorough understanding of the microstructural evolution and the mechanisms involved in the inhomogeneous sintering of nanopowders.

Several studies have investigated these topics and reported various observations and recommendations. For example, inhomogeneities, according to Exner [144], can appear as voids, as regions of non-uniform particle packing, and as agglomerates. Dynys *et al.* [145] confirmed that the densification rate decreases with increasing agglomerate content and provided a model to describe the densification kinetics. Lange [146] reported on the poor sinterability of agglomerated powder systems. Rhodes [147] emphasized the need to get rid of agglomerations to achieve the full potential of fine powders. Suggestions for reducing or

eliminating inhomogeneities were stated in [148]. Furthermore, Evans [149] noted that the compact inhomogeneity must induce non-uniform sintering rates. Hsueh [150] explained that heterogeneities sinter at different rates than the host matrix and generate stresses that could lead to damage.

The complexity of the problem increases further when dealing with multicomponent systems, with high technological importance - such as composites, layered structures and inclusion-added scenarios. Such systems undergo *constrained sintering* with mismatched shrinkage behavior [48]. Bordia *et al.* [1] provided a comprehensive review of the mechanisms and models for constrained sintering, as well as discussed the practical problems and applications of complex ceramic systems. They highlighted the need for improved understanding and control of the microstructural evolution and stress development during sintering with constraints.

However, most of the existing literature on this topic lacks high-resolution experimental images of the microstructural evolution during sintering. The studies are limited to low-resolution and/or ex-situ observations, which are unable to capture the dynamic changes in the microstructure brought on by the presence of constraints. Weiser *et al.* [151] studied the impact of inert particulates on the sintering kinetics of ceramic powders. They found that the presence of non-sintering inclusions reduced the densification rate of the ceramic matrix. Similar behavior was seen with zinc oxide powder compacts containing silicon carbide (SiC) particles in [152]. Lately, Okuma *et al.*, using synchrotron X-ray nano-tomography in their successive works, managed to capture the three-dimensional (3D) morphology of the defects in ceramic sintering and the overall evolution in multi-layer ceramic capacitors [51], [133]. Likewise, more experimental evidence in this regard could in fact help optimize the sintering of ceramic nanopowders with constraints. In their review article, Green *et al.* [153] indeed hypothesized that future advances in in-situ tomography techniques would make it possible to comprehend and tackle these issues better. In line with this suggestion, we utilize the recent developments in the science of synchrotron tomography to investigate the sintering of an industrial ceramic powder system at an unprecedented resolution scale.

Our research group has recently demonstrated the feasibility of using synchrotron X-ray nano-tomography (nano-CT) with a voxel size as low as 25 nm to observe the sintering of ceramic powders at high temperatures [134], [154]. We applied this technique to a model alumina

powder system and obtained successful post-mortem and in-situ observations of the densification and grain growth phenomena.

Here, we extend the nano-CT application to a ceramic system that is more complex and realistic, consisting of a ZnO nanopowder with inherent inhomogeneities. The sintering behavior of the powder system is monitored up to 1000°C, with and without inert alumina inclusions added into the ZnO matrix. The effect of the added inclusions on the ZnO microstructure and on the sintering behavior overall is explored. Qualitative descriptions of each stage of the in-situ observation are provided and the assertions are supported by clear visualizations.

5.2 Materials and Methods

Powder system and sample preparation

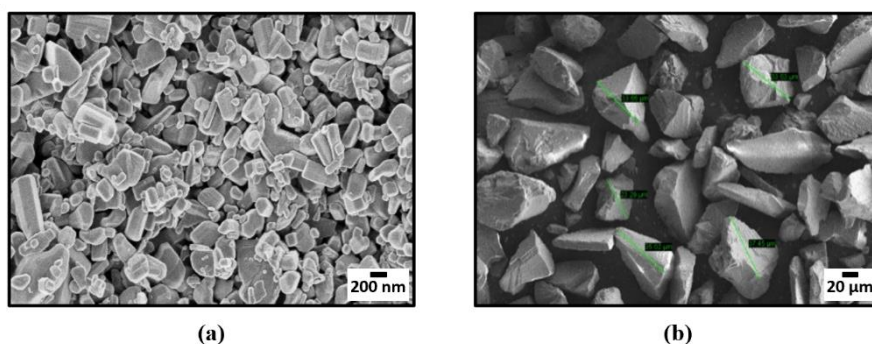


Figure 67. SEM observation of (a) ZnO powder with particle sizes of around 200 nm and (b) Al₂O₃ powder of around 22 μm, respectively.

The two powders employed in this study are a sub-micronic zinc oxide (ZnO) powder (average size of 200 nm from Carlo ERBA) and an alumina (Al₂O₃) powder (average size of 22 μm). The scanning electron microscopy (SEM) images of both are given in **Figure 67**. ZnO nanoparticles comprise a variety of shapes such as prismatic, cuboid-like, thin rod-like, and other irregular profiles, while the Al₂O₃ particles are angular, with sharp corners and jagged edges.

For the experiments without alumina inclusions, the ZnO powder is mixed and pressed to shape uniaxially in a die under a pressure of ~60MPa. A small amount of stearic acid mixed with acetone was used as a lubricant for the die. The parameters were selected carefully to ensure that the final compact density came up to around ~52%.

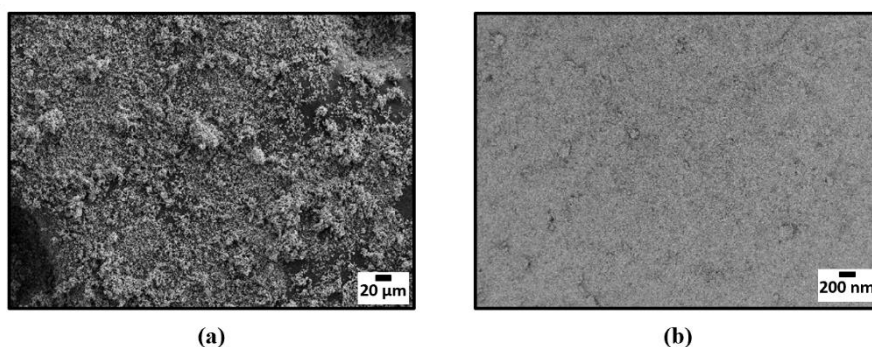


Figure 68. SEM observation of the ZnO powder (a) before and (b) after compaction.

Another SEM image, now with a lower magnification, indicates the presence of different types of entities (**Figure 68** (a)), prior to compaction in the original ZnO powder. The inherent heterogeneities are visible - nanoparticles tend to naturally stick together due to their higher surface energy and area, forming agglomerates. The compaction process (**Figure 68** (b)) reduces the average pore space, causing most of the *softer* agglomerates in the matrix to disintegrate. There are still, however, regions with larger porosity, due to the fact that the *harder* agglomerates, which are resistant to breakage, remain intact. These are referred to as *aggregates* in this study. They have a size range of up to several tens of microns. There are also other *larger elements* that might have originated from the processing route. These elements are also a few microns in size. They cannot be clearly distinguished from the aggregates with the SEM images but can be better identified by tomography images in the later sections.

For the experiments with inclusions, 20 vol % of alumina particles are mixed together with the ZnO powder. This blend is compacted following the same procedure as above. The relative density of the compacts read ~50%.

Dilatometry experiments

Preliminary dilatometry experiments were conducted in *SETARAM's SETSYS Evolution - 1750 CS* to trace the sintering behavior, with and without inclusions (**Figure 69**). With a heating rate of 5°C/min and an original relative density of ~52%, the change in shrinkage of the compact was measured as a function of time from the room temperature to 1000°C. At 1000°C, the experiment without inclusions shrunk the compact by ~16%. Final relative density calculated by the Archimedes approach read ~92%. However, with 20% alumina inclusions, following the same thermal cycle, the density attained was limited significantly (~77%), causing a

shrinkage of only ~12%. This signals that the addition of inclusions hampered the densification process. The underlying mechanisms for this drastic difference in the density and shrinkage will be deciphered later with the tomography analyses.

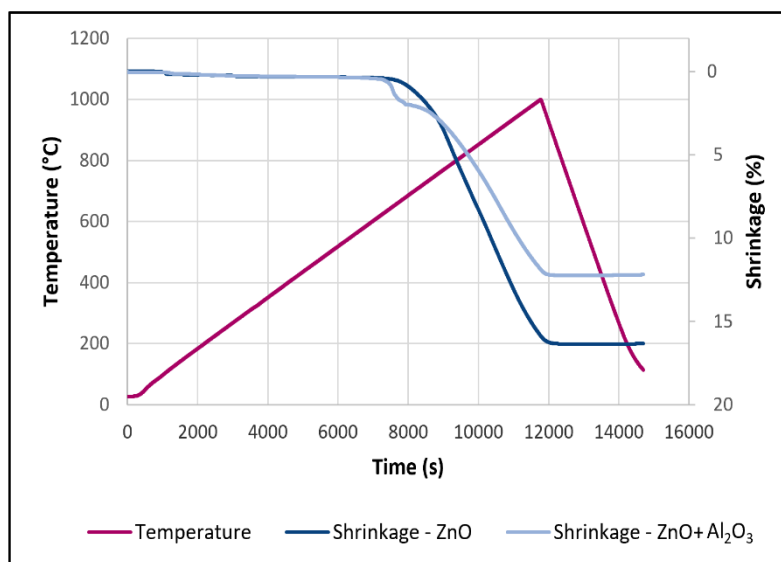


Figure 69. Dilatometry curves showing the trajectory of the shrinkage in the compact, with and without alumina inclusions.

X-ray nano-tomography experiments

For the samples without inclusions, we performed post-mortem experiments [134], by scanning the samples that have already been subjected to the sintering cycle in the dilatometer. For the sample with inclusions, interrupted in-situ experimentations were carried out inside the synchrotron hutch [154], by scanning the same region of the sample during the heat treatment, capturing the sintering evolution. We followed the same experimental set-up and procedure as described in our previous works [134] [154]. This phase-contrast technique has a proven record of attaining higher resolutions. In addition, the difference between the two ‘phases’ of ZnO and Al₂O₃ here in terms of their very different absorption coefficients could be exploited as well. For post-mortem, the sintered dilatometer compacts were broken into smaller fragments. For in-situ, the *green* compact obtained just after compaction were broken - we expect it to not introduce significant damage in the material as this compact is very brittle. The fragments are ~100 μm in diameter and ~1-2 mm in height in both the cases, suitable for further phase-contrast nano-CT experiments at the ESRF synchrotron. Holotomography (4-distance imaging), with a total of 3203 projections over a full rotation were collected using an X-ray beam with an energy of 29.1keV for each tomographic scan [63]. The resulting 3D volume of

$64*64*54 \mu\text{m}^3$ presents a voxel size of 25nm. 3D reconstructed images of the internal structure of the compacts were obtained at five different sintering temperatures: room, 800°C, 900°C, 1000°C, and 1000°C + 30 min of isothermal holding.

A built-in furnace of the ESRF with a Ni-Cr resistor, clad in an Inconel shell, was used for these real-time assessments [5]. An iterative Paganin based method with a delta over beta value of 59.7 was chosen to perform the phase retrieval of radiographs [65], and ESRF's PyHST2 software package was then used for the subsequent reconstruction, to obtain the 3D volumes of the samples [94].

5.3 Results

5.3.1 Post-mortem investigation

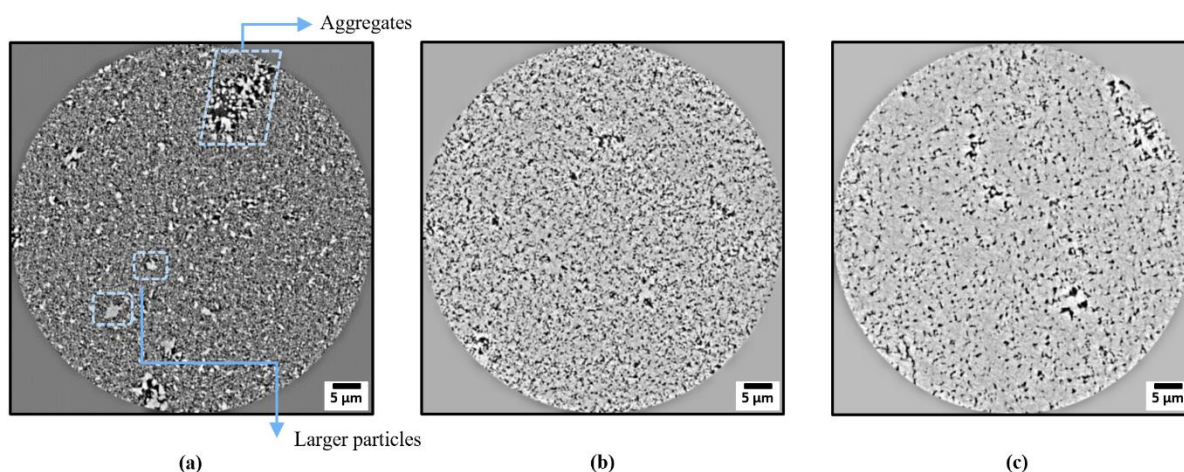


Figure 70. Cross-section slices extracted from the 3D reconstructed volumes for ZnO samples at (a) the green state, and observing post-mortem after sintering at (b) 800°C and (c) 1000°C, respectively.

First, we present the results obtained from the post-mortem nano-CT of the ZnO powder compacts performed at the ESRF. **Figure 70** (a) shows the microstructure of the ZnO powder at the green state, before sintering, and with no alumina inclusions in them. In the figure, the ZnO matrix is in shades of gray, while the black phase is porosity. The material is porous with a relative density of ~52%, as evidenced by the pore spaces in the image. The resolution of the imaging, although not effective enough to view the individual particles, is good enough to detect the inhomogeneities (spaces with higher porosity) present in the powder packing. As a consequence of the particle aggregation, the particles have a wide size distribution and some

regions have higher porosity than others. It is possible here to make a distinction between the *aggregates* and the so-called *larger ZnO particles*.

The microstructure of the compact after sintering at 800°C is depicted in **Figure 70** (b). The image shows the process of densification, together with some grain growth that has occurred during sintering, making the grains clearly distinguishable from the pores now. Nonetheless, a distribution of porosity still seems to exist. At 1000°C, in **Figure 70** (c), prevailing massive grain growth can be observed, with a much higher densification of the material. The density of the compact reaches ~92%, corresponding to the 16% shrinkage that was earlier noted via the dilatometry exercise. Two classes of porosity can be noticed, with smaller pores that have been gradually shrinking and the larger pore segregations that are visible in a few locations here and there. These three figures show more or less the expected course of action that is bound to happen during a sintering process. This is taken as a reference for the subsequent in-situ imaging carried out on the sintering of the same microstructure but with some additional larger alumina inclusions inside.

5.3.2 In-situ investigation

A global view of the powder system at the green state is displayed in **Figure 71**, obtained after the 3D reconstructions of the in-situ observations.

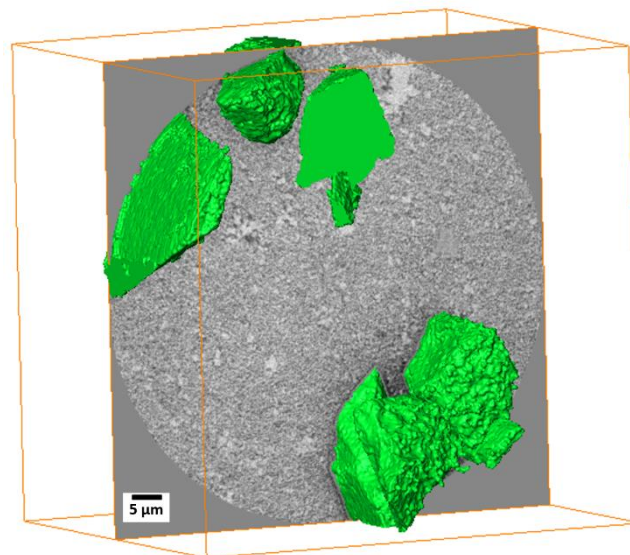


Figure 71. An overview of the material system under consideration, showing one of the slices of the image stack (64*64*54 μm³) with the ZnO matrix and the alumina inclusions in green in 3D.

From here on in this study, for the sake of convenience, the 3D image stacks are categorized into two regions based on their proximity to the added inclusions - *Region 1* referring to the areas that are far from the inclusions, and *Region 2* in the vicinity of inclusions (**Figure 72**).

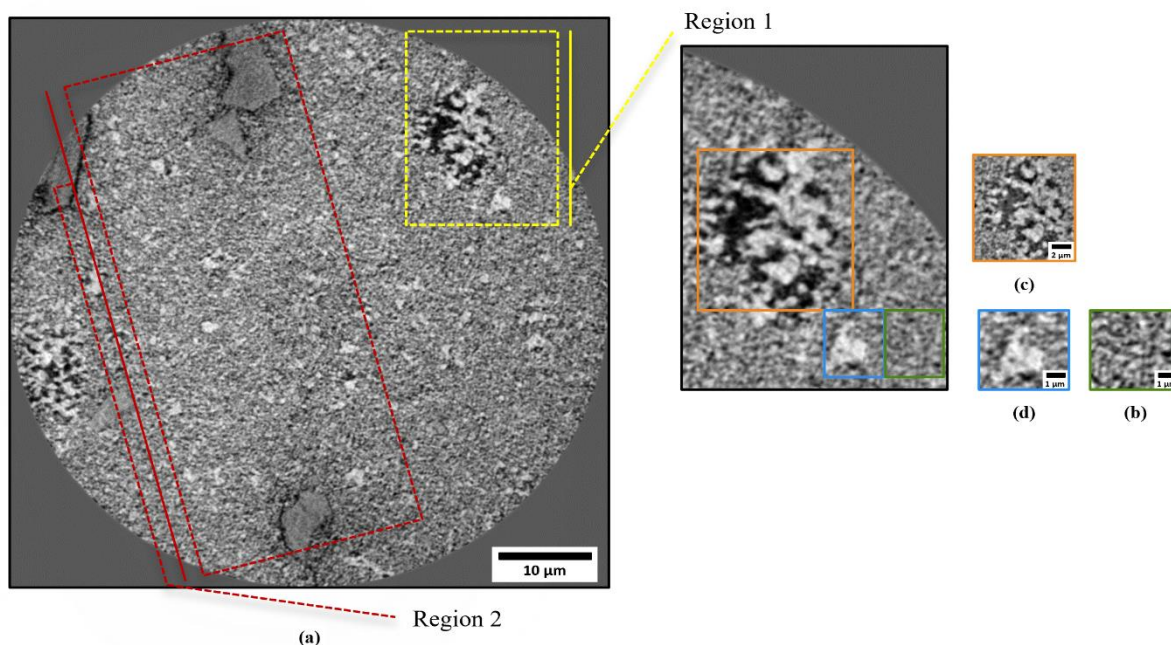


Figure 72. (a) One of the slices of the image stack (taken from mid-volume) depicting the categorization of the images into regions far from the inclusions (Region 1) and regions with the inclusions (Region 2). (b), (c), (d) show the sub-regions with no apparent inhomogeneities, larger ZnO particles and aggregates, respectively.

Microstructure evolution far from the inclusions

The idea of analyzing Region 1 separately is to check the behavior of the regions away from the influence of the inclusions, so as to regard them as regions supposedly undergoing *free sintering* and capture their evolution over time. In this context, it entails taking a look at the effect of the inhomogeneities prevalent in the ZnO matrix on the microstructure, without the added impact of the inclusions. Of course, this does not necessarily imply that the regions in question would be totally unaffected by the inclusions, but it is presumed to be minimal. They are selected based on a careful distance mapping, so that the inclusions are not in sight for a minimum number of voxels (~500) in the X and the Y-direction, and for at least 500 slices in the Z-direction.

Furthermore, Region 1 is divided into 3 more distinct sub-regions, to try and encompass the variability in the ZnO matrix – Sub-regions with only the ZnO matrix, Sub-regions with ZnO matrix and aggregates, and sub-regions with ZnO matrix and larger ZnO particles.

We compare and discuss the different sintering behaviors exhibited by these regions depending upon the presence and the type of inhomogeneities. One such representative region for each of the cases mentioned is displayed in the **Figure 72** (b) (c) (d) and taken in for the discussion below.

The in-situ observation of the sub-region 1 with only the ZnO matrix (**Figure 72** (b)) at different times shows a typical sintering behavior, as seen from **Figure 73**. Sintering in the absence of strong particle aggregation as such is expected to allow the attainment of higher densification rates than for sintering with aggregation. These sub-regions have the highest packing density in the matrix and therefore should see the most rapid densification. Likewise, the individual particles in **Figure 73** (a), with uniform and homogeneous microstructure tend to enhance the sintering progression. The grain packing appears to gradually densify from the room temperature up until 900°C, and the pores in the matrix shrink during the process (**Figure 73** (a) (b) (c)). Later, the particles increasingly merge and grow in size (**Figure 73** (d) (e)). As a likely consequence of this grain growth, pore coalescence can be noticed towards the end, especially during the period of isothermal holding (**Figure 73** (e)).

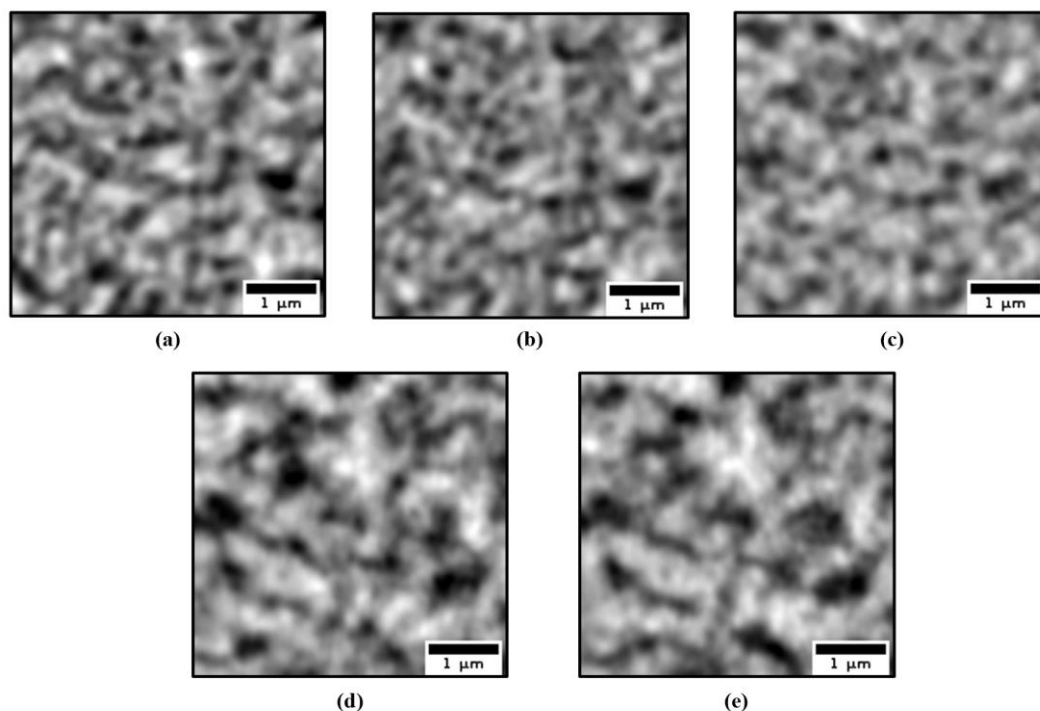


Figure 73. Follow-up of the in-situ observation of one of the sub-regions with only the 3D reconstructed ZnO matrix at (a) room temperature, (b) 800°C, (c) 900°C, (d) 1000°C, and (e) 1000°C + 30 mins of isothermal holding, respectively.

The following paragraphs discuss the sub-regions 2 in Region 1 which contribute to the non-uniformity in the powder system.

The sub-region with aggregates (**Figure 72 (c)**) includes strongly bonded clusters of smaller particles that resist disintegration during powder compaction. These aggregates create heterogeneous packing in the green body, which leads to differential sintering and distortion of the compact [155]. Moreover, the lower packing density here has an adverse effect on the *sinterability* and limits the density of the final product.

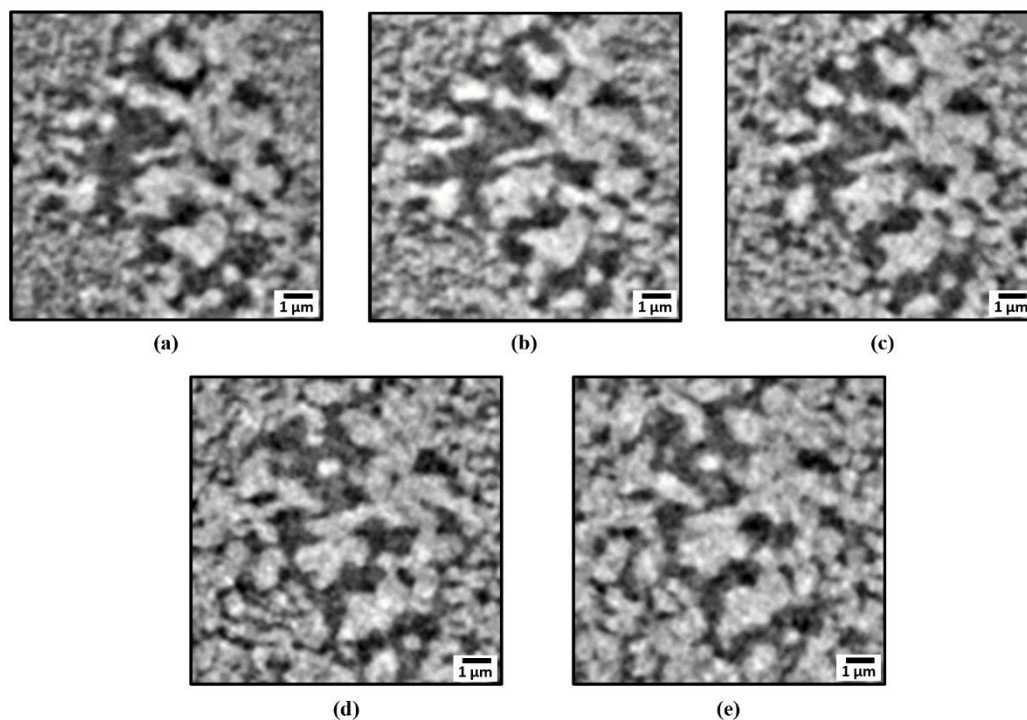


Figure 74. Follow-up of the in-situ observation of one of the sub-regions with aggregates in the 3D reconstructed ZnO matrix at (a) room temperature, (b) 800°C, (c) 900°C, (d) 1000°C, and (e) 1000°C + 30 mins of isothermal holding, respectively.

The **Figure 74** above shows the in-situ observation of the aggregates' behavior during sintering. It shows a starkly different conduct from the previous sub-region. Initially, in **Figure 74 (a)**, the aggregates are poorly connected to the matrix particles and are surrounded by pores. Further, throughout the sintering process, the aggregates change slightly over time, but they do not break or deform significantly. The pores around remain mostly stable and intact. However, all around the aggregates, we see grain growth occurring in the matrix over time.

Additionally, the original powder contains some ZnO particles that are larger and more irregular than the rest of the matrix. They are considered in the sub-region 3 (**Figure 72 (d)**).

These particles do not break on compaction and are anticipated to show complex and varied sintering behavior. Salehi *et al.* [156] reported that such larger particles have a negative effect on the packing density and the homogeneity of the matrix.

The larger particles also possess isolated large pores in and around them (**Figure 75** (a)). These *heteropores* could be attributed to the poor packing of the smaller particles around the larger ones during compaction, as reported by Jonghe *et al.* [157]. They are not easily eliminated during sintering, as they are weakly connected to the surrounding matrix and have a low driving force for sintering [158]. Porras *et al.* [159] studied the stability and redistribution of such related pores and found that they can exhibit complex and different behaviors depending on their location and size.

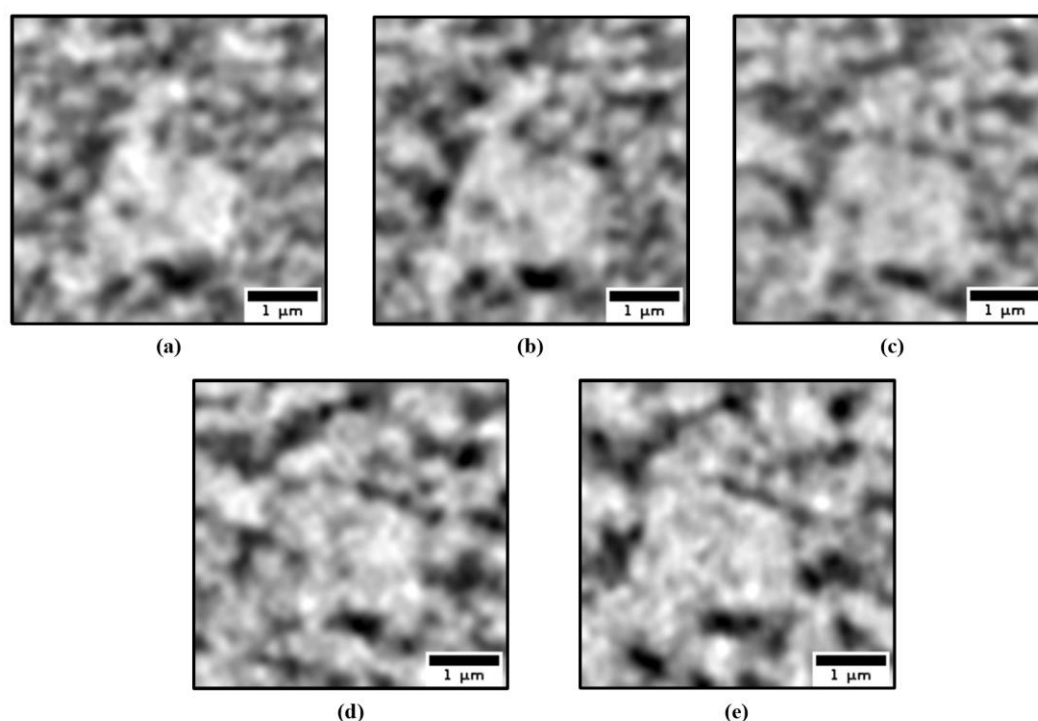


Figure 75. Follow-up of the in-situ observation of one of the sub-regions with larger particles in the 3D reconstructed ZnO matrix at (a) room temperature, (b) 800°C, (c) 900°C, (d) 1000°C, and (e) 1000°C + 30 mins of isothermal holding, respectively.

During sintering, as seen from the set of images above (**Figure 75**), the larger particles behave more rigidly than the aggregates. They retain their core shape, but merge with other grains over time, forming an even larger version of the same. The pore evolution (from **Figure 75** (b) onwards) is complex and varied along the surface of the larger particles. Some pores around the particles stay the same, while others increase in size due to the coalescence of smaller pores around them. In addition, we find that some of the larger particles contained *intra-pores* that

vanished during sintering, indicating a densification process within the particles. This is because the smaller pores have a higher surface area and curvature, which makes them more prone to densification and shrinkage. The larger pores, on the other hand, have a lower specific surface area and curvature, which makes them more resistant to the same [108], [111].

On the whole, the sintering characteristics of the compact would deteriorate due to the low-sintering characteristics of the aggregates and the much coarser particles, and the slow shrinkage of the larger pores, resulting in a more porous and a weaker product. The imperfections here in the in-situ observation do not appear to collapse easily, but instead persist and create further complications. This behavior is in contrast to the post-mortem image sequence in **Figure 70**. No significant densification is observed in the sub-regions with the imperfections, indicating that it can contribute to the hindering of the sintering process of the overall matrix, and thereby reduce the strength of the sintered material. This essentially suggests the wide-ranging impact of the inclusions (discussed further in the subsequent section) even at distant locations from their positions.

Microstructure evolution in the vicinity of the inclusions

Moving on now to the second region in the study - Region 2, and focusing our attention on to the role of the alumina inclusions in the ZnO matrix. The region contains a network of deliberately introduced much coarser alumina particles (average size of 22 μm), into the matrix ((**Figure 71**) (**Figure 72 (a)**)), setting up a constrained sintering framework. This is likely to create a higher degree of inhomogeneity in the microstructure, the extent of which is analyzed in this section.

The alumina particles behave as rigid inert inclusions, as they do not deform or react with the surrounding ZnO matrix. Poor packing of the ZnO particles around the inclusions generate voids adjacent to them from the get-go (**Figure 76 (a)**). In addition to poor initial packing, the action of unloading after die pressing could also possibly be responsible for the defects around the inclusions. These voids at the matrix-inclusion interface, referred to by many terms in the literature, such as circumferential voids, peripheral pores etc. are responsible for the large suppression in the densification rate during the initial stages of sintering [160]–[162].

The formation of initial voids next to the inclusions is a common feature with respect to all the inclusions here in the system. As illustrated in **Figure 76 (a)** onwards, over time, as sintering progresses, the voids become thicker and more pronounced, creating an extreme density variation around the interface. Notably, towards the latter stages of sintering, at around 900°C

(Figure 76 (c)), these voids appear to be acting as a source of crack initiation. This is further clearly visible from 1000°C onwards (Figure 76 (d)). In the neighboring matrix, significant grain growth can be seen over the course of sintering.

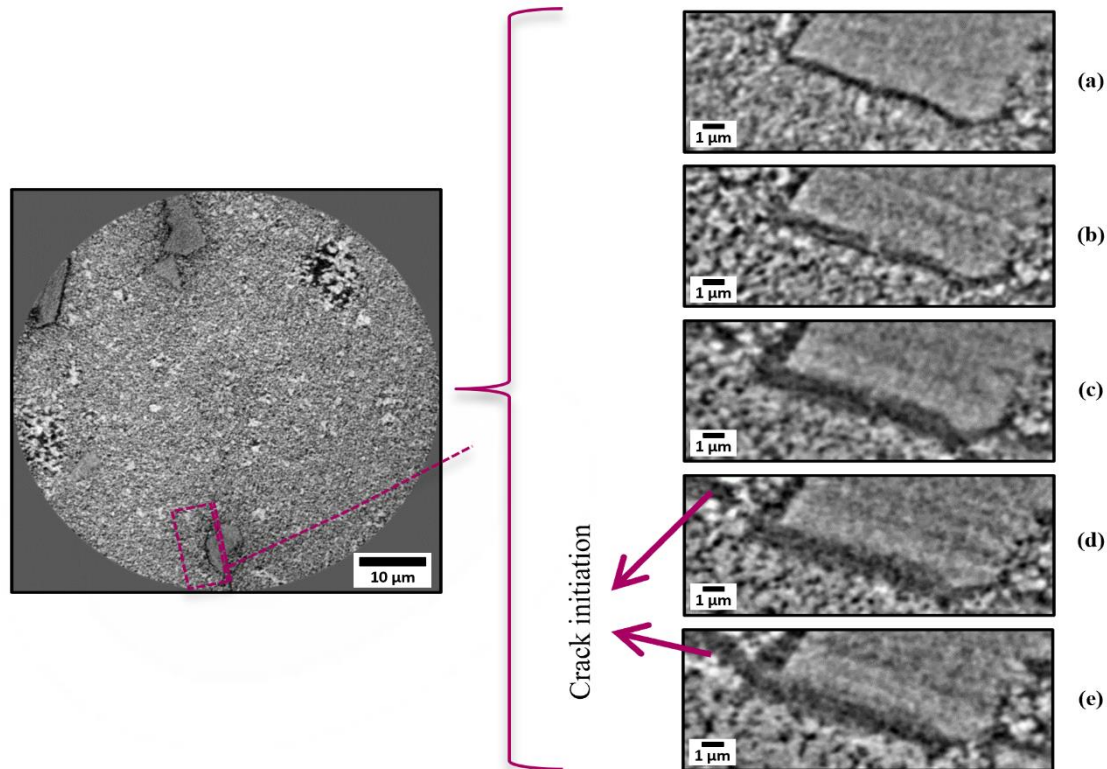


Figure 76. Follow-up of the voids generated at the matrix-inclusion interface at (a) room temperature, (b) 800°C, (c) 900°C, (d) 1000°C, and (e) 1000°C + 30 mins of isothermal holding, respectively.

To know more on these crack-like defects, if they further open during sintering or just exist as imperfections, a wider view of the region is considered here. Figure 77 is a tracker of the cracks taken from cross-section visualizations at various sintering temperatures. We find that the voids at the matrix-inclusion interface in fact act as pre-existing flaws. Extent of the cracks increases at every time-step, both in terms of their magnitude and severity.

As compiled in Bordia *et al.* [1] and as observed in Lange *et al.*'s works [163], [164] in the context of constrained sintering, the damage here indeed begins in the early stages of densification and near pre-existing defects/voids.

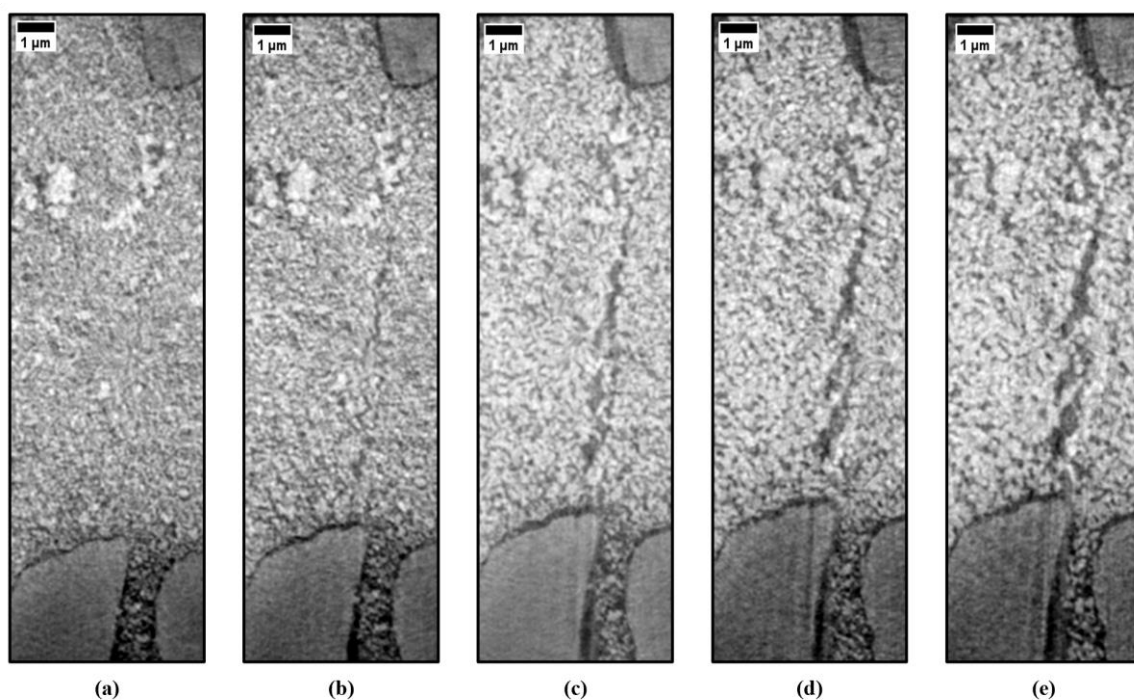


Figure 77. Follow-up of the crack initiation and propagation in between the inclusions at (a) room temperature, (b) 800°C, (c) 900°C, (d) 1000°C, and (e) 1000°C + 30 mins of isothermal holding, respectively.

The reasons for the crack visualizations are anticipated to be the stresses generated as a result of the inclusions added to the system, as remarked in a few theoretical approaches [165], [166] and experimental studies [160], [167]. These stresses have been given an overall term ‘back stresses’ by Tuan *et al.* [161] and they are supposed to exist in the matrix, in the inclusions, and at the inclusion-matrix interface. According to them, these internal stresses can arise from an external constraint or from the differential densification due to inhomogeneities. We can rest assured that in the present study, the main source of internal stresses is the constraint imposed in terms of inclusions.

Our notion is that the presence of inclusions prevents the matrix regions away from the inclusions (described in the previous section) from sintering uniformly. The rigid nature of the inclusions makes these regions undergo a tensile stress, which in turn hinders their shrinkage. Simultaneously, local stress concentrations develop, especially at the periphery of the inclusions. This eventually has the potential to introduce and propagate crack-like defects, as demonstrated in **Figure 77**. In all probability, these cracks would act as strength-limiting flaws and cause irreversible structural damage, proving fatal for the properties of the sintered parts.

Furthermore, it could also be inferred from **Figure 77** that the cracks, rather than being a mere linkage of pores, have a well-defined path. They also cause a separation of initially sintered grains in some cases. Interestingly, the cracks tend to propagate from one inclusion to another, as seen from **Figure 77** (b) onwards. All the cracks in the entire volume were checked for the possible routes of propagation. This feature of crack initiation and propagation was observed consistently, and once initiated, they propagate through the 3D network of these inclusions. The impact of the inclusions becomes progressively more critical as the densification proceeds (**Figure 77** (d) (e)). However, the relative significance of the inclusion volume fraction, the inclusion size and of other processing conditions are beyond the scope of this study.

Overall, it is safe to declare that, together with other inhomogeneities, the cracks due to the constraints are major contributors to the significantly lesser shrinkage observed in the powder system. This justifies the lesser final densification (~77%) attained in the dilatometry experiments for the inclusion-added system earlier. Also, the aggregates and the larger ZnO particles behave rigidly, yes, but their impact is marginal in comparison to the effect of the rigidity of the alumina inclusions.

It is also to be noted that we attempted to conduct a quantitative analysis on the sintering evolution. However, the resolution of the images was not sufficient enough to detect the individual nanoparticles accurately. Image analyses, for instance, on features such as the density variations at different regions; evolution of pores and voids in terms of their thickness and volume; 3D rendering of the cracks and their volume evaluation etc. were tried upon, but the results were not found to be precise and reliable. It was therefore decided to focus on a more qualitative account of the trends observed.

5.4 Conclusion

The sintering behavior of a ZnO-based powder compact with several heterogeneities has been visualized using nano-scale (25nm) imaging at the ESRF synchrotron.

The microstructure of the powder compact was compared with and without inclusions - by visualizing a post-mortem sample without inclusions and introducing the inclusions during the in-situ observation.

Post-mortem imaging at this scale was good enough to perceive the heterogeneities of the system and its evolution during sintering. The heterogeneities get effectively minimized over the course of sintering, leading to densification in the compact.

When additional larger alumina inclusions were added into the matrix, with in-situ imaging, it is found out that these inclusions have a clear impact on the sintering process. They have a significant effect on the microstructure not only in their immediate vicinity, but also far away from them. Real-time assessments of the system show the behavior of the inhomogeneities in the presence of inclusions such as the aggregates and the larger ZnO particles in the matrix, formation and persistence of large pores, and the ensuing spatial density variations.

Additionally, the inclusion is observed to be acting as a rigid constraint inducing damage around it, which spreads into the surrounding matrix during sintering. The voids which were initially present adjacent to the inclusions, were found to later manifest as cracks during sintering. Crack initiation and their progression afterwards were seen to be from one inclusion to another. These factors were seen to influence and lower the overall densification and shrinkage of the material system. The cracks are imagined to compromise the structural integrity and the properties of the sintered components.

Given resolution-related improvements in the future, this work establishes a solid basis for a systematic quantitative study on the sintering of such nanoscale powders, both with or without constraints. Future works could make use of the nano-holotomography imaging system and the resolution attained to check the retarding effect of the inclusions in terms of their size, shape, number and spacing on the sintering kinetics and microstructure. Optimal sintering conditions for a given set of inclusions could be identified, and the possible scenarios if and when the added inclusions could be detrimental for the sintering process may be explored.

CHAPTER-6

COMPARISON WITH DISCRETE ELEMENT SIMULATION

This final chapter presents a preliminary comparative analysis of the key results derived from in-situ measurements on alumina sintering in **Chapter 4** and a novel *DEM model* recently developed by our research group. This chapter is still under development and has the potential to be published as a full-fledged technical paper. Possible titles for the paper are, ‘*Consolidation and grain growth in sintering of alumina powder: In-situ X-ray nanotomography and DEM simulation results*’ or ‘*Comparison of discrete element simulation of ceramic powder sintering including grain growth with the results of in-situ X-ray nanotomography experiments*’.

6.1 Introduction

Modeling is an important tool for understanding and optimizing the process of sintering for different applications. Consistent efforts have been on to develop accurate and reliable models that can foresee the microstructural evolution and the overall sintering behavior. Different models have been developed at different scales, ranging from atomistic to macroscopic scales. At the grain scale, discrete element method (DEM) is a numerical method that has been used to model various aspects of sintering, especially the consolidation and the densification processes. The technique can simulate the sintering behavior of a large collection of grains while taking into consideration the individual behavior of the particles and their interactions. Each grain is represented as a discrete element with certain properties, and its positions, interactions and deformations are tracked by means of solid mechanics and contact laws.

Martin *et al.* [168] and Henrich *et al.* [169] were among the first ones to demonstrate the potential of DEM to forecast sintering behavior. Martin *et al.* [168] used DEM to model sintering of metallic powders and compared the simulated outcomes with experimental data. Henrich *et al.* [169] used DEM to study the influence of rearrangement during sintering and its impact on microstructural evolution. Several studies later on have come up with DEM simulations and have used tomography facilities to perform in-situ or ex-situ measurements of

sintering processes in order to make comparisons. For instance, Olmos *et al.* [39] compared the results of DEM with those of X-ray microtomography to study the sintering of copper particles. Martin *et al.* [170] validated their DEM model of sintering using an in-situ X-ray microtomography analysis of the sintering of NaCl powder. Other authors, like Lichtner *et al.* [171] investigated the anisotropic sintering behavior of freeze-cast ceramics by discrete-element simulations and optical dilatometry. Roussel *et al.* [172] applied discrete simulations on X-ray nano-tomography images to examine the strength of porous ceramics.

None of the sintering-related works above, though, considered realistic grain growth in their models. This is an important factor affecting the final microstructure and properties of sintered ceramics. However, lately, Paredes *et al.* [110] accounted for the effects of grain boundary diffusion and migration in their model. They proposed a grain growth model coupled with a densification model for ceramic sintering, based on DEM simulations on large packings. This model predicts the sintering trajectory, as in, the evolution of density and grain size in solid state sintering, and showed improved relevancy in the early and intermediate stages of sintering. Performance of this model has been assessed on the sintering behavior of conventional as well as nanoscale powders to acquire insights into the sintering mechanisms [110] [173]. This DEM model considered grain boundary diffusivity as the main parameter for densification, and surface diffusivity and grain boundary mobility as the main parameters for grain growth. These effective diffusivities and mobilities depend on the powder composition and their purity.

A more comprehensive comparison of this model is now possible, thanks to the 3D imaging of ceramic sintering, made possible with advanced synchrotron X-ray nano-tomography techniques. Sintering progression of ceramic powders, both by post-mortem and in-situ observations at the particle-length scale has been reported recently [134] and are described in **Chapter 3** and **Chapter 4**.

This chapter is dedicated to integrate the findings of Paredes *et al.* [110] and Venkatesh *et al.* [134]. In-situ X-ray nano-tomography analysis of the sintering of alumina powders in Venkatesh *et al.* [134] served as the basis for the validation of Paredes' DEM model of sintering. The DEM model was first calibrated according to the input parameters of the post-mortem experiments (**Chapter 3**). Then, the calibrated DEM model was run in accordance with the in-situ experiments of **Chapter 4**, to compare and review the similarities and the differences. We evaluate different key sintering variables and suggest that such collaborative

approaches could throw light on fine-tuning the processing conditions leading to a better control of ceramic sintering.

6.2 Model description

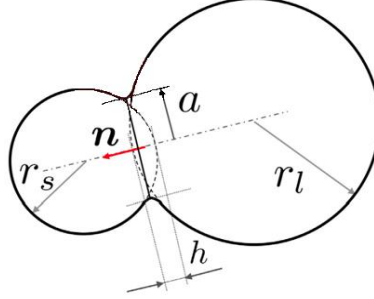


Figure 78. Schematic of the contact between two spherical particles of unequal sizes with radii r_s and r_l .

The proposed DEM model is a coupled solid-state sintering and grain growth model that can simulate large packings of particles with realistic particle size distributions. The model uses refined contact laws to account for consolidation and densification. Derived from the models of Bouvard and McMeeking [24] and of Pan *et al.* [25], the normal force N between two particles with radii r_s and r_l is defined as:
$$N = -\frac{\pi a^4}{\left(1+\frac{r_s}{r_l}\right)\beta\Delta_{GB}}\frac{dh}{dt} + \frac{\alpha}{\beta}\pi r_l \gamma_s$$

with surface energy γ_s and a grain boundary diffusion-related term $\Delta_{GB} = \frac{\Omega}{K_b t} D_{GB} \delta_{GB}$, where $D_{GB} = D_{0GB} \exp\left(-\frac{Q_{GB}}{RT}\right)$ is the diffusion coefficient with the activation energy Q_{GB} . Geometrical parameters h , a and n are the indentation, the contact radius and the normal vector respectively, as illustrated in **Figure 78**.

The mass transfer between the particles to account for grain growth is driven by surface diffusion (S) and grain boundary (GB) migration. The two terms with the corresponding diffusion coefficient D_s and the grain boundary mobility M_{GB} , following the conditions in the

picture above (**Figure 78**), take the form as:
$$\left(\frac{dV_{LS}}{dt}\right)_S = -2 \frac{D_s}{K_b T} \gamma_s \Omega \frac{\frac{1}{r_l} \frac{1}{r_s}}{r_l + r_s - \delta} [\pi(a + \delta_s)^2 - \pi a^2]$$

and
$$\left(\frac{dV_{LS}}{dt}\right)_{GBM} = -2 M_{GB} \gamma_{GB} \left(\frac{1}{r_l} - \frac{1}{r_s}\right) [\pi a^2]$$

The volume balance at the contact points is maintained as per by these equations. The model's comprehensive approach will be put to test with the first-ever X-ray nano-tomography experimental data of ceramic sintering carried out at the particle-length scale, using the in-house developed DEM software dp3D [168].

For detailed description of the model and the parameters involved, please refer to the original source by Paredes *et al.* [110], [173].

6.3 Results

6.3.1 Consolidation - Alumina 1.3 μm

Calibration of DEM model with post-mortem experimental data

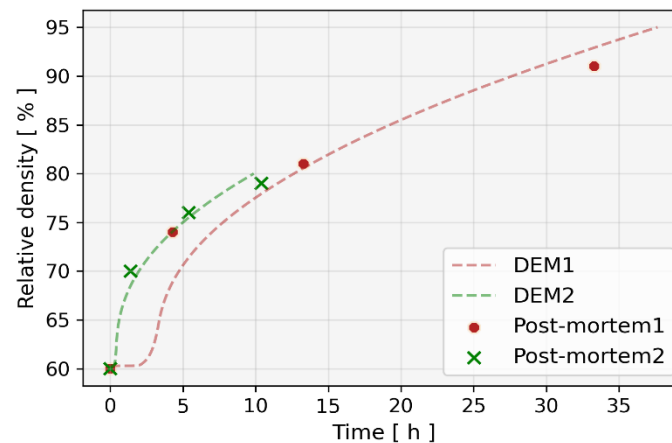


Figure 79. Correlation between the density of the sintered compact measured by the Archimedes approach for the sintering of Al 1.3 μm at 5°C/min (Post-mortem1) and 40°C/min (Post-mortem2) respectively, and the profile obtained with the corresponding DEM simulation.

First up, the DEM model was calibrated with the post-mortem experimental data for alumina 1.3 μm . As detailed in **chapter 2** and **chapter 3**, the sintering was performed with heating rates of 5°C/min and 40°C/min, from room temperature to various times at the isothermal holding of 1500°C.

Initial considerations for the simulation were set in accordance with the experimental conditions: 1.33 μm diameter alumina particles with an effective standard deviation of 0.19 μm in the distribution, with initial powder compact density of 60%, and with the same two thermal cycle profiles, with an exception of 500°C as the starting point. The end conditions for the simulation were set at 80% and 90% of density for the experiments with 5°C/min and 40°C/min heating rates, respectively.

Different simulations were run by varying the parameters in the DEM model to obtain the best possible match with the density values of the post-mortem experiments at different time intervals at 1500°C. A diffusivity pre-factor value of 0.13e-08 m^2/s with an activation energy

of 475 KJ/mol (taken from literature [107]) was found to give a good agreement between the simulated and experimental results.

The corresponding density points of the simulations are plotted with the ones obtained for the experiments below in **Figure 79**. Relative density in the case of the experiments, or *Practical* relative density, is the ratio of the weight density at a particular temperature to its value at room temperature.

The agreement in the density trajectory indicates that the calibration method was effective enough to run further sintering simulations on the chosen powder.

DEM simulation and comparison with in-situ experimental data

The reliability of the calibrated DEM model was checked by evaluating the results it produced for the evolution of key sintering parameters viz. density, co-ordination number, and inter-particle neck growth. Data obtained by in-situ experiments on alumina 1.3 μm were used for comparison. In contrast to the post-mortem experiments, in-situ offered direct observation of the same sample with more time-steps. The heating cycle in the experiments consisted of a ramp at a rapid rate from the room temperature to 1500°C, followed by an isothermal holding. The details are in **Chapter 4**.

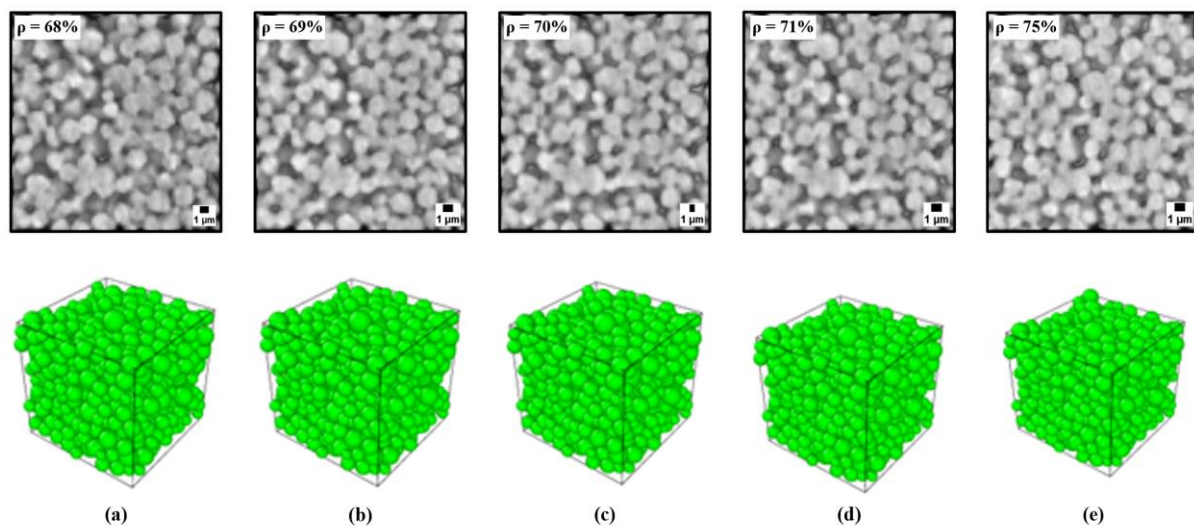


Figure 80. 3D follow-up of a cropped section of the in-situ observation of the alumina Al 1.3 μm and the corresponding 3D renderings of the DEM simulation below (in green), after (a) 1 hour, (b) 1.5 hours (c) 2 hours, (d) 3 hours, and (e) 5 hours of sintering at 1500°C respectively. ρ is the *true* relative density (fraction of solid phase).

Using the calibrated values for the parameters - diffusivity pre-factor of 0.13E-08 m^2/s and an activation energy of diffusivity of 475 KJ/mol, DEM simulation was run in line with the in-

situ experiments. A cubic ROI of 520*3 voxels, each side with a length of 13 μm was considered for the powder packing. This matches with the size of the many cropped image stacks taken for the quantitative analysis from the 3D in-situ data. The sintering process was simulated by keeping the temperature fixed at 1500°C in dp3D until it reached ~80%, which was the end condition in the case of the in-situ experiment (~75% density).

The 3D visualizations of the DEM simulations are displayed below their counterparts from the in-situ observations in **Figure 80**.

Density

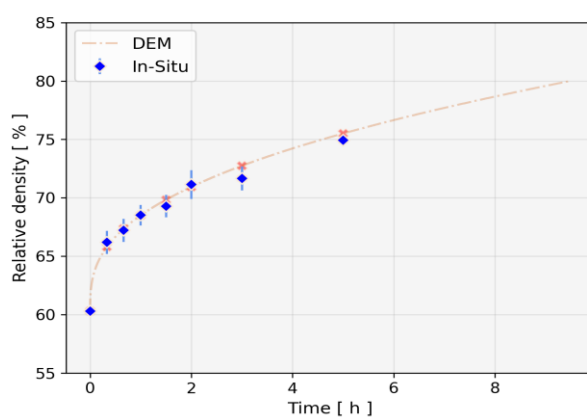


Figure 81. Comparison of *true* relative density (fraction of solid phase) as a function of dwell time for alumina Al 1.3 μm sintered and observed in-situ, along with the corresponding DEM simulation.

The graph of density change as a function of time in **Figure 81** showed a good match between the experimental data and the DEM simulations along all the time-steps considered. This reaffirms the validity of the calibration method. Both the in-situ and the DEM data reached a similar density level (around 75%) after sintering at 1500°C for ~5 hours. The results also show that the DEM simulations, although they consider spherical particles, are consistent with the in-situ experiments.

Coordination number

The co-ordination number, i.e. the average number of contacts per particle, serves as an important tracker of the sintering behavior. Its variation with time, plotted in **Figure 82**, showed significant differences in the values between in-situ and DEM. The coordination numbers in the in-situ experiments remained higher (with a difference of around 0.5) than those in DEM at all times. This could be attributed to the different assumptions/factors in play:

- In in-situ experiments, the non-spherical shape of the particles allowed more possibilities of contact with neighboring particles than the spherical ones in DEM. The particle co-ordination may have also been impacted by the particle rearrangement phenomenon that was initially noticed (ref. **Chapter 4**). Moreover, some particles may have coalesced as the sintering progressed, which would have had an effect on the particle number and, in turn, the co-ordination number, over time.

- In DEM simulations, the assumed spherical shape of the particles limited the contact possibilities with the neighbors. Moreover, since grain growth was not considered, the particle number remained constant during sintering.

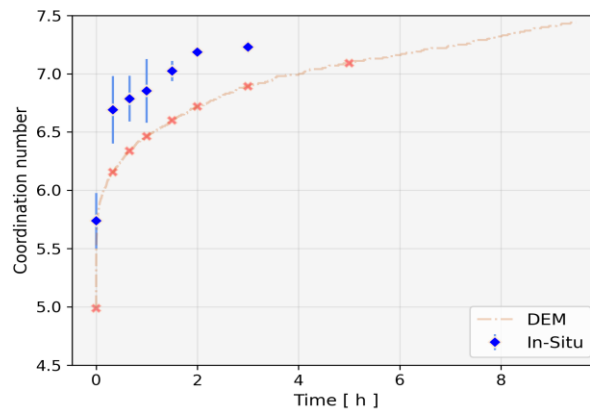


Figure 82. Comparison of co-ordination number as a function of dwell time for alumina Al 1.3 μm sintered and observed in-situ, along with the corresponding DEM simulation.

Neck radius

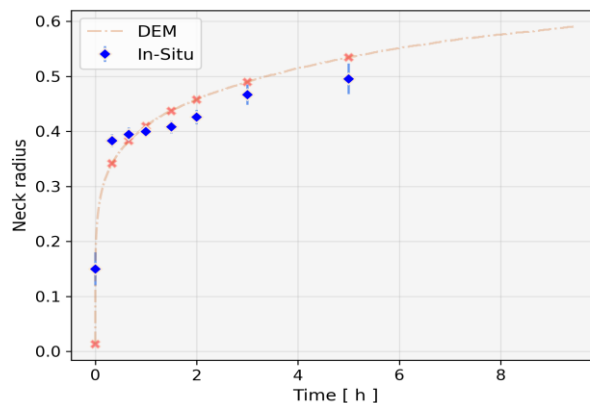


Figure 83. Comparison of neck radius as a function of dwell time for alumina Al 1.3 μm sintered and observed in-situ, along with the corresponding DEM simulation.

The growth of necks between sintering particles was tracked as a function of time, with the methods of calculation as specified. The DEM simulation, with spherical particles, applied the Coble equation for neck size calculations, assuming a *torus* shape for the neck [13] [110]. This is, however, not an accurate representation of the alumina powder at our disposal. The in-situ observation found the actual particles to be not so spherical, and the necks to have varying shapes and sizes, with different contact angles. For the in-situ images, Avizo software package was employed to segment the particles and measure their neck length using a *Feret* concept [79] (ref. **Chapter 4**). It considers the maximum distance between two possible parallel tangents across different orientations of the neck.

The graph of neck radius vs. time (**Figure 83**) showed some discrepancies between the two set of data. At time = 0, the DEM simulation assumes a zero neck size, which is not the case in the experiment as there is already some contact between particles (as seen from in-situ data).

At later times, however, there is a decent match between the two methods, indicating that both capture the general trend of neck growth.

6.3.2 Grain growth - Alumina 0.7 μm

Calibration of DEM model with post-mortem experimental data

For describing the grain growth phenomenon, following the approach proposed by Paredes *et al.* [110], the DEM model included grain growth by surface diffusion and grain boundary migration. This meant the inclusion of calibration of parameters responsible for grain growth as well. Consequently, the parameters obtained after calibration with the post-mortem experimental data were: the pre-factor of grain boundary diffusion of $0.13\text{e-}08 \text{ m}^2/\text{s}$ with an activation energy 475 KJ/mol from the earlier calibration of Alumina 1.3 μm , including the new pre-factors for surface diffusion ($0.09 \text{ m}^2/\text{s}$) and grain boundary migration ($0.01 \text{ m}^3/\text{Ns}^{-1}$), with their activation energies of 313.68 KJ/mol and 443 KJ/mol, respectively, taken from literature [174] [175].

Further, on calibration, alumina of smaller particle size of 0.7 μm was used for grain growth comparison with the DEM simulations. The in-situ observation was done until a density of ~90% was attained and the grain growth phenomenon was evidently more pronounced compared to alumina 1.3 μm (**Chapter 4**).

DEM simulation and comparison with in-situ experimental data

Simulations were performed using the calibrated values for the above mentioned parameters with an alumina powder of $0.7\ \mu\text{m}$ average particle size and an effective standard deviation of 0.13. The initial density was set to 57%, the temperature was fixed at 1500°C and the grain growth trajectory simulation was run until the density reached 90%. To better capture the dynamics of the sintering process, a bigger ROI ($22\ \mu\text{m}$ each side) than the previous case, was opted for, as more number of particles needed to be considered (~ 40000).

A follow-up of the DEM simulation is shown at the corresponding time-steps of the in-situ observations in the **Figure 84**. The set of images of the simulation indicate progressive densification, with a noticeable grain growth towards the end.

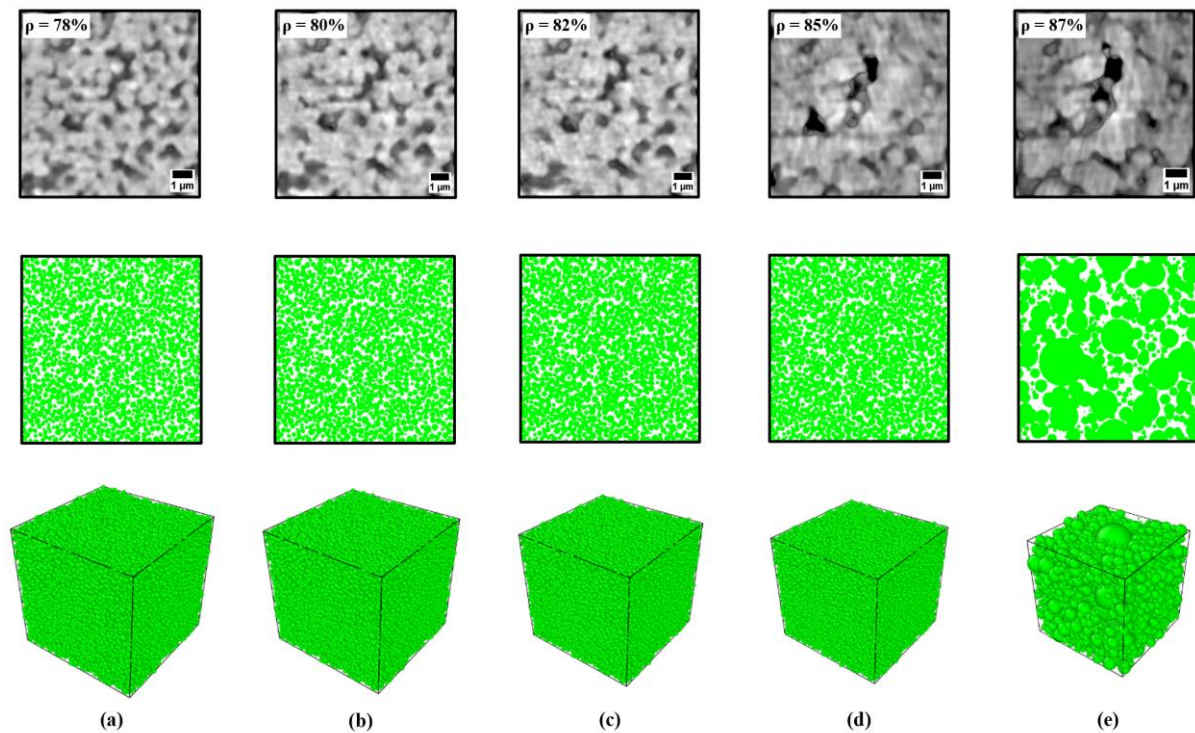


Figure 84. Follow-up of a cropped section of the in-situ observation of the alumina $Al\ 0.7\ \mu\text{m}$ and the corresponding DEM simulation below (in green), after (a) 20 min, (b) 30 min (c) 45 min, (d) 1 hour, and (e) 2 hours of sintering at 1500°C respectively. δ is the *true* relative density (fraction of solid phase).

The results of the simulation are plotted in terms of grain size versus density graph in **Figure 85**. The plot shows a significant discrepancy between the DEM and the experimental curves. The DEM curve exhibited almost no grain growth up until $\sim 85\%$ density and then showed a spike, as reflected in the 3D renderings earlier (**Figure 84**). This suggests that some factors affecting the grain growth process were not adequately captured by the DEM model. The initial

size distribution of the alumina powder being too narrow could be one of the possible reasons for the mismatch. Moreover, assuming spherical particles with uniform contact properties, and neglecting the different local phenomena observed in the in-situ images at the particle level seem to be playing a role on the same.

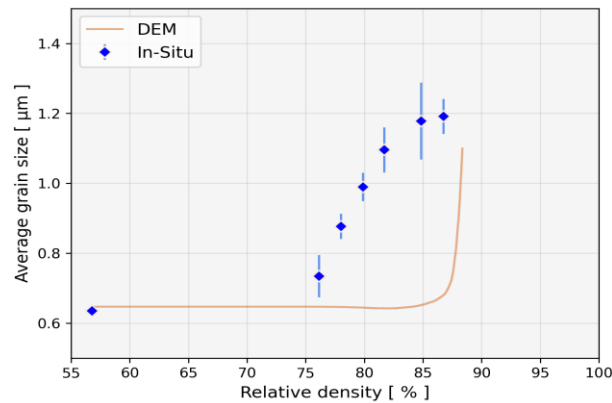


Figure 85. Comparison of grain size evolution as a function of density for alumina Al 0.7µm sintered and observed in-situ, along with the corresponding DEM simulation.

Implementing these changes, especially, using a wider initial size distribution for the alumina powder to account for the natural variability and polydispersity of real powders is in the works.

6.4 Conclusion

An improved DEM model for sintering that incorporates a densification model and a grain growth model was calibrated and validated using experimental data on alumina powders. The calibration method was effective enough to run sintering simulations on the selected powders. The simulation results largely captures the trend observed in the experiments when compared in terms of sintering parameters such as neck growth, coordination number etc. For the grain growth trajectory, however, a substantial inconsistency is observed. We intend to perform new sets of simulations with different assumptions and parameters to explore the possible causes of this discrepancy and to investigate if they can affect the DEM curve and improve the agreement with the experimental outcome.

CHAPTER-7

CONCLUSION AND PERSPECTIVES

This thesis presents a 3D analysis of ceramic powder sintering by synchrotron X-ray nano-tomography - a technique that has enabled us to capture the complex 3D morphology of the particles and pores in the ceramic powder system with an unprecedented voxel size of 25 nm.

The first step in realizing the objectives set was to be able to run the X-ray nano-tomography experiments smoothly and get to the resolution range that can make the individual particles at their length-scale visible, in 3D. Having been successful at that, it was possible to investigate the microstructural evolution of two ceramic powder systems during sintering, at different temperatures and durations. Relevant parameters responsible for sintering such as inter-particle neck growth, pore curvature etc., together with the evolution of accompanying parameters with respect to the grains and the pores, such as grain shapes, grain growth, grain and pore size distribution etc. were quantified, analysed and deliberated.

The X-ray nano-tomography experiments were conducted at the European Synchrotron Radiation Facility (ESRF), in both post-mortem and in-situ modes of operation. Post-mortem, as in, already sintered samples with the facilities in the lab were carried to the synchrotron and fed into a more in-depth observation there. The in-situ route was a step-forward - the samples were directly observed at the synchrotron during the process of sintering.

For the in-situ experiments to materialize, a high temperature, compact furnace was designed and developed. The furnace is apt both in terms of its capabilities to attain the desired temperature as well as its compatibility with the ESRF beamline specifications.

The chosen powder systems varied in their complexity and nature of sintering. To start off, for the first set of experiments, a seemingly simple alumina powder system was used, as it is considered a model material for sintering studies. The chosen alumina, in spite of many of its convenient characteristics, proved to be not so simple when looked at from the prism of X-ray nano-tomography. Local observations, thanks to the high resolution of the experiments, revealed irregularities in the particle shape, size distribution and arrangement, and the ensuing complications during sintering.

The post-mortem 3D images gave a qualitative grasp of the sintering phenomena. Additionally, several quantitative indicators, for instance, with regard to grain size and pore size evolution were put forth. Mathematical equations capturing their trend were proposed. A connectivity index indicator that reflects the changes in pore connectivity and closure by predicting the cut-off density at which the open pores transform into closed ones was recommended as well. Another novel contribution was to identify the pore curvature evolution with the help of 3D images and classifying the stages of sintering on the basis of it.

The in-situ data, on the other hand, provided a local perspective of the sintering process by allowing us to track the same set of particles over time. This permitted, say, the observation of the grain shape changes in terms of their sphericity and roundness, as well as the inter-particle neck growth trajectory. Changes in both grain size and pore size throughout the process were followed-up, and their trajectories were compared with theoretically proposed equations. Plus, local scrutiny revealed the occurrence of particle rearrangement as well as particle coarsening in the early stages of sintering. The pore curvature evolution hypothesis was also confirmed by the in-situ data.

A chapter was also devoted to the comparison of the obtained experimental results with an improved DEM model. The DEM simulations were used to generate initial microstructures and carry out sintering process on the lines of the experiments, to predict and measure important relevant parameters. Numerical predictions were mostly found to be consistent with experimental data, with the exception of grain size evolution, which deserves additional efforts to be accurately described by the model.

The second set of experiments was with a complex blend of ZnO nanopowders and bigger alumina inclusions. The idea behind it was to resemble a real material situation that could be processed by powder metallurgy.

The synchrotron X-ray nano-tomography enabled the visualization of the microstructure of this composite material with a high contrast between the two phases. The study here focused more on the identification and tracking of inhomogeneities as a result of the sintering of this mixture. The 3D images show the constrained effects of the inclusions on the powder system, initiation and continual of the defect morphology, such as cracks and larger pores as the sintering progresses.

For a more systematic list of conclusions, a section has been dedicated at the end of each of the result-focused chapters of 3, 4, 5, and 6.

The perspectives of this work include some limitations and challenges that need to be addressed in future research.

One of them is the difficulty in matching some of the predictions of the sintering model with the experimental results. This requires more accurate modeling of the sintering mechanisms and parameters, taking into account reliable and realistic collection of experimental data.

Another limitation is the temperature range that can be achieved with the current experimental set-up. In this work, the maximum temperature was 1500°C, which is lower than the typical sintering temperature for ceramic materials generally. A higher temperature would let us speed up the sintering process. However, this would also pose challenges for the furnace design and operation, such as the ambient temperature outside the furnace in the hutch, and aspects of thermal stability and radiation shielding.

Moreover, the resolution of the synchrotron X-ray nano-tomography is still insufficient to resolve fine features such as small pores or grain boundaries. As for the constrained sintering study, the resolution of 25 nm is not enough to clearly resolve the individual particles of the ZnO nano-powder. This hinders the possibility of a reliable segmentation of the phases, the prospects of a 3D rendering of the defects and, in turn, an overall quantitative analysis of the sintering parameters. Future work may require improving the resolution or using other complementary techniques to overcome this challenge, enabling a more precise quantification of the microstructure and its evolution during sintering. A higher resolution, by means of an even superior optical arrangement at the nano-imaging beamlines would be very difficult to realize. The final resolution is also closely linked to the size of the focused beam and it would be very challenging to go beyond 50x50 nm. On the other hand, machine learning could play a role - by utilizing deep learning for super-high resolution imaging.

Furthermore, a continuous in-situ observation would be preferable over an interrupted in-situ observation. It would ensure a more seamless flow of visualization, and facilitate comprehension on unresolved matters like particle rearrangement etc.

Finally, a better segmentation approach for image processing would be beneficial for improving the quality and reliability of the quantitative analysis. For instance, as a possible alternative, new tools powered by machine learning that can handle large and complex datasets could be tried out.

In its entirety, this thesis demonstrates the extraordinary potential of synchrotron X-ray nanotomography as a formidable tool for studying ceramic powder sintering, in 3D, with high resolution and precision. Visualization of typical micron-sized ceramic particles at their length-scale is indeed feasible. And, as a matter of fact, a continuous monitoring of ceramic sintering, at this level, at high temperatures, is achievable. Further concerted research in this direction could well contribute to a better understanding and optimization of ceramic processing and sintering, in general.

REFERENCES

- [1] R. K. Bordia, S. J. L. Kang, and E. A. Olevsky, “Current understanding and future research directions at the onset of the next century of sintering science and technology,” *Journal of the American Ceramic Society*, vol. 100, no. 6, pp. 2314–2352, Jun. 2017, doi: 10.1111/jace.14919.
- [2] J. M. Chaix, “Quantitative analysis of microstructure and modeling of sintering,” *Materials Science Forum*, Trans Tech Publications Ltd, 2009, pp. 1–18. doi: 10.4028/www.scientific.net/MSF.624.1.
- [3] E. A. Olevsky, V. Tikare, and T. Garino, “Multi-scale study of sintering: A review,” *Journal of the American Ceramic Society*, Jun. 2006, pp. 1914–1922. doi: 10.1111/j.1551-2916.2006.01054.x.
- [4] D. J. Green, O. Guillon, and J. Rödel, “Constrained sintering: A delicate balance of scales,” *Journal of the European Ceramic Society*, vol. 28, no. 7, pp. 1451–1466, 2008, doi: 10.1016/j.jeurceramsoc.2007.12.012.
- [5] J. Villanova, R. Daudin, P. Lhuissier, D. Jauffres, S. Lou, C. L. Martin, S. Labouré, R. Tucoulou, G. Martínez-Criado, and L. Salvo, “Fast in situ 3D nanoimaging: a new tool for dynamic characterization in materials science,” *Materials Today*, vol. 20, no. 7, pp. 354–359, Sep. 2017, doi: 10.1016/j.mattod.2017.06.001.
- [6] D. Richerson, “The magic of ceramics,” *John Wiley & Sons, Inc.*, Hoboken, New Jersey, 2012.
- [7] W. D. Kingery, H. K. Bowen, and D. R. Uhlmann, “Introduction to ceramics,” Second edition. New York: *John Wiley & Sons*, 1976.
- [8] R. J. Brook, R. W. Cahn, and M. B. Bever, “Concise encyclopedia of advanced ceramic materials,” *Pergamon Press*, 1991.
- [9] M. S. Krishnan, “NPTEL: A programme for free online and open engineering and science education,” *International Workshop on Technology for Education*, 2009, pp. 1–5. doi: 10.1109/T4E.2009.5314112.
- [10] S.-J. L. Kang, “Sintering: densification, grain growth and microstructure,” *Elsevier*, 2005.

- [11] P. Boch and J.-C. Niepce, “Ceramic Materials: Processes, Properties and Applications,” *Hermès Science Publications*, France, 2001.
- [12] M. N. Rahaman, “Ceramic processing and sintering,” *CRC press*, 2003.
- [13] R. L. Coble, “Initial Sintering of Alumina and Hematite,” *Journal of the American Ceramic Society*, vol. 41, no. 2, pp. 55–62, 1958, doi: 10.1111/j.1151-2916.1958.tb13519.x.
- [14] R. L. Coble, “Sintering crystalline solids. I. intermediate and final state diffusion models,” *Journal of Applied Physics*, vol. 32, no. 5, pp. 787–792, 1961, doi: 10.1063/1.1736107.
- [15] J. Frenkel, “Viscous flow of crystalline bodies under the action of surface tension,” *Journal of Physics (USSR)*, 9:385–391, 1945.
- [16] G. C. Kuczynski, “Study of the sintering of glass,” *Journal of Physics*, 20:1160–1163, 1949.
- [17] W. D. Kingery and M. Berg, “Study of the initial stage of sintering solids by viscous flow, evaporation-condensation, and self-diffusion,” *Journal of Applied Physics*, 21:1205–1212, 1955.
- [18] W. S. Coblenz, J. M. Dynys, R. M. Cannon, and R. L. Coble, “Initial stage solid state sintering models. A critical analysis and assessment. Sintering Processes,” *Materials Science Research*, 13, 141-157, 1980.
- [19] D. L. Johnson, “A General Model for the Intermediate Stage of Sintering,” *Journal of the American Ceramic Society*, vol. 53, no. 10, pp. 574–577, 1970, doi: 10.1111/j.1151-2916.1970.tb15969.x.
- [20] W. Beeré, “The intermediate stage of sintering,” *Metal Science*, vol. 10, no. 8, pp. 294–296, Aug. 1976, doi: 10.1179/msc.1976.10.8.294.
- [21] S. C. Coleman and W. B. Beeré, “The sintering of open and closed porosity in UO₂,” *Philosophical Magazine*, vol. 31, no. 6, pp. 1403–1413, Jun. 1975, doi: 10.1080/00318087508228691.
- [22] J. K. Mackenzie and R. Shuttleworth, “A Phenomenological Theory of Sintering,” *Proceedings of the Physical Society, Section B*, vol. 62, no. 12, pp. 833–852, Dec. 1949, doi: 10.1088/0370-1301/62/12/310.

- [23] P. Bross and H. Exner, “Computer simulation of sintering processes,” *Acta Metallurgica*, vol. 27, no. 6, pp. 1013–1020, 1979.
- [24] D. Bouvard and R. M. McMeeking, “Deformation of interparticle necks by diffusion-controlled creep,” *Journal of the American Ceramic Society*, vol. 79, no. 3, pp. 666–672, 1996, doi: 10.1111/j.1151-2916.1996.tb07927.x.
- [25] J. Pan, H. Le, S. Kucherenko, and J. A. Yeomans, “A model for the sintering of spherical particles of different sizes by solid state diffusion,” *Acta Materialia*, 46(13), 4671–4690, 1998.
- [26] A. Wonisch, T. Kraft, M. Moseler, and H. Riedel, “Effect of different particle size distributions on solid-state sintering: A microscopic simulation approach,” *Journal of the American Ceramic Society*, Jul. 2009, pp. 1428–1434. doi: 10.1111/j.1551-2916.2009.03012.x.
- [27] A. Wonisch, O. Guillon, T. Kraft, M. Moseler, H. Riedel, and J. Rodel, “Stress-induced anisotropy of sintering alumina: Discrete element modelling and experiments,” *Acta Materialia*, vol. 55, no. 15, pp. 5187–5199, Sep. 2007, doi: 10.1016/j.actamat.2007.05.038.
- [28] B. Henrich, A. Wonisch, T. Kraft, M. Moseler, and H. Riedel, “Simulations of the influence of rearrangement during sintering,” *Acta Materialia*, vol. 55, no. 2, pp. 753–762, Jan. 2007, doi: 10.1016/j.actamat.2006.09.005.
- [29] G. Petzow and H. E. Exner, “Particle Rearrangement in Solid State Sintering,” *International Journal of Materials Research*, vol. 67, no. 9, pp. 611–618, Sep. 1976, doi: 10.1515/ijmr-1976-670906.
- [30] F. Parhami and R. M. McMeeking, “A network model for initial stage sintering,” *Mechanics of Materials*, vol. 27, no. 2, pp. 111–124, Feb. 1998, doi: 10.1016/S0167-6636(97)00034-3.
- [31] C. L. Martin, L. C. R. Schneider, L. Olmos, and D. Bouvard, “Discrete element modeling of metallic powder sintering,” *Scripta Materialia*, vol. 55, no. 5, pp. 425–428, Sep. 2006, doi: 10.1016/j.scriptamat.2006.05.017.
- [32] S. Martin, M. Guessasma, J. L echelle, J. Fortin, K. Saleh, and F. Adenot, “Simulation of sintering using a Non Smooth Discrete Element Method. Application to the study of rearrangement,” *Computational Materials Science*, vol. 84, pp. 31–39, Mar. 2014, doi: 10.1016/j.commatsci.2013.11.050.

- [33] C. L. Martin, Z. Yan, D. Jauffres, D. Bouvard, and R. K. Bordia, “Sintered ceramics with controlled microstructures: numerical investigations with the Discrete Element Method,” *Journal of the Ceramic Society of Japan*, vol. 124, no. 4, pp. 340–345, 2016, doi: 10.2109/jcersj2.15269.
- [34] T. Rasp, T. Kraft, and H. Riedel, “Discrete element study on the influence of initial coordination numbers on sintering behaviour,” *Scripta Materialia*, vol. 69, no. 11–12, pp. 805–808, Dec. 2013, doi: 10.1016/j.scriptamat.2013.09.003.
- [35] O. Lame, D. Bellet, M. Di Michiel, and D. Bouvard, “Bulk observation of metal powder sintering by X-ray synchrotron microtomography,” *Acta Materialia*, vol. 52, no. 4, pp. 977–984, Feb. 2004, doi: 10.1016/j.actamat.2003.10.032.
- [36] H. E. Exner and T. Kraft, “Review on computer simulations of sintering processes,” *Powder Metallurgy World Congress*, Vol. 2, pp. 278-283, 1998.
- [37] M. Nöthe, M. Schulze, R. Grupp, B. Kieback, and A. Haibel, “Investigation of Sintering of Spherical Copper Powder by Micro Focus Computed Tomography (μ CT) and Synchrotron Tomography,” *Materials Science Forum*, vol. 539–543, pp. 2657–2662, Mar. 2007, doi: 10.4028/www.scientific.net/msf.539-543.2657.
- [38] A. Vagnon, J.P. Rivière, J.M. Missiaen, D. Bellet, M. Di Michiel, C. Josserond, and D. Bouvard, “3D statistical analysis of a copper powder sintering observed in situ by synchrotron microtomography,” *Acta Materialia*, vol. 56, no. 5, pp. 1084–1093, Mar. 2008, doi: 10.1016/j.actamat.2007.11.008.
- [39] L. Olmos, C. L. Martin, D. Bouvard, D. Bellet, and M. Di Michiel, “Investigation of the sintering of heterogeneous powder systems by synchrotron microtomography and discrete element simulation,” *Journal of the American Ceramic Society*, Jul. 2009, pp. 1492–1499. doi: 10.1111/j.1551-2916.2009.03037.x.
- [40] R. Grupp, M. Nöthe, B. Kieback, and J. Banhart, “Cooperative material transport during the early stage of sintering,” *Nature Communications*, vol. 2, no. 1, p. 298, May 2011, doi: 10.1038/ncomms1300.
- [41] B. Kieback, M. Nöthe, J. Banhart, and R. Grupp, “Investigation of sintering processes by tomography,” *Materials Science Forum*, Trans Tech Publications Ltd, 2010, pp. 2511–2516. doi: 10.4028/www.scientific.net/MSF.638-642.2511.

- [42] D. H. Phillips and J. J. Lannutti, “Measuring physical density with X-ray computed tomography,” *NDT&E International*, vol. 30, no. 6, pp. 339–350, Dec. 1997, doi: 10.1016/S0963-8695(97)00020-0.
- [43] T. A. Deis and J. J. Lannutti, “X-ray Computed Tomography for Evaluation of Density Gradient Formation during the Compaction of Spray-Dried Granules,” *Journal of the American Ceramic Society*, vol. 81, no. 5, pp. 1237–1247, Jan. 2005, doi: 10.1111/j.1151-2916.1998.tb02474.x.
- [44] P. Lu, J. J. Lannutti, P. Klobes, and K. Meyer, “X-ray Computed Tomography and Mercury Porosimetry for Evaluation of Density Evolution and Porosity Distribution,” *Journal of the American Ceramic Society*, vol. 83, no. 3, pp. 518–522, Dec. 2004, doi: 10.1111/j.1151-2916.2000.tb01227.x.
- [45] D. Bernard, D. Gendron, J. M. Heintz, S. Bordère, and J. Etourneau, “First direct 3D visualisation of microstructural evolutions during sintering through X-ray computed microtomography,” *Acta Materialia*, vol. 53, no. 1, pp. 121–128, Jan. 2005, doi: 10.1016/j.actamat.2004.09.027.
- [46] Y. Niu, F. Xu, X. Hu, J. Zhao, H. Miao, X. Wu, Z. Zhang “In situ investigation of the silicon carbide particles sintering,” *Journal of Nanomaterials*, vol. 2011, 2011, doi: 10.1155/2011/728617.
- [47] F. Xu, X. F. Hu, Y. Niu, J. H. Zhao, and Q. X. Yuan, “In situ observation of grain evolution in ceramic sintering by SR-CT technique,” *Transactions of Nonferrous Metals Society of China*, vol. 19, Dec. 2009, doi: 10.1016/S1003-6326(10)60132-X.
- [48] F. Wakai, G. Okuma, and N. Nishiyama, “Sintering mechanics of ceramics: a short review,” *Materials Today: Proceedings*, vol. 16, pp. 4-13, 2019.
- [49] Z. Yan, C. L. Martin, D. Bouvard, D. Jauffrès, P. Lhuissier, L. Salvo, L. Olmos, J. Villanova and O. Guillon, “Coupling in-situ X-ray micro- and nano-tomography and discrete element method for investigating high temperature sintering of metal and ceramic powders,” *EPJ Web of Conferences*, 2017, doi: 10.1051/epjconf/201714013006.
- [50] G. Okuma, D. Kadowaki, T. Hondo, S. Tanaka, and F. Wakai, “Interface topology for distinguishing stages of sintering,” *Scientific Reports*, vol. 7, no. 1, p. 11106, Sep. 2017, doi: 10.1038/s41598-017-11667-2.

- [51] G. Okuma, N. Saito, K. Mizuno, Y. Iwazaki, R. Inoue, H. Kishi, A. Takeuchi, M. Uesugi, K. Uesugi, and F. Wakai, “Microstructural evolution of electrodes in sintering of multi-layer ceramic capacitors (MLCC) observed by synchrotron X-ray nano-CT,” *Acta Materialia*, vol. 206, Mar. 2021, doi: 10.1016/j.actamat.2020.116605.
- [52] G. Okuma, T. Osada, H. Minagawa, Y. Arai, R. Inoue, H. Kakisawa, K. Shimoda, A. Takeuchi, M. Uesugi, S. Tanaka, and F. Wakai, “Heterogeneities and defects in powder compacts and sintered alumina bodies visualized by using the synchrotron X-ray CT,” *Journal of the European Ceramic Society*, vol. 43, no. 2, pp. 486–492, Feb. 2023, doi: 10.1016/j.jeurceramsoc.2022.10.020.
- [53] Z. Yan, C. L. Martin, O. Guillon, and D. Bouvard, “Effect of size and homogeneity of rigid inclusions on the sintering of composites,” *Scripta Materialia*, vol. 69, no. 4, pp. 327–330, Aug. 2013, doi: 10.1016/j.scriptamat.2013.05.013.
- [54] G. Martinez-Criado, J. Villanova, R. Tucoulou, D. Salomon, J. P. Suuronen, S. Labouré, C. Guilloud, V. Valls, R. Barrett, E. Gagliardini, and Y. Dabin, “ID16B: A hard X-ray nanoprobe beamline at the ESRF for nano-analysis,” *Journal of Synchrotron Radiation*, 2016, vol. 23, pp. 344–352. doi: 10.1107/S1600577515019839.
- [55] M. Arsenko, F. Hannard, L. Ding, L. Zhao, E. Maire, J. Villanova, H. Idrissi, and A. Simar, “A new healing strategy for metals: Programmed damage and repair,” *Acta Materialia*, vol. 238, Oct. 2022, doi: 10.1016/j.actamat.2022.118241.
- [56] J. Gheysen, D. Tingaud, J. Villanova, A. Hocini, and A. Simar, “Exceptional fatigue life and ductility of new liquid healing hot isostatic pressing especially tailored for additive manufactured aluminum alloys,” *Scripta Materialia*, vol. 233, Aug. 2023, doi: 10.1016/j.scriptamat.2023.115512.
- [57] R. Kumar, J. Villanova, P. Lhuissier, and L. Salvo, “In situ nanotomography study of creep cavities in Al-3.6-Cu alloy,” *Acta Materialia*, vol. 166, pp. 18–27, Mar. 2019, doi: 10.1016/j.actamat.2018.12.020.
- [58] R. Kumar, P. Lhuissier, J. Villanova, L. Salvo, and J. J. Blandin, “Elementary growth mechanisms of creep cavities in AZ31 alloy revealed by in situ X-ray nano-tomography,” *Acta Materialia*, vol. 228, Apr. 2022, doi: 10.1016/j.actamat.2022.117760.

- [59] V. Vanpeene, J. Villanova, A. King, B. Lestriez, E. Maire, and L. Roué, “Dynamics of the Morphological Degradation of Si-Based Anodes for Li-Ion Batteries Characterized by In Situ Synchrotron X-Ray Tomography,” *Advanced Energy Materials*, vol. 9, no. 18, May 2019, doi: 10.1002/aenm.201803947.
- [60] S. D. Auweter, J. Herzen, M. Willner, S. Grandl, K. Scherer, F. Bamberg, M. F. Reiser, F. Pfeiffer, and K. Hellerhoff, “X-ray phase-contrast imaging of the breast - Advances towards clinical implementation,” *British Journal of Radiology*, vol. 87, no. 1034, Feb 2014. doi: 10.1259/bjr.20130606.
- [61] Y. Cheng, H. Suhonen, L. Helfen, J. Li, F. Xu, M. Grunze, P. A. Levkin, and Tilo Baumbach, “Direct three-dimensional imaging of polymer-water interfaces by nanoscale hard X-ray phase tomography,” *Soft Matter*, vol. 10, no. 17, pp. 2982–2990, May 2014, doi: 10.1039/c3sm52604f.
- [62] B. Yu, L. Weber, A. Pacureanu, M. Langer, C. Olivier, P. Cloetens, and F. Peyrin, “Evaluation of phase retrieval approaches in magnified X-ray phase nano computerized tomography applied to bone tissue,” *Optics Express*, vol. 26, no. 9, p. 11110, Apr. 2018, doi: 10.1364/oe.26.011110.
- [63] P. Cloetens, W. Ludwig, J. Baruchel, D. V. Dyck, J. V. Landuyt, J. P. Guigay, and M. Schlenker, “Holotomography: Quantitative phase tomography with micrometer resolution using hard synchrotron radiation x rays,” *Applied Physics Letters*, vol. 75, no. 19, pp. 2912–2914, Nov. 1999, doi: 10.1063/1.125225.
- [64] D. Paganin, S. C. Mayo, T. E. Gureyev, P. R. Miller, and S. W. Wilkins, “Simultaneous phase and amplitude extraction from a single defocused image of a homogeneous object,” *Journal of Microscopy*, vol. 206, no. 1, pp. 33–40, 2002, doi: 10.1046/j.1365-2818.2002.01010.x.
- [65] D. Paganin, “Coherent X-Ray Optics,” *Oxford University Press*, 2006.
- [66] R. Kumar, “In situ nanotomography investigation of cavity nucleation and growth in light alloys during high temperature deformation,” 2019. [Online]. Available: <https://theses.hal.science/tel-02528824>.

- [67] A. Kostenko, K. Joost Batenburg, H. Suhonen, S. E. Offerman, and L. J. Van Vliet, "Phase retrieval in in-line x-ray phase contrast imaging based on total variation minimization," *Optics Express*, vol. 21, no. 1, pp. 710-723, 2013.
- [68] M. Langer, P. Cloetens, J. P. Guigay, and F. Peyrin, "Quantitative comparison of direct phase retrieval algorithms in in-line phase tomography," *Medical Physics*, vol. 35, no. 10, pp. 4556–4566, 2008, doi: 10.1118/1.2975224.
- [69] A. C. Kak and M. Slaney, "Principles of computerized tomographic imaging," *IEEE Press*, The Institute of Electrical and Electronics Engineers, Inc., New York, 1999.
- [70] G. Michael, "X-ray computed tomography," *Special feature: Medical Physics*, 2001, [Online]. Available: www.iop.org/Journals/PhysEd.
- [71] F. P. Vidal, J. M. Létang, G. Peix, and P. Cloetens, "Investigation of artefact sources in synchrotron microtomography via virtual X-ray imaging," *Nuclear Instruments and Methods in Physics Research Section B: Beam Interactions with Materials and Atoms*, vol. 234, no. 3, pp. 333–348, Jun. 2005, doi: 10.1016/j.nimb.2005.02.003.
- [72] A. Lyckegaard, G. Johnson, and P. Tafforeau, "Correction of ring artifacts in X-ray tomographic images," *International Journal of Tomography and Statistics*, 18, pp.1-9, 2011.
- [73] B. Münch, P. Trtik, F. Marone, and M. Stampanoni, "Stripe and ring artifact removal with combined wavelet - Fourier filtering," *Optical Society of America*, vol. 17, no. 10, 2009, doi: 10.1364/oe.17.008567.
- [74] S. Schlüter, A. Sheppard, K. Brown, and D. Wildenschild, "Image processing of multiphase images obtained via X-ray microtomography: A review," *Water Resources Research*, vol. 50, no. 4, pp. 3615–3639, 2014, doi: 10.1002/2014WR015256.
- [75] R. Guinebretière, S. Arnaud, N. Blanc, N. Boudet, E. Thune, D. Babonneau, and O. Castelnau, "Full reciprocal-space mapping up to 2000 K under controlled atmosphere: the multipurpose QMAX furnace," *Journal of Applied Crystallography*, vol. 53, no. 3, p. pp.650-661, 2020, doi: 10.1107/S160057672000432X.
- [76] J. Schindelin, I. Arganda-Carreras, E. Frise, V. Kaynig, M. Longair, T. Pietzsch, S. Preibisch, C. Rueden, S. Saalfeld, B. Schmid, and J. Y Tinevez, "Fiji: An open-source platform for biological-image analysis," *Nature Methods*, vol. 9, no. 7, pp. 676–682, Jul. 2012. doi: 10.1038/nmeth.2019.

- [77] S. van der Walt, J. L. Schönberger, J. Nunez-Iglesias, F. Boulogne, J. D. Warner, N. Yager, E. Gouillart, and T. Yu, “scikit-image: image processing in Python,” *PeerJ*, vol. 2, p. e453, Jun. 2014, doi: 10.7717/peerj.453.
- [78] J. Becker, F. Biebl, E. Glatt, L. Cheng, A. Grießer, M. Groß, S. Linden, D. Mosbach, C. Wagner, A. Weber, and R. Westerteiger, “GeoDict (Release 2022) [Simulation software],” Math2Market GmbH, 2021, doi.org/10.30423/release.geodict2022.
- [79] “Avizo 2021.1, <https://www.fei.com/software/avizo-formaterials-science>,” 2021.
- [80] P. Babin, G. Della Valle, H. Chiron, P. Cloetens, J. Hoszowska, P. Pernot, A. L. Reguerre, L. Salvo, and R. Dendievel, “Fast X-ray tomography analysis of bubble growth and foam setting during breadmaking,” *Journal of Cereal Science*, vol. 43, no. 3, pp. 393–397, May 2006, doi: 10.1016/j.jcs.2005.12.002.
- [81] D. Sundararajan, “Digital Image Processing: A signal processing and algorithmic approach,” *Springer*, 2017.
- [82] J. Ohser and F. Mücklich, “Statistical Analysis of Microstructures in Materials Science”, *Wiley and sons* , 2000.
- [83] B. Otsuki, M. Takemoto, S. Fujibayashi, M. Neo, T. Kokubo, and T. Nakamura, “Pore throat size and connectivity determine bone and tissue ingrowth into porous implants: Three-dimensional micro-CT based structural analyses of porous bioactive titanium implants,” *Biomaterials*, vol. 27, no. 35, pp. 5892–5900, Dec. 2006, doi: 10.1016/j.biomaterials.2006.08.013.
- [84] W. Zhang, K. E. Thompson, A. H. Reed, and L. Beenken, “Relationship between packing structure and porosity in fixed beds of equilateral cylindrical particles,” *Chemical Engineering Science*, 2006, doi: 10.1016/j.
- [85] W. Pabst, E. Gregorová, I. Sedlářová, and M. Černý, “Preparation and characterization of porous alumina-zirconia composite ceramics,” *Journal of the European Ceramic Society*, vol. 31, no. 14, pp. 2721–2731, Nov. 2011, doi: 10.1016/j.jeurceramsoc.2011.01.011.
- [86] L. Olmos, T. Takahashi, D. Bouvard, C. L. Martin, L. Salvo, D. Bellet, and M. Di Michiel, “Analysing the sintering of heterogeneous powder structures by in situ microtomography,” *Philosophical Magazine*, vol. 89, no. 32, pp. 2949–2965, Nov. 2009, doi: 10.1080/14786430903150225.

- [87] F. Delannay and J. M. Missiaen, “Experimental validation of a new model for the initial stage of sintering of single phase systems,” *Acta Materialia*, vol. 57, no. 2, pp. 420–431, 2009, doi: 10.1016/j.actamat.2008.09.019.
- [88] P. Lu, J. J. Lannutti, P. Klobes, and K. Meyer, “X-ray computed tomography and mercury porosimetry for evaluation of density evolution and porosity distribution,” *Journal of the American Ceramic Society*, vol. 83, no. 3, pp. 518–522, 2000, doi: 10.1111/j.1151-2916.2000.tb01227.x.
- [89] F. Xu, X. F. Hu, H. Miao, and J. H. Zhao, “In situ investigation of ceramic sintering by synchrotron radiation X-ray computed tomography,” *Optics and Lasers in Engineering*, vol. 48, no. 11, pp. 1082–1088, Nov. 2010, doi: 10.1016/j.optlaseng.2009.12.012.
- [90] L. Salvo, M. Suéry, A. Marmottant, N. Limodin, and D. Bernard, “3D imaging in material science: Application of X-ray tomography,” *Comptes Rendus Physique*, vol. 11, no. 9–10. Elsevier Masson SAS, pp. 641–649, 2010. doi: 10.1016/j.crhy.2010.12.003.
- [91] S. Fujiwara, Y. Tamura, H. Maki, N. Azuma, and Y. Takeuchi, “Development of New High-Purity Alumina,” *Sumitomo Kagaku*, vol. 2007-I, 2007.
- [92] S. Sakamoto, T. Kajino, T. Nasu, S. Sakaki, and Y. Sakatani, “New Technology and Application - Development of High Purity Alumina,” *Sumitomo Kagaku*, vol. 2020, 2020.
- [93] B. Yu, L. weber, A. Pacureanu, M. Langer, C. Olivier, P. Cloetens, and F. Peyrin, “Phase retrieval in 3D X-ray magnified phase nano CT: Imaging bone tissue at the nanoscale,” *Proceedings - International Symposium on Biomedical Imaging*, IEEE Computer Society, Jun. 2017, pp. 56–59. doi: 10.1109/ISBI.2017.7950467.
- [94] A. Mirone, E. Brun, E. Guillard, P. Tafforeau, and J. Kieffer, “The PyHST2 hybrid distributed code for high speed tomographic reconstruction with iterative reconstruction and a priori knowledge capabilities,” *Nuclear Instruments and Methods in Physics Research Section B: Beam Interactions with Materials and Atoms*, vol. 324, pp. 41–48, Apr. 2014, doi: 10.1016/j.nimb.2013.09.030.
- [95] “GrainFind handbook, in GeoDict 2022 User Guide from Math2Market GmbH, Germany,” doi: doi.org/10.30423/userguide.geodict2022, available at <https://www.geodict.com/userguide/geodict2022.html>

- [96] “Porodict handbook, in GeoDict 2022 User Guide from Math2Market GmbH, Germany,” doi: doi.org/10.30423/userguide.geodict2022, available at <https://www.geodict.com/userguide/geodict2022.html>
- [97] V. Boulos, V. Fristot, D. Houzet, L. Salvo, and P. Lhuissier, “Investigating performance variations of an optimized GPU-ported granulometry algorithm,” *Proceedings of the 2012 Conference on Design and Architectures for Signal and Image Processing*, IEEE, 2012.
- [98] J. J. Koenderink and A. J. van Doorn, “Surface shape and curvature scales,” *Image and vision computing*, 10(8), pp.557-564, 1992.
- [99] A. Burr, P. Lhuissier, C. L. Martin, and A. Philip, “In situ X-ray tomography densification of firn: The role of mechanics and diffusion processes,” *Acta Materialia*, vol. 167, pp. 210–220, Apr. 2019, doi: 10.1016/j.actamat.2019.01.053.
- [100] A. J. Shahani, E. B. Gulsoy, V. J. Rousochatzakis, J. W. Gibbs, J. L. Fife, and P. W. Voorhees, “The dynamics of coarsening in highly anisotropic systems: Si particles in Al-Si liquids,” *Acta Materialia*, vol. 97, pp. 325–337, Jul. 2015, doi: 10.1016/j.actamat.2015.06.064.
- [101] N. P. Bansal and A. R. Boccaccini, “Ceramics and composites processing methods,” *John Wiley & Sons*, 2012.
- [102] T. -S. Yeh and M. D. Sacks, “Effect of Particle Size Distribution on the Sintering of Alumina,” *Journal of the American Ceramic Society*, vol. 71, no. 12, p. C-484-C-487, 1988, doi: 10.1111/j.1151-2916.1988.tb05812.x.
- [103] I. Borgh, P. Hedström, T. Persson, S. Norgren, A. Borgenstam, J. Ågren, and J. Odqvist, “Microstructure, grain size distribution and grain shape in WC-Co alloys sintered at different carbon activities,” *International Journal of Refractory Metals and Hard Materials*, vol. 43, pp. 205–211, 2014, doi: 10.1016/j.ijrmhm.2013.12.007.
- [104] U. Chowdhry and R. M. Cannon, “Microstructural evolution during the processing of sodium β -alumina,” *Processing of Crystalline Ceramics*, pp. 443-455), Springer, Boston, MA., 1978.
- [105] M. F. Yan, R. M. Cannon, H. K. Bowen, and U. Chowdhry, “Effect of Grain Size Distribution on Sintered Density,” *Materials science and engineering*, 60(3), 1983 pp.275-281.
- [106] C. Herring, “Effect of change of scale on sintering phenomena,” *Journal of Applied Physics*, vol. 21, no. 4, pp. 301–303, 1950, doi: 10.1063/1.1699658.

- [107] R. M. German, "Coarsening in sintering: Grain shape distribution, grain size distribution, and grain growth kinetics in solid-pore systems," *Critical Reviews in Solid State and Materials Sciences*, vol. 35, no. 4, pp. 263–305, Oct. 2010, doi: 10.1080/10408436.2010.525197.
- [108] I. Nettleship, R. J. McAfee, and W. S. Slaughter, "Evolution of the grain size distribution during the sintering of alumina at 1350°C," *Journal of the American Ceramic Society*, vol. 85, no. 8, pp. 1954–1960, 2002, doi: 10.1111/j.1151-2916.2002.tb00387.x.
- [109] R. German, "Sintering: from empirical observations to scientific principles," *Butterworth-Heinemann*, 2014.
- [110] B. Paredes-Goyes, D. Jauffres, J. M. Missiaen, and C. L. Martin, "Grain growth in sintering: A discrete element model on large packings," *Acta Materialia*, vol. 218, Oct. 2021, doi: 10.1016/j.actamat.2021.117182.
- [111] J. A. Varela, O. J. Whittemore, and E. Longo, "Pore Size Evolution during Sintering of Ceramic Oxides," *Ceramics International*, vol. 16, no. 3, pp. 177-189, 1990.
- [112] O. J. Whittemore Jr and J. J. Sipe, "Pore Growth during the Initial Stages of Sintering Ceramics," *Powder Technology*, vol. 9, no. 4, pp. 159-164, 1974.
- [113] R. L. Coble and W. D. Kingery, "Effect of Porosity on Physical Properties of Sintered Alumina," *Journal of the American Ceramic Society*, vol. 39, no. 11, pp. 377–385, 1956, doi: 10.1111/j.1151-2916.1956.tb15608.x.
- [114] R. L. Coble and T. K. Gupta, "Sintering and Related Phenomena," *Gordon and Breach*, vol. 6, pp. 423-41, 1967.
- [115] W. Beere, "The second stage sintering kinetics of powder compacts," *Acta Metallurgica*, vol. 23, no. 1, pp. 139–145, 1975, doi: 10.1016/0001-6160(75)90079-6.
- [116] M. Eudier, "Sintering and Related Phenomena," *Gordon and Breach*, vol. 6, pp. 442, 1967.
- [117] J. Svoboda, H. Riedel, and H. Zipse, "Equilibrium pore surfaces, sintering stresses and constitutive equations for the intermediate and late stages of sintering - I. computation of equilibrium surfaces," *Acta metallurgica et materialia*, vol. 42, no. 2, pp. 435-443, 1994.

- [118] J. R. Nimmo, “Porosity and Pore Size Distribution,” *Encyclopedia of Soils in the Environment*, vol. 3, no. 1, pp. 295-303, 2004, doi: 10.1016/b978-0-12-409548-9.05265-9.
- [119] S. C. Coleman and W. B. Beeré, “The sintering of open and closed porosity in UO₂,” *Philosophical Magazine*, vol. 31, no. 6, pp. 1403–1413, 1975, doi: 10.1080/00318087508228691.
- [120] A. Burr, C. Ballot, P. Lhuissier, P. Martinerie, C. L. Martin, and A. Philip, “Pore morphology of polar firn around closure revealed by X-ray tomography,” *The Cryosphere*, vol. 12, no. 7, pp. 2481–2500, Jul. 2018, doi: 10.5194/tc-12-2481-2018.
- [121] A. M. Venkatesh, D. Bouvard, P. Lhuissier, and J. Villanova, “Analysis of Pore Evolution During Ceramic Powder Sintering by Synchrotron X-ray Nano-Tomography,” *Proceedings of the 2022 International Conference on Powder Metallurgy & Particulate Materials*, Metal Powder Industries Federation, 2022.
- [122] H. H. Hu, H. Y. Chen, C. I. Hung, W. Y. Guo, and Y. T. Wu, “Shape and curvedness analysis of brain morphology using human fetal magnetic resonance images in utero,” *Brain Structure and Function*, vol. 218, no. 6, pp. 1451–1462, Nov. 2013, doi: 10.1007/s00429-012-0469-3.
- [123] J. W. Gibbs, K. A. Mohan, E. B. Gulsoy, A. J. Shahani, X. Xiao, C. A. Bouman, M. De Graef, and P. W. Voorhees, “The Three-Dimensional Morphology of Growing Dendrites,” *Scientific reports*, vol. 5, Jul. 2015, doi: 10.1038/srep11824.
- [124] S. Somiya and Y. Moriyoshi, “Sintering Key Papers,” *Springer Science & Business Media*, 2012.
- [125] R. M. German, “Sintering Theory and Practice,” *John Wiley & Sons, Inc.* 1996.
- [126] R. K. Bordia and E. A. Olevsky, “Advances in Sintering Science and Technology: Ceramic Transactions,” *John Wiley & Sons, Inc.*, 2009.
- [127] J. Baruchel, J.-Y. Buffière, E. Maire, P. Merle, and G. Peix, “X-Ray tomography in material science,” *Hermès Science Publications*, 2000.
- [128] G. S. Upadhyaya, “Sintering Fundamentals,” *Material Science Forum*, 2009, pp. 1-152.

- [129] H. E. Exner, “Stereology and 3D microscopy: useful alternatives or competitors in the quantitative analysis of microstructures?,” *Image Analysis & Stereology*, vol. 23, pp. 73–82, 2004, doi: 0.5566/ias.v23.p73-82.
- [130] F. Xu, X. Hu, B. Lu, J. Zhao, X. Wu, and Q. Yuan, “Microstructures-evolution observation of boron carbide ceramic during sintering process by synchrotron radiation X-ray computed tomography,” *Journal of Inorganic Materials*, vol. 24, pp. 175–181, 2009.
- [131] F. Xu, X. F. Hu, H. Miao, and J. H. Zhao, “In situ investigation of ceramic sintering by synchrotron radiation X-ray computed tomography,” *Optics and lasers in engineering*, vol. 48, no. 11, pp. 1082–1088, Nov. 2010, doi: 10.1016/j.optlaseng.2009.12.012.
- [132] J. Lesseur, “Imagerie 3D des matériaux et modélisations numériques : application aux multi-matériaux ferroélectriques,” 2016. [Online]. Available: <https://theses.hal.science/tel-01281311>
- [133] G. Okuma, S. Watanabe, K. Shinobe, N. Nishiyama, A. Takeuchi, K. Uesugi, S. Tanaka, and F. Wakai, “3D multiscale-imaging of processing-induced defects formed during sintering of hierarchical powder packings,” *Scientific reports*, vol. 9, no. 1, Dec. 2019, doi: 10.1038/s41598-019-48127-y.
- [134] A. M. Venkatesh, D. Bouvard, P. Lhuissier, and J. Villanova, “3D analysis of ceramic powder sintering by synchrotron X-ray nano-tomography,” *Journal of the European Ceramic Society*, vol. 43, no. 6, pp. 2553–2563, Jun. 2023, doi: 10.1016/j.jeurceramsoc.2022.12.065.
- [135] S. C. Mayo, A. W. Stevenson, and S. W. Wilkins, “In-Line Phase-Contrast X-ray Imaging and Tomography for Materials Science,” *Materials*, vol. 5, no. 12, pp. 937–965, May 2012, doi: 10.3390/ma5050937.
- [136] O. Stamati, E. Andò, E. Roubin, R Cailletaud, M. Wiebicke, G. Pinzon , C. Couture, R. C. Hurley, R. Caulk, D. Caillerie, T. Matsushima, P. Besuelle, F. Bertoni, T. Arnaud, A. O. Laborin, R. Rorato, Y. Sun, A. Tengattini, O. Okubadejo, J-B. Colliat, M. Saadatfar, F. E Garcia, C. Papazoglou, I. Vego, S. Brisard, J. Dijkstra, G. Birmpilis, “spam: Software for Practical Analysis of Materials,” *Journal of Open Source Software*, no. 51, p. 2286, 2020, doi: 10.21105/joss.02286i.
- [137] “spam: Software for Practical Analysis of Materials, <https://ttk.gricad-pages.univ-grenoble-alpes.fr/spam/index.html>,” 2020.

- [138] A. Kornilov, I. Safonov, and I. Yakimchuk, “A Review of Watershed Implementations for Segmentation of Volumetric Images,” *Journal of Imaging*, vol. 8, no. 5. MDPI, May 01, 2022. doi: 10.3390/jimaging8050127.
- [139] H. E. Exner and C. Müller, “Particle rearrangement and pore space coarsening during solid-state sintering,” *Journal of the American Ceramic Society*, Jul. 2009, pp. 1384–1390. doi: 10.1111/j.1551-2916.2009.02978.x.
- [140] L. Wang, V. Pouchly, K. Maca, Z. Shen, and Y. Xiong, “Intensive particle rearrangement in the early stage of spark plasma sintering process,” *Journal of Asian Ceramic Societies*, vol. 3, no. 2, pp. 183–187, Jun. 2015, doi: 10.1016/j.jascer.2015.02.004.
- [141] S. A. McDonald, C. Holzner, E. M. Lauridsen, P. Reischig, A. P. Merkle, and P. J. Withers, “Microstructural evolution during sintering of copper particles studied by laboratory diffraction contrast tomography (LabDCT),” *Scientific Reports*, vol. 7, no. 1, Dec. 2017, doi: 10.1038/s41598-017-04742-1.
- [142] W. C. Krumbein, “Measurement and geological significance of shape and roundness of sedimentary particles,” *Journal of Sedimentary Research*, vol. 11, no. 2, 1941, pp. 64-72.
- [143] D. L. Johnson and I. B. Cutler, “Diffusion Sintering: I, Initial Stage Sintering Models and Their Application to Shrinkage of Powder Compacts,” *Journal of the American Ceramic Society*, vol. 46, no. 11, pp. 541–545, 1963, doi: 10.1111/j.1151-2916.1963.tb14606.x.
- [144] H. E. Exner, “Principles of single-phase sintering,” *Reviews on powder metallurgy and physical ceramics*,(1/4), pp. 1-251, 1979.
- [145] F. W. Dynys and J. W. Halloran, “Influence of Aggregates on Sintering,” *Journal of the American Ceramic Society*, vol. 67, no. 9, pp. 596–601, 1984, doi: 10.1111/j.1151-2916.1984.tb19601.x.
- [146] F. F. Lange, “Sinterability of Agglomerated Powders,” *Journal of the American Ceramic Society*, vol. 67, no. 2, pp. 83–89, 1984, doi: 10.1111/j.1151-2916.1984.tb09620.x.
- [147] W. H. Rhodes, “Agglomerate and Particle Size Effects on Sintering Yttria-Stabilized Zirconia,” *Journal of the American Ceramic Society*, vol. 64, no. 1, pp. 19–22, 1981, doi: 10.1111/j.1151-2916.1981.tb09552.x.

- [148] F. F. Lange, "Powder Processing Science and Technology for Increased Reliability," *Journal of the American Ceramic Society*, vol. 72, no. 1, pp. 3–15, 1989, doi: 10.1111/j.1151-2916.1989.tb05945.x.
- [149] A. G. Evans, "Considerations of Inhomogeneity Effects in Sintering," *Journal of the American Ceramic Society*, vol. 65, no. 10, pp. 497–501, 1982, doi: 10.1111/j.1151-2916.1982.tb10340.x.
- [150] C.-H. Hsueh, "Sintering behaviour of powder compacts with multi heterogeneities," *Journal of materials science*, vol. 21, pp. 2067-2072, 1986.
- [151] M. W. Weiser and L. C. De Jonghe, "Inclusion Size and Sintering of Composite Powders," *Journal of the American Ceramic Society*, vol. 71, no. 3, p. C-125-C-127, 1988, doi: 10.1111/j.1151-2916.1988.tb05030.x.
- [152] L. C. De Jonghe, M. N. Rahaman, and C. H. Hsueh, "Transient stresses in bimodal compacts during sintering," *Acta Metallurgica*, vol. 34, no. 7, pp. 1467-1471, 1986.
- [153] D. J. Green, O. Guillon, and J. Rödel, "Constrained sintering: A delicate balance of scales," *Journal of the European Ceramic Society*, vol. 28, no. 7, pp. 1451–1466, 2008, doi: 10.1016/j.jeurceramsoc.2007.12.012.
- [154] A. M. Venkatesh, C. Rajon, D. Bouvard, P. Lhuissier, and J. Villanova, "In-situ 3D X-ray investigation of ceramic powder sintering at the particle length-scale [Manuscript submitted for publication]," *Ceramics International*, 2023.
- [155] T. -S Yeh and M. D. Sacks, "Effect of Particle Size Distribution on the Sintering of Alumina," *Journal of the American Ceramic Society*, vol. 71, no. 12, p. C-484-C-487, 1988, doi: 10.1111/j.1151-2916.1988.tb05812.x.
- [156] A. Salehi, G. Pircheraghi, and R. Foudazi, "Pore structure evolution during sintering of HDPE particles," *Polymer*, vol. 183, Nov. 2019, doi: 10.1016/j.polymer.2019.121865.
- [157] L. C. De Jonghe, M.-Y. Chu, and M. K. F. Lin, "Pore size distribution, grain growth, and the sintering stress." *Journal of Materials Science*, vol. 24, pp. 4403-4408, 1989.
- [158] A. G. Evans and C. H. Hsueh, "Behavior of Large Pores During Sintering and Hot Isostatic Pressing," *Journal of the American Ceramic Society*, vol. 69, no. 6, pp. 444–448, 1986, doi: 10.1111/j.1151-2916.1986.tb07442.x.

- [159] F. Lorenzano-Porras, D. H. Reeder, M. J. Annen, P. W. Carr, and A. V McCormick, "Unusual Sintering Behavior of Porous Chromatographic Zirconia Produced by Polymerization-Induced Colloid Aggregation," *Industrial & engineering chemistry research*, vol. 34, no. 8, pp. 2719–2727, 1995.
- [160] T. Kimura, H. Kajiyama, R. Yazaki, and T. Yamaguchi, "Effects of nondensifying inclusions on the densification and microstructure of zinc oxide matrix composites," *Journal of Materials Science*, vol. 31, pp. 4149-4157, 1996.
- [161] W. H. Tuan, E. Gilbert, and R. J. Brook, "Sintering of heterogeneous ceramic compacts Part 1 Al₂O₃-Al₂O₃," *Journal of Materials Science*, vol. 24, pp. 1062-1068, 1989.
- [162] S. M. Salamone, "Densification of and constitutive laws for ceramic matrix composites and multilayered systems - PhD Thesis," University of Washington, Seattle, 2003.
- [163] F. F. Lange, "Processing-Related Fracture Origins: I, Observations in Sintered and Isostatically Hot-Pressed Al₂O₃/ZrO₂ Composites," *Journal of the American Ceramic Society*, vol. 66, no. 6, pp. 396–398, 1983, doi: 10.1111/j.1151-2916.1983.tb10068.x.
- [164] F. F. Lange, B. I. Davis, and I. A. Aksay, "Processing-Related Fracture Origins: III, Differential Sintering of ZrO₂ Agglomerates in Al₂O₃/ZrO₂ Composite," *Journal of the American Ceramic Society*, vol. 66, no. 6, pp. 407–408, 1983, doi: 10.1111/j.1151-2916.1983.tb10070.x.
- [165] R. Raj and R. K. Bordia, "Sintering behavior of bi-modal powder compacts," *Acta Metallurgica*, vol. 32, pp. 1003-1019, 1984.
- [166] G. W. Scherera, "Sintering with Rigid Inclusions," *Journal of the American Ceramic Society*, vol. 70, no. 10, pp. 719–725, 1987, doi: 10.1111/j.1151-2916.1987.tb04870.x.
- [167] C. -L. Fan and M. N. Rahaman, "Factors Controlling the Sintering of Ceramic Particulate Composites: I, Conventional Processing," *Journal of the American Ceramic Society*, vol. 75, no. 8, pp. 2056–2065, 1992, doi: 10.1111/j.1151-2916.1992.tb04465.x.
- [168] C. L. Martin, L. C. R. Schneider, L. Olmos, and D. Bouvard, "Discrete element modeling of metallic powder sintering," *Scripta Materialia*, vol. 55, no. 5, pp. 425–428, Sep. 2006, doi: 10.1016/j.scriptamat.2006.05.017.

- [169] B. Henrich, A. Wonisch, T. Kraft, M. Moseler, and H. Riedel, “Simulations of the influence of rearrangement during sintering,” *Acta Materialia*, vol. 55, no. 2, pp. 753–762, Jan. 2007, doi: 10.1016/j.actamat.2006.09.005.
- [170] S. Martin, S. Navarro, H. Palancher, A. Bonnin, J. L  chelle, M. Guessasma, J. Fortin, and K. Saleh, “Validation of DEM modeling of sintering using an in situ X-ray microtomography analysis of the sintering of NaCl powder,” *Computational Particle Mechanics*, vol. 3, no. 4, pp. 525–532, Nov. 2016, doi: 10.1007/s40571-015-0062-7.
- [171] A. Lichtner, D. Roussel, D. R  hrens, D. Jauffres, J. Villanova, C. L. Martin, and R. K. Bordia, “Anisotropic sintering behavior of freeze-cast ceramics by optical dilatometry and discrete-element simulations,” *Acta Materialia*, 2018, doi: 10.1016/j.actamat.2018.06.001i.
- [172] D. Roussel, A. Lichtner, D. Jauffr  s, J. Villanova, R. K. Bordia, and C. L. Martin, “Strength of hierarchically porous ceramics: Discrete simulations on X-ray nanotomography images,” *Scripta Materialia*, vol. 113, pp. 250–253, 2016, doi: 10.1016/j.scriptamat.2015.11.015.
- [173] B. Paredes-Goyes, A. M. Venkatesh, D. Jauffres, and C. L. Martin, “Two-step sintering of alumina nano-powders: A discrete element study,” *Journal of the European Ceramic Society*, vol. 43, no. 2, pp. 501–509, Feb. 2023, doi: 10.1016/j.jeurceramsoc.2022.10.001.
- [174] W. M. Robertson and R. Chang, “The Kinetics of Grain-Boundary Groove Growth on Alumina Surfaces,” *The Role of Grain Boundaries and Surfaces in Ceramics: Proceedings of the Conference*, pp. 49-60, Springer US, doi: 10.1007/978-1-4899-6311-6.
- [175] S. J. Dillon and M. P. Harmer, “Intrinsic grain boundary mobility in alumina,” *Journal of the American Ceramic Society*, vol. 89, no. 12, pp. 3885–3887, Dec. 2006, doi: 10.1111/j.1551-2916.2006.01331.x.